POSSIBLE QUINTESSENCE-LIKE PSEUDOSCALAR DARK ENERGY EFFECTS ON ^{56}FE NUCLEAR TRANSITION ENERGIES OBSERVED IN SUPERNOVA 1991T

by

Robert D. Orlando

A Dissertation

Submitted to the Faculty of Purdue University

In Partial Fulfillment of the Requirements for the degree of

Doctor of Philosophy

Department of Physics and Astronomy

West Lafayette, Indiana

May 2025

THE PURDUE UNIVERSITY GRADUATE SCHOOL
STATEMENT OF COMMITTEE APPROVAL

Dr. David Koltick, Chair

Department of Physics and Astronomy

Dr. Dimitrios Giannios

Department of Physics and Astronomy

Dr. Dennis Krause

Department of Physics and Astronomy

Dr. L. Martin Kruczenski

Department of Physics and Astronomy

Approved by:

Dr. Gabor A. Csathy

To GG, Nana, and Aunt Denise for all of their love and support

ACKNOWLEDGMENTS

I am extremely grateful to Prof. Ephraim Fischbach for his mentorship and invigorating enthusiasm towards science. This work would not have been possible without him agreeing to be my first serious advisor. Our conversations and interactions were the first that started me on the path of becoming a practitioner of physical research.

Prof. Dennis Krause has persisted in helping me develop this project from the day that I was introduced to him by Prof. Fischbach. I would always walk away from our conversations motivated and refreshed. It was reassuring to talk physics with someone who shared the same values and ideals in the way that they conducted their work. By meeting Prof. Krause, I not only worked with a colleague, but I met a kindred spirit and made a friend.

I will always be very grateful to Prof. David Koltick for taking me on as his Ph.D. student, even agreeing to continue working with me into his retirement. Prof. Koltick always showed much care and enthusiasm for the project and spent much time discussing it with me, which led to a large increase in the quality of the research. His advice will be something I carry with me throughout my career.

I am thankful to the committee members Prof. Dimitrios Giannios and Prof. Martin Kruczenski for being a part of this project. Prof. Giannios and Prof. Kruczenski were always very welcoming whenever I had questions that aligned with their expertise. Both professors always took the time to answers my questions thoroughly and were always patient with me until I reached an understanding. The larger astrophysics group with the department have also been very helpful and patient. I am grateful for the willingness and patience of Prof. Paul Duffel, Prof. Abigail Polin, and Prof. Danny Milisavljevic for their time in addressing my seemingly endless list of questions.

This thesis would not have been possible without all of the love and support of the people closest to me. My great-grandmother GG, my grandmother Nana, my great Aunt Denise, my sister Seffrah and my partner Kike have always had the utmost faith in my ability to complete this dissertation, even when I did not. Their unconditional love, patience, and encouragement have always carried me through worst of times and truly created the best of times.

TABLE OF CONTENTS

LIST OF TABLES

LIST OF FIGURES

LIST OF SYMBOLS

A	nuclear mass number
$a(t)$	scale factor at time t
$\alpha_{\lambda\mu}(t)$	deformation parameter for liquid drop model
α	decay constant coefficient
α, β	liquid scintillator resolution parameters
B_0	ratio of meson masses
B_Λ	nuclear inertia of liquid drop model
C_Λ	restoring force of liquid drop model
c	speed of light in vacuum
$\delta E/E$	energy deviation from expected, redshifted value
ε	nuclear surface energy of liquid drop model
e	fundamental unit charge
E_{phon}	energy of level within a nucleus modeled as a liquid drop
E_{rig}	energy of level within a nucleus modeled as a rigid rotor
f_π	decay constant of pion
f_Q	decay constant of quintessence-like field
$F_{\mu\nu}$, $F^{\mu\nu}$	electromagnetic field tensor
$\tilde{F}_{\mu\nu}$, $\tilde{F}^{\mu\nu}$	dual to the electromagnetic field tensor
g	determinant of metric tensor
$g_{\mu\nu}$, $g^{\mu\nu}$	metric tensor
g_{CB}	coupling constant for cosmic birefringence
g_S	coupling of strong force
G	Newton's constant
$G_{a\mu\nu}$, $G_a^{\mu\nu}$	gluon field strength tensor of color a
H	Hubble rate
H_0	Hubble rate today
h	hadron species
$\hbar$	reduced Planck's constant

$\mathcal{I}$	nuclear moment of inertia
J	angular momentum quantum number
κ	constant equivalent to $\sqrt{8\pi G}$
K_h	sensitivity coefficient of hadron species h
$K_{h,q}$	sensitivity coefficient between hadron species h and quark species q
$\mathcal{L}$	Lagrangian density (referred to as Lagrangian)
Λ	cosmological constant
λ	index denoting vibrational modes of liquid drop model
M	parameter for quintessence tracking potential
m	nucleon mass
m_d	mass of down quark
m_h	mass of hadron species h
m_π	mass of the pion
M_{pl}	unreduced Planck mass
m_q	mass of quark species q
m_u	mass of up quark
N	neutron number
Ω_{KE}	dimensionless kinetic energy density of quintessence-like field
Ω_Λ	dimensionless energy density of dark energy
Ω_V	dimensionless energy density of quintessence potential
ω	vibrational frequency of surface of nuclear liquid drop
ω_2	frequency of phonon associated with quadrupole vibrations of nuclear surface
P	pressure
p	tracking potential power
ϕ	phantom dark energy field
Q	quintessence field
Q_Λ	constant term of quintessence field that corresponds to the cosmological constant
R_0	spherical nuclear radius
r_0	parameter for determining nuclear charge radius

R	Ricci scalar
ρ	mass density of nucleus
ρ_{crit}	critical energy density of the universe
ρ_Λ	energy density of dark energy
S	action
σ_i	resolution of gamma ray line i
t	cosmic time
$T_{\mu\nu}$, $T^{\mu\nu}$	stress-energy tensor
θ	QCD vacuum angle
V	potential
w_Λ	dark energy equation of state parameter
ξ	parameter for determining gamma ray energy deviation for the liquid drop model
Y	Yukawa matrices
z	redshift
Z	proton number
ζ	coefficient of liquid drop phonon frequency

ABSTRACT

Fitting the background-subtracted spectral data of SN 1991T indicates that the gamma rays emitted by the ^{56}Fe nuclei are shifted to lower energies at the 3.2σ statistical level. The average energy shift of both the first and second excited states is found to be $\delta E/E = 0.023 \pm 0.007$ where the uncertainty is given at one standard deviation. Assuming this energy shift is constant as the universe evolves over time implies that $\delta \dot{E}/E = (5.2 \pm 1.7) \times 10^{-10}$ yr^{-1}. It is assumed that this energy shift is caused by a dynamical pseudoscalar field Q that acts as dark energy with a coupling to the nucleons of atoms. This interaction would cause an apparent variation in the mass of the pion, thereby shifting the gamma ray energies. To relate the energy deviation to the pion mass and Q, the excited ^{56}Fe nucleus is modeled as a deformed rigid rotor and vibrating liquid drop. The implied pion mass variation, indicated by the observed energy deviations, is found to be $\delta \dot{m}_\pi/m_\pi = -(2.2 \pm 0.7) \times 10^{-10}$ yr^{-1}, modeling the nucleus as a deformed rigid rotor, and $\delta \dot{m}_\pi/m_\pi = -(2.5 \pm 0.8) \times 10^{-10}$ yr^{-1}, modeling the nucleus as a vibrating liquid drop. It can also be used to determine the value of $\dot{Q}$, which corresponds to the term of the dark energy field that changes as the universe evolves. This quantity will depend on the free parameters α and p, which are the decay constant coefficient of the field and the power of the quintessence tracking potential, respectively. The maximum value of $\dot{Q}$ will result for $\alpha = 0.1$ and $p = 1$. These values are $\dot{Q} = (1.07 \pm 0.35) \times 10^8$ GeV/yr for the nucleus as a rigid rotor and $\dot{Q} = (1.22 \pm 0.39) \times 10^8$ GeV/yr for the nucleus as a vibrating liquid drop. The measured values of the dark energy equation of state parameter determined by DESI observations of the BAO and complemented by Planck observations of the CMB and SNe indicate that there exists an allowed α–p parameter space. This implies that the fractional kinetic energy densities determined by $\dot{Q}$ are consistent with cosmological observations under the assumptions that are used throughout this work. Here upper limits are also presented to take into account the possibility that the observed energy deviations are caused by an unknown systematic error.

1. OVERVIEW

A novel framework is developed to relate the energy deviations of astrophysical gamma rays produced in nuclear processes to a quintessence-like field Q through its contribution to the pion mass. The gamma rays used for this purpose are those emitted by SN 1991T [1], a peculiar Type Ia supernova that contains iron-56 (^{56}Fe) in an excited state that is produced by the decay of cobalt-56 (^{56}Co), which is long lived (77-days) relative to its parent nucleus nickel-56 (^{56}Ni, 6 days) [2]. ^{56}Fe produced in this way is always produced in an excited state [3]. This nucleus will emit gamma rays to deexcite to its ground state and produce a spectrum that is dominated by gamma rays with energies 847 keV and 1238 keV [4]. Figure 1.1 shows the best fit of the background-subtracted gamma ray data taken by COMPTEL [5].

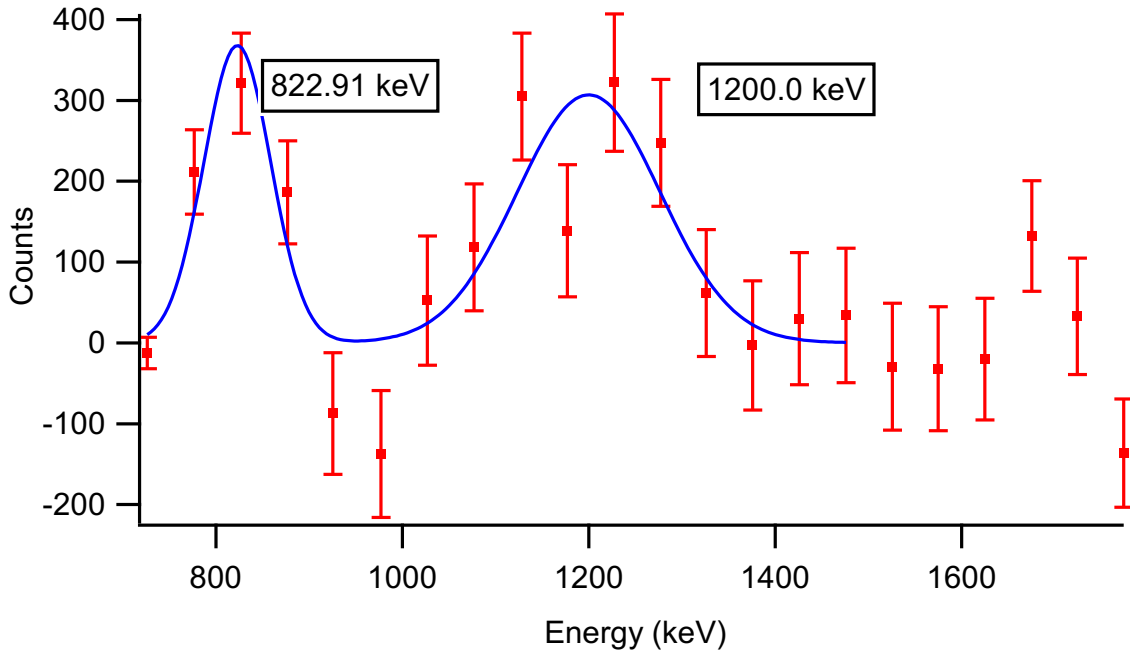

Figure 1.1. Best fit ($\chi^2/DoF \approx 1.42$) of SN1991T gamma ray data. The first peak corresponds to the transition of ^{56}Fe from the first excited 2+ state to the 0+ ground state. The second peak corresponds to the transition from the second excited 4+ state to the first excited 2+ state.

This fit, which was produced using `Igor Pro 9` [6], indicates the average energy shift of the detected gamma rays from the first and second excited states of ^{56}Fe in SN 1991T is

$$\frac{\delta E}{E} = 0.023 \pm 0.007, \tag{1.1}$$

when compared with gamma rays produced by the same process in terrestrial experiments. The plus-minus value is the uncertainty at one standard deviation. The above value takes into account the redshift of the host galaxy NGC4527 caused by its velocity relative to the Milky Way ($z = 0.005791$) [7]. It is assumed that the rate of change of the energy is constant over time, and since SN 1991T is 13.5 megaparsecs away (44.0 million lightyears), this implies

$$\frac{\delta \dot{E}}{E} = (5.2 \pm 1.7) \times 10^{-10}\ \text{yr}^{-1}. \tag{1.2}$$

While this energy discrepancy may be caused by other physics processes, in this thesis it is assumed that it results from the coupling of a new light pseudoscalar degree of freedom (Q) to the hadronic sector [8]. The existence of cosmological pseudoscalar fields is suggested by the anomalous measurement of cosmic birefringence [9]. In principle, any pseudoscalar degree of freedom will contribute to the QCD vacuum angle θ [10]. This, in turn, will introduce a contribution of Q to the pion mass through [11]

$$m_\pi^2 = \frac{2B_0}{f_\pi^2}[m_u^2 + m_d^2 + 2m_u m_d \cos\theta]^{1/2}, \tag{1.3}$$

where B_0 is a constant determined by the ratio of meson masses and has value 7.6×10^6 MeV^3, m_u and m_d are the masses of the up and down quarks taken to be 4 MeV and 7 MeV, respectively, and f_π is the pion decay constant, which has value 92.4 MeV. If this axion-like particle (ALP) field changes as the universe evolves, so then too will the mass of the pion as [12]

$$\frac{\delta \dot{m}_\pi}{m_\pi} \approx -0.05 \frac{d\theta^2}{dt}. \tag{1.4}$$

Because the exchange of pion(s) characterizes an important contribution to the interaction of protons and neutrons in the nucleus via the strong force, there will be apparent variations

in the nuclear mass, radius, and magnetic moment as the universe evolves [8]. The variation of the nuclear radius due to the change in the pion and nucleon mass, parameterized by the pion mass variation, is given by [12]

$$\frac{\delta r_0}{r_0} = 1.2\frac{\delta m_\pi}{m_\pi}, \tag{1.5}$$

where r_0 is a constant that is used to determine the nuclear radius through $R_0 = r_0 A^{1/3}$ and has value 1.2 femtometers.

Two models can be used to determine the dependence of the nuclear transition energies of the ^{56}Fe excited states on the nuclear radius. These are the nucleus as a deformed classical rigid rotor and as a charged liquid drop undergoing surface vibrations. It is found that

$$\frac{\delta \dot{E}_{rig}}{E_{rig}} = -2\frac{\delta \dot{r}_0}{r_0}, \tag{1.6}$$

$$\frac{\delta \dot{E}_{phon}}{E_{phon}} = -\frac{(1-3\xi/2)}{(1-\xi)}\frac{\delta \dot{r}_0}{r_0}. \tag{1.7}$$

Both of these equations imply that the resulting pion mass variation is

$$\left(\frac{\delta \dot{m}_\pi}{m_\pi}\right)_{rig} = -(2.2 \pm 0.7) \times 10^{-10}\ \text{yr}^{-1}, \quad \left(\frac{\delta \dot{m}_\pi}{m_\pi}\right)_{phon} = -(2.5 \pm 0.8) \times 10^{-10}\ \text{yr}^{-1}, \tag{1.8}$$

where the uncertainty is given at one standard deviation. This limit is eight orders of magnitude larger than the best limit produced by studies of the Oklo natural nuclear reactor [13]. However, there exist several differences between this work and the analyses of Oklo that make this work complementary to Oklo, rather than superseded by it. The studies of Oklo are conducted using single particle models and the observed disappearance of Samarium-149 for the goal of generating a limit on quark mass variations [13]. Separate subsequent analyses use these results to indicate the dark matter energy density (see [12]). This analysis uses astrophysical gamma rays produced by the deexcitation of the ^{56}Fe nucleus and compare them to the gamma rays produced in the same process here on earth. Any observed deviation is quantified using collective nuclear models for the purpose of determining the configuration of a quintessence-like field acting as dark energy, specifically through its kinetic energy density.

The use of an extragalactic gamma ray source (SN 1991T), provides a future opportunity to study differences in the local matter and energy distributions of the Milky Way and NGC 4527 and/or the interactions of the photons as they travel to earth-bound detectors.

If the the decay constant of the ALP field is chosen to be $f_Q = \alpha M_{pl}/\sqrt{8\pi}$ where $\alpha \approx O(0.1)$ and $M_{pl} = \sqrt{\hbar c/G}$ is the unreduced Planck mass and is 1.22×10^{19} GeV, Q can potentially play the part of a dynamical dark energy field with the characteristics required by observation (e.g. slow-roll) [14]–[16]. Assuming that the entire value of the QCD vacuum is determined by Q allows one to write

$$\theta = \frac{Q}{f_Q}, \tag{1.9}$$

and produce upper limits on parameters associated with the field from the aforementioned energy deviations. Further assuming that dark energy is approximately a cosmological constant at the current epoch permits the expansion

$$Q \approx Q_\Lambda + \dot{Q}(t_0)\Delta t, \tag{1.10}$$

where Q_Λ is the constant part of the field that mimics a cosmological constant, $\dot{Q}(t_0)$ is the value of the time-varying part of the field at initial time t_0, and Δt is the interval between the initial time t_0 and the current time t. Finally, values for the upper limits on the time-dependent part of the field $\dot{Q}$ are found using the equations

$$\dot{Q}_{rig} = \frac{(\alpha M_{pl}/\sqrt{8\pi})^2}{0.24 Q_\Lambda \Delta t}\frac{\delta E}{E}, \tag{1.11}$$

$$\dot{Q}_{phon} = \frac{(\alpha M_{pl}/\sqrt{8\pi})^2}{0.12 Q_\Lambda \Delta t}\frac{1-\xi}{1-3\xi/2}\frac{\delta E}{E}, \tag{1.12}$$

where α is the decay constant coefficient and ξ is defined to be

$$\xi \equiv \frac{3}{10}\frac{Z^2 e^2}{\varepsilon A^{1/3}}\frac{1}{r_0}, \tag{1.13}$$

and has value approximately 2.94 for the ^{56}Fe nucleus. In the above equation, Z is the atomic number, e is the fundamental charge, ε is the surface energy of the liquid drop, and A is the atomic mass number [17]. The values of $\dot{Q}$ can be used to find observable quantities such as the fractional kinetic energy density

$$\Omega_{KE} \equiv \frac{1}{2\rho_{crit}}\dot{Q}^2, \tag{1.14}$$

and the dark energy equation of state parameter

$$w_Q \equiv \frac{P_Q}{\rho_Q} = \frac{\Omega_{KE} - \Omega_V}{\Omega_{KE} + \Omega_V}, \tag{1.15}$$

where Ω_V is the fractional energy density of the field's potential. The determination of the above quantity is the subject of intense experimental and theoretical efforts. The allowed parameter spaces for α and p (the power of the quintessence potential) based on measurements of w_Q for both nuclear models are provided in Figures 1.2 and 1.3.

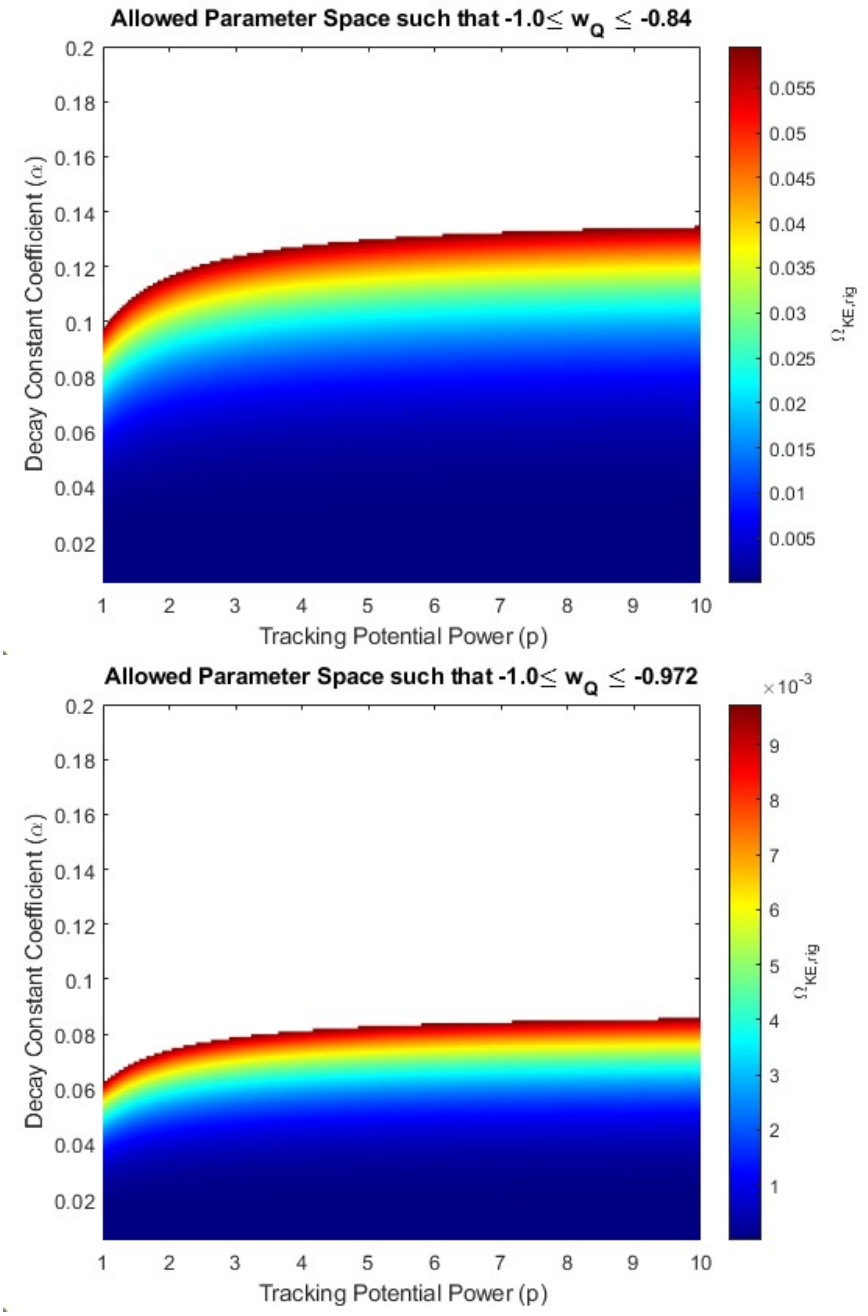

Figure 1.2. Allowed parameter spaces of α and p for the rigid rotor model. The top plot uses the allowed values of dark energy equation of state parameter as indicated by DESI only. The bottom plot uses the allowed values of dark energy equation of state parameter as indicated by DESI measurements of the BAO and Planck measurements of the Cosmic Microwave Background and Supernovae. The color indicates the fractional kinetic energy density given in Equation (1.14) and is only allowed to be as high as approximately 6.8%.

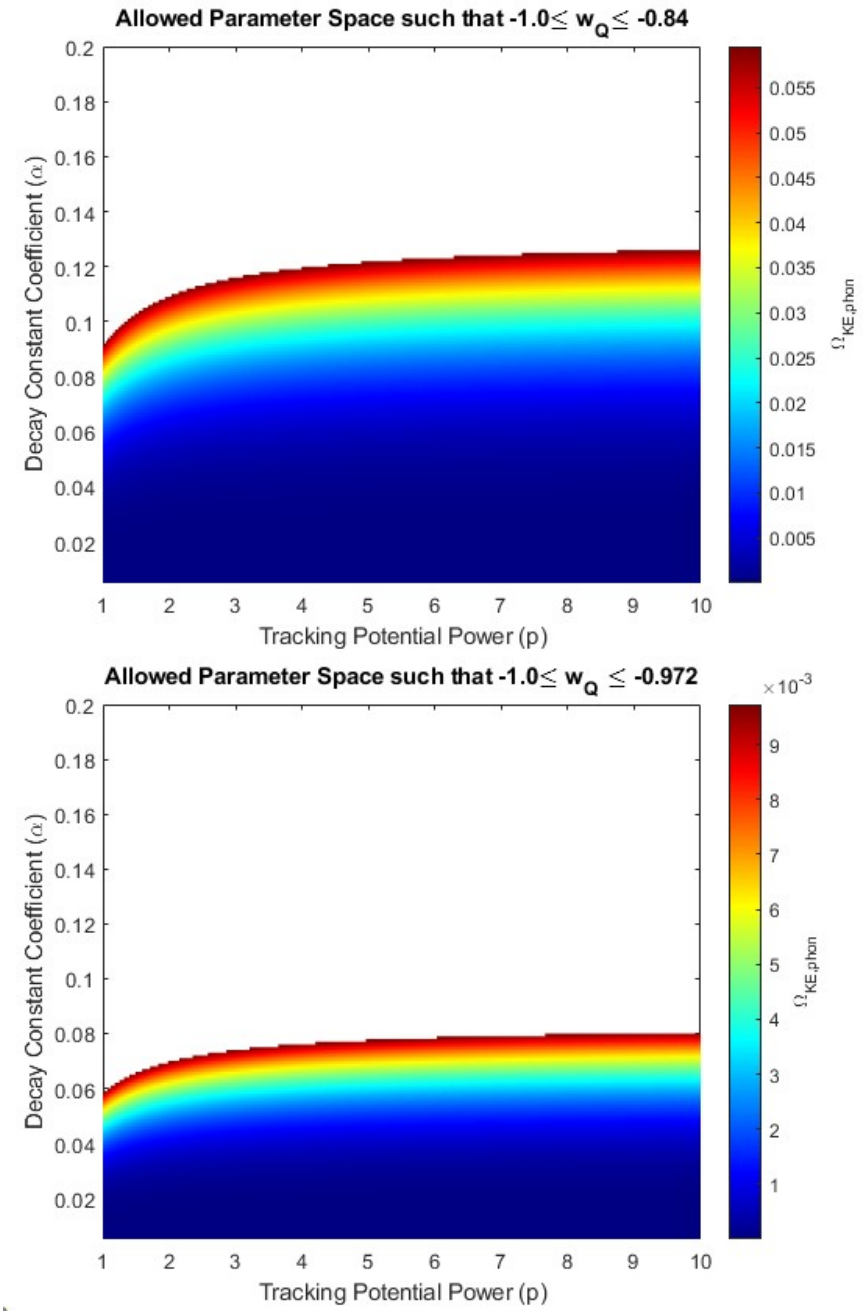

Figure 1.3. Allowed parameter spaces of α and p for the charged liquid drop model. The top plot uses the allowed values of the dark energy equation of state parameter as indicated by DESI only. The bottom plot uses the allowed values of dark energy equation of state parameter as indicated by DESI measurements of the BAO and Planck measurements of the Cosmic Microwave Background and Supernovae. The color indicates the fractional kinetic energy density given in Equation (1.14) and is only allowed to be as high as approximately 6.8%

2. INTRODUCTION

It has been a well established fact since the 1930s that the universe is expanding after Edwin Hubble made the observation that the light reaching us from distant galaxies is red-shifted [18]. A more surprising discovery came in 1998 when observing the redshift of Type Ia supernovae. Not only is the universe expanding, but the rate of this expansion is increasing [19]. Later, this fact would be more firmly established by measurements of the power fluctuations in the cosmic microwave background (CMB) [20], the comparison of the baryon acoustic oscillations (BAO) signal to theoretical predictions [21], and the extent to which light is bent from gravitational lensing [22].

The origin of this acceleration is still a puzzle, but two main paradigms are used to explain this accelerated expansion. The first is that the theory of Einstein, general relativity, breaks down at large scales such as those of the universe. Within this paradigm, physicists desire to find a modified theory of general relativity that correctly includes and explains this long-range behavior of gravity. Some examples of these extensions are $f(\mathrm{R})$ models [23], the modified Newtonian dynamics (MOND) theory [24], and the Dvali-Gabadadze (DGP) model [25]. The second paradigm posits that there is an unaccounted-for energy density, referred to as dark energy, that drives the expansion of the universe [19]. This dark energy is sourced from exotic matter not included in the standard model. The source and nature of dark energy are not known, but cosmological observations require models of dark energy to comprise about 70% of the energy density of the universe in the form of negative pressure (which corresponds to an equation of state parameter $w_\Lambda = -1$) [19].

The first and simplest attempt to characterize dark energy was in the form of vacuum energy and led to the reintroduction of the cosmological constant to Einstein's equations, which was first introduced to allow for a static universe [19], [26], [27]. Lambda-Cold Dark Matter (ΛCDM), sometimes referred to as the standard model of cosmology, is the accepted model of dark energy and dark matter. Within this model, the vacuum exerts a constant negative pressure (Λ) that drives the accelerated expansion of the universe [28] and dark matter is non-relativistic, weakly interacting, pressure-less matter that holds galaxies together [29]. ΛCDM shows excellent agreement with observation and is considered the most

successful cosmological model in physics. However, there are well-documented perplexities and tensions that arise from the model (see [30] for a review). This has prompted the view within the physics community that ΛCDM needs to be extended to address the resulting "curiosities".

Classically, the cosmological constant does not create any theoretical or observational discrepancies; however, when considering quantum vacuum fluctuations, there is a major discrepancy in the expected and measured vacuum energies [26]. Additionally, using the cosmological constant to model dark energy inevitably introduces issues of fine-tuning, coincidence, and naturalness [31], [32]. To be specific, using the cosmological constant to model the accelerated expansion of the universe results in a 120 order of magnitude discrepancy between the theoretical and observed vacuum energies caused by the inclusion of the quantum fluctuations in the vacuum. This striking issue is commonly referred to as the *cosmological constant problem*. There exist means to exactly cancel the additional vacuum contributions to yield the observed energy density, but there is no comprehensive theoretical explanation motivating this process. These cancellations, usually invoking some variation of the anthropic principle [33], introduce fine-tuning concerns to the theoretical treatment of the accelerating expansion of the universe [26], [27]. Furthermore, it is observed that the energy densities of dark energy and matter were comparable to each other in recent cosmic history. The cosmological constant does not offer any theoretical explanation of why this would take place or why these two quantities would be related [34]. This is a major coincidence that can possibly have a deeper physical explanation. As a final point, the theory associated with a cosmological constant contains no explanation as to why it is so small compared to the scales of particle physics [35]. Having no satisfying theoretical explanation of the smallness of the cosmological constant calls into question its naturalness.

Additionally, the use of the cosmological constant does not offer a resolution to the Hubble tension, which refers to the significant 5σ-6σ disagreement that arises when comparing different determinations of the Hubble rate today (H_0) [36]. The first method to determine H_0 is by taking measurements of CMB anisotropies using the *Planck* satellite and predicting its value within the context of the ΛCDM model. These estimates (referred to as early-time estimates), determined by Planck and ACT+WMAP data, consistently yield values of

67.4 ± 0.5 km s^{-1} Mpc^{-1} and 67.6 ± 1.1 km s^{-1} Mpc^{-1}, respectively [36]. The second method to determine H_0 is from local measurements of low-redshift probes such as supernovae [37]. These determinations (referred to as late-time estimates) fall in the range of 70–76 km s^{-1} Mpc^{-1} [36]. This disagreement has not been resolved by increases in the accuracy of cosmological measurements. The differences in these values suggest that the behavior of dark energy is more complex than a constant energy density produced by vacuum, since the latter cannot produce the observed discrepancy [37], [38].

To attempt to resolve the cosmological constant problem, coincidence problem, naturalness problem, and also provide a possibility for relaxing the Hubble tension, dynamical models of dark energy have been introduced. The simplest of these abstractions replaces the cosmological constant by a dynamical scalar field with the stipulation that it behaves similarly to a cosmological constant at the current epoch [39]–[41]. With this model, referred to as quintessence, dark energy is able to change with the evolution of the universe, which introduces a time-dependent equation of state [41]. Furthermore, depending on the form of the potential of this field, tracking behavior can be exhibited by dark energy. Tracking behavior refers to when the energy density of the quintessence field is dependent upon the evolution of radiation and matter energy densities [42]. These tracking potentials allow for a natural resolution to the cosmological constant problem and the coincidence problem without introducing a fine-tuning of initial conditions [42], [43].

Even more mysterious is the microphysical nature of dark energy. Large scale cosmological behaviors do not uniquely determine the nature of dark energy [44]. Rather, hints need to be taken across particle physics and astrophysics, in addition to cosmology, to start with a well-informed guess of what dark energy could be and then test that hypothesis. For example, across the aforementioned fields in physics, there is an indication that dark energy exists as a pseudoscalar field of effective mass $\leq 10^{-33}$ eV [16], [45]–[47]. This mass is characteristic of a dark energy field. A mass greater than this value would comprise a fraction of dark matter, which allows the two fields to be distinguished from each other [47]. This is the specific form of dark energy that is phenomenologically studied in this thesis.

If dark energy were to exist as a dynamical pseudoscalar field, there would be a plethora of implied phenomena based on the couplings that this field is assumed to have [48]. In this

study, it is assumed that the pseudoscalar dark energy field interacts with the nucleons of atoms. One possible consequence of this is the apparent variation of the mass of pions which, in turn, affects nuclear properties such as the nuclear mass, radius, and magnetic moment [8]. If this is the case, the energies produced by nuclear processes will be affected.

Using this collection of considerations from astrophysics, nuclear physics, and particle physics along with experimental methods, the time-varying part of a quintessence-like field ($\dot{Q}$) is quantified here. Therefore, this study produces a framework for determining the nature and behavior of dark energy from its effects on nuclear processes. This framework can be extended to new astrophysical and nuclear systems, so that the fundamental nature and large-scale behavior of dark energy can be further probed. It also allows for the study of other models of dark energy, such as K-essence, phantom dark energy, and quintom dark energy (see [26] and [34] for general reviews) and their effects on the nucleus.

The dissertation is structured in the following way. Chapter 3 will introduce the necessary background information, including a description of cosmic birefringence, which suggests the existence of cosmic pseudoscalar fields, axions, which are a light pseudoscalars that find their origin in quantum chromodynamics (QCD), the formalism and governing equations of quintessence, and Type Ia supernovae, which is the astrophysical system of study chosen for this work. Also included in this chapter is a collection of limits on the quark and pion mass variations and an explanation of what separates this analysis from analyses of the Oklo natural nuclear reactor from which the best limits are derived. Chapter 4 details the theoretical ideas that serve as the basis for this work. The origin of the variation of the fundamental constants as a study, which this work utilizes, is described. This is presented with an emphasis on how the quark masses and pion mass would change when interacting with a light pseudoscalar degree of freedom. Two nuclear models are then described, and their theoretical uncertainties are determined. These models are used to derive the upper limit for $\dot{Q}$ and the values chosen for the free parameters are explained. Chapter 5 details SN 1991T, the supernova from which the gamma ray data was extracted, and COMPTEL, the observing detector. The best fits of the background-subtracted data and a discussion of these best fits are provided. The upper limits computed for $\dot{Q}$ are presented along with allowed parameter spaces as indicated by astrophysical and cosmological observations. Chapter 6

discusses the difficulties encountered in this work along with possible improvements on the analysis and avenues of future inquiry. The main results are summarized in Chapter 7.

For this work, natural units are utilized where $\hbar = c = 1$. The Axion refers to the hypothetical particle that arises from the strong CP problem of QCD. Axion-like particles (ALPs) refer to any light pseudoscalar degree of freedom that will contribute to the QCD vacuum angle. Axions refer both to the Axion and ALPS.

3. PRELIMINARIES

Since the goal of this work is to relate a nuclear energy deviation to a pseudoscalar quintessence field, all of the concepts have to be introduced and given a brief background. The first introduced is the measurement of cosmic birefringence, which suggests the existence of a cosmic pseudoscalar field. Next discussed is a compelling candidate of this pseudoscalar motivated by string theory and particle physics. Canonical quintessence, where the cosmic field is a scalar, is then described with a focus on what this model attempts to achieve, its advantages over dark energy as a cosmological constant, how it generates universal accelerated expansion, and the equations that govern the field's dynamics. Type Ia supernovae will be the system by which a limit is derived for the time-varying component of the quintessence field. What these are and the processes by which they generate gamma ray spectra are discussed.

3.1 Cosmic Birefringence

Measurements of photons from the CMB suggest that the polarizations of these photons are rotated as they propagate. This phenomenon is known as cosmic birefringence [49]. The rotation angle is reported, in one case, to be 0.35 ± 0.14 degrees at one standard deviation producing an unexpected 2.4σ result [9]. The non-rotation of the polarizations is excluded with a 99.2% confidence level. Other measurements indicate a similar rotation angle with a deviation exceeding 3σ in some cases [47]. What is causing the cosmic birefringence of CMB photon's polarizations as they travel to orbiting detectors?

The possibility that the birefringence of CMB photons is caused by conventional standard model physics, such as Thomson scattering, is considered [50]. However, it is believed that cosmic birefringence is much more likely to arise form beyond standard model physics. Some possibilities that are explored in the literature are primordial magnetic fields [51], Lorentz invariance violation [52], non-commutative gauge theories [53], and photon scattering with cosmic neutrinos [54]. However, the most prominent view is that the photons reaching

detectors on or orbiting Earth from the CMB are propagating through a pseudoscalar field with a Chern-Simons coupling of the form [38]

$$\mathcal{L}_{CB} = -\frac{1}{4} g_{CB} Q F_{\mu\nu} \tilde{F}^{\mu\nu}, \tag{3.1}$$

where $F_{\mu\nu}$ is the electromagnetic tensor, $\tilde{F}_{\mu\nu}$ is its dual, g_{CB} is a coupling constant, and Q is the pseudoscalar field. This coupling introduces a difference in the dispersion relation of left- and right-handed photons, making the pseudoscalar field a birefringent medium for photons [45], [55]. A well motivated scenario worth exploring is where the pseudoscalar field that possibly produces cosmic birefringence is the Axion or ALP.

3.2 Axions

The Axion of quantum chromodynamics (QCD) is a hypothetical, light pseudoscalar particle that find its origin in the strong charge-parity (CP) problem of QCD. The strong CP problem can be summarized as the confusing fact that the strong interaction is not observed to violate CP symmetry despite the existence of a CP violating term in the QCD Lagrangian

$$\mathcal{L}_{\theta} = \theta \frac{g_S^2}{32\pi^2} G_a^{\mu\nu} \tilde{G}_{a\mu\nu}, \tag{3.2}$$

where θ is the QCD vacuum angle, g_s is the coupling of the strong force, $G_a^{\mu\nu}$ is the gluon field strength tensor of color a, and $\tilde{G}_{a\mu\nu}$ is its dual. Measurements of the neutron electric dipole moment (EDM) show $\bar{\theta}$, which is related to the QCD vacuum angle (θ) by

$$\overline{\theta} = \theta - \text{Arg det}(Y_u Y_d), \tag{3.3}$$

where Y_u and Y_d are the Yukawa matrices for the up and down quarks, to be less than 10^{-11} [56]. Since there is no physical reason for the unnatural smallness of θ, axions were introduced to make θ a dynamical variable with a preferred value of zero [57], [58].

A common scenario explored in the literature is that the pseudoscalar field of the preceding section is the Axion or an ALP [14], [46], [59], [60]. This is because of the pseudoscalar

nature of the Axion and ALPs , how well motivated their existence is from considerations of QCD [61], [62], and how ubiquitous light pseudoscalar degrees of freedom are in string theories [45]. The small mass that axions can obtain (at and below 10^{-33} GeV) [10], in addition to the axion mass range required for the signal of birefringence (see [55]), suggests that axions can potentially comprise all dark energy and a fraction of dark matter [45], [56], [63], [64]. The case where an axion field is responsible for dark energy in the form of a quintessence field has been studied using string theory and shown to posses a potential varying slowly enough to be consistent with cosmological observations [16].

3.3 Quintessence

The modeling of dark energy as a constant energy density from the vacuum (referred to as the cosmological constant) does not address the coincidence problem or other theoretical questions related to dark energy [33]–[35]. Furthermore, different methods of determining the expansion rate of the universe yield values that disagree (the Hubble Tension [36]) and the observed and theoretical values of the cosmological constant disagree by 120 orders of magnitude (the cosmological constant problem [33]). The simplest theoretical generalization to the cosmological constant to address these shortcomings and tensions are quintessence models. Quintessence is a model where the dynamics of a cosmic scalar field with a minimal coupling to gravity is responsible for the accelerating expansion of our universe [26], [27], [34]. In Quintessence, the total action with non-relativistic matter is

$$S = \int d^4x\sqrt{-g}\left[\frac{1}{2}\frac{M_{pl}^2}{8\pi}R - \frac{1}{2}g^{\mu\nu}\partial_\mu Q\partial_\nu Q - V(Q)\right] + S_m, \tag{3.4}$$

where Q is the quintessence field, $M_{pl} = \sqrt{\hbar c/G}$ is the unreduced Planck mass, g is the determinant of the metric tensor $g_{\mu\nu}$, R is the Ricci scalar, and S_m is the action associated with matter [35], [41].

This action is considered in the standard flat Friedman-Lemaître-Robertson-Walker (FLRW) universe where the line element is $ds^2 = -dt^2 + a^2(t)dx^2$ and $a(t)$ is the scale factor at cosmic

time t. Within this context, varying the action with respect Q yields the equation for the evolution of the quintessence field

$$\ddot{Q} + 3H\dot{Q} + \frac{dV}{dQ} = 0, \tag{3.5}$$

where $H \equiv \dot{a}/a$ [27], [34], [43]. All quantities with a dot are derivatives of that quantity with respect to cosmic time.

By taking the variation of the action with respect to $g_{\mu\nu}$ (ignoring the matter contribution since it does not produce accelerated expansion), the energy-momentum tensor of the quintessence field is derived which is [26], [34], [43]

$$T_{\mu\nu}^{(Q)} = -\frac{2}{\sqrt{-g}}\frac{\delta(\sqrt{-g}\mathcal{L}_Q)}{\delta g^{\mu\nu}} = \partial_\mu Q \partial_\nu Q - g_{\mu\nu}\left[\frac{1}{2}g^{\alpha\beta}\partial_\alpha Q \partial_\beta Q + V(Q)\right]. \tag{3.6}$$

Using the energy-momentum tensor allows one to find the energy density and pressure of the field as well as the equation of state parameter w_Q [34]

$$\rho_Q = -T_0^{0(Q)} = \frac{1}{2}\dot{Q}^2 + V(Q), \tag{3.7}$$

$$P_Q = \frac{1}{3}T_{\mathrm{i}}^{\mathrm{i}(Q)} = \frac{1}{2}\dot{Q}^2 - V(Q), \tag{3.8}$$

$$w_Q \equiv \frac{P_Q}{\rho_Q} = \frac{\dot{Q}^2 - 2V(Q)}{\dot{Q}^2 + 2V(Q)}. \tag{3.9}$$

It can be surmised from the above expression that the value of w_Q that corresponds to the cosmological constant is -1 since $\dot{Q}$ will be zero and only the potentials will remain in the numerator and denominator. Even when studying quintessence models, it is necessary to require that $-1.0 \leq w_Q \leq -0.972$ at the current time in cosmic history due to the amount of observational evidence that suggests this scenario [65]–[69]. This implies that the "kinetic energy" of the quintessence field ($\dot{Q}^2/2$) is much smaller than its potential $V(Q)$. Evaluating the Einstein equation in the flat FLRW background yields the standard Friedman equations of [26]

$$3\frac{M_{pl}^2}{8\pi}H^2 = \rho_Q = \frac{1}{2}\dot{Q}^2 + V(Q), \tag{3.10}$$

$$-2\frac{M_{pl}^2}{8\pi}\dot{H} = \rho_Q + P_Q = \dot{Q}^2. \tag{3.11}$$

Imposing local energy conservation yields a continuity equation within quintessence-type models [26]

$$\partial_\mu \xi_\nu T^{(Q)\mu\nu} = \dot{\rho}_Q + 3H(\rho_Q + P_Q) = 0, \tag{3.12}$$

where ξ_ν is the Killing vector indicating the symmetries of the FLRW spacetime.

The equation governing the accelerating expansion of the universe is obtained by taking linear combinations of the two Friedman equations [26]. The result is

$$-\frac{3M_{pl}^2}{4\pi}\left[\frac{\ddot{a}(t)}{a(t)}\right] = \rho_Q + 3P_Q = 2\left[\dot{Q}^2 - V(Q)\right]. \tag{3.13}$$

The above equations are the general dynamical equations of quintessence. At this point, the common practice is to begin to build a specific quintessence-type model by choosing an explicit form of potential $V(Q)$. The choice of potential should allow for an accelerating universal expansion, the main feature of quintessence, which is achieved by choosing $V(Q)$ to be flat and currently dominating over matter in our universe [40]. In order to serve its purpose, a quintessence model must have a mechanism that adequately motivates its recent dominating contribution to the accelerating expansion (e.g. it must address the coincidence problem of the cosmological constant) as well as an indication of a natural set of initial conditions to prevent fine-tuning of the theory. This is accomplished with tracker quintessence models [70].

The original and simplest tracker potential derived by Ratra and Peebles is an inverse power law that has the general form [71]

$$V(Q) = M^{4+p}Q^{-p}, \tag{3.14}$$

where M is a quantity that is fixed by the observed fractional energy density of dark energy Ω_Λ, which is 0.685 [27], [72]. The main feature of a potential of this form is the quintessence field *tracks* the evolution of the matter and radiation energy densities which, in turn, influences the evolution of the energy density of the quintessence field. In fact, it is found that

the energy density of the quintessence field, with the potential in Equation (3.14) decreases less rapidly than the matter and radiation energy densities of the universe [40]. This leads to a point in cosmic history when the energy density of the quintessence field overtakes the energy density of matter and becomes the main contributor to accelerated universal expansion. Another attractive feature of tracker models is that they are insensitive to initial conditions; a wide range of initial conditions lead to the same cosmic evolution [27], [70].

Quintessence, in this way, is able to relax the cosmological constant problem as well as the issues of fine-tuning, naturalness, and coincidence that come along with it. Also, it should be noted that a quintessence field can act as dark energy, dark matter, or both depending on the effective mass of the field [9], [47], thereby possibly solving the mysteries of dark energy and dark matter simultaneously. The Hubble tension is not sufficiently relaxed in the case of canonical (scalar) quintessence; however, the general idea of quintessence, which is the departure from the scenario of constant dark energy, can still potentially alleviate the Hubble tension [37].

Quintessence does relax the aforementioned issues, but it does not solve them outright. Making the energy density of Q comparable to the matter energy density still requires fine-tuning. Additionally, for the slow evolution of Q, it is required that

$$M^{4+p} \approx (8\pi G)^{-1-p/2} H_0^2, \tag{3.15}$$

which is determined by observation and not based on any theoretical first-principles [27].

Any quintessence field will obey the general Taylor expansion

$$Q(t) = Q_\Lambda + \dot{Q}(t_0)(t - t_0) + ... \tag{3.16}$$

if $\dot{Q}(t_0)$ is approximately constant for a sufficiently small time interval relative to the age of the universe (13.7 billion years). In the above equation, Q_Λ is the lowest order term of the field corresponding to the cosmological constant, $\dot{Q}(t_0)$ is the derivative of the field with respect to cosmic time evaluated at t_0, t is the current time after the big bang, and t_0 is an earlier, recent time (cosmically speaking) after the big bang. Since the cosmological constant

serves as a good approximation of dark energy, $\dot{Q}$ varies slowly in time and can be seen as approximately constant since the ratio of Δt, which is the time it takes light to reach earth from SN 1991T (44.0×10^6 years), to the age of the universe (13.7×10^9 years) behaves like 10^{-3}.

The above expansion can be seen as the astrophysical version of a similar expansion that is more applicable to nuclear and atomic experiments. The lab-based version of the expansion, utilizing the energy-time uncertainty relation, is

$$Q(t) \approx Q_\Lambda + \dot{Q}(t_0)\frac{\hbar}{\Delta E} \approx Q_\Lambda + \frac{\dot{Q}(t_0)}{\Delta \nu}, \tag{3.17}$$

where $\Delta\nu$ is the frequency drift of a nuclear or atomic transition. The atomic transition frequency drift has been determined experimentally for the Ytterbium ion (Yb^+, $Z = 70$) [73], [74] and others (see [75]). These results have been used to place limits on the variation of the quark and hadron masses [13] and used to determine the dark matter energy density [12]. The quark mass variation limits will be presented in a later section so that they may be compared with the limits produced from the astrophysical approach that is developed in this study.

The simple and generic Taylor series expansion given by Equation (3.16) suggests three non-trivial facts: (i) $\dot{Q}$ can be seen as a measure of how much dark energy deviates from a cosmological constant, (ii) the larger the value of $t - t_0$, the better the limits (in terms of their smallness) that are placed on $\dot{Q}$, (iii) any limits placed on $\dot{Q}$ can help discriminate among different quintessence models. In relation to point (ii), it is important to note that the time interval cannot be large ($\Delta t \sim 10^9$ years) to the point that $\dot{Q}$ is no longer constant. Point (iii) arises from the relation between the time derivative of the field and $V(Q)$ using Equation (3.5).

The smallness of $\dot{Q}$ relative to $V(Q)$ implied by the dark energy equation of state being close to -1 simplifies the study of quintessence by allowing the assumption that the value is constant, but also makes any effect associated with $\dot{Q}$ difficult to detect for time scales small relative to the age of the universe. In order to mitigate this consequence, it is beneficial to consider the extreme environments of astrophysical events and cosmological systems. Asso-

ciated with these systems are long distances, large time intervals, and high-energy regimes that cannot be achieved in most experiments here on Earth. One example of these extreme astrophysical events are the deaths of stars, specifically Type Ia supernovae, of which there exist many that are well studied.

3.4 Type Ia Supernovae

A Type Ia supernova is a distinct death process of a star understood through the delayed detonation model [76]. This thermonuclear explosion occurs when a white dwarf, formed when the original star has fused all hydrogen in its core and sheds its outer layer of gas, accretes enough material from a companion star to reach the Chandrasekhar mass (see Figure 3.1) [2]. Type Ia supernovae are distinguished from Type II supernovae by the lack of hydrogen and helium in their spectra and the strong presence of silicon emission lines in the spectra early after the initial explosion [77]. Later, the spectrum is dominated by emission lines of iron elements formed in the ejecta of the explosion (which is of particular interest to this study) [2]. Due to the high luminosity and homogeneity of the light curves compared to the other types of supernovae, Type Ia supernovae are used as standard candles to determine astrophysical distances [78]. The analysis of the redshift of light reaching earth from Type Ia supernovae was the first indicator that the universe is expanding at an increasing rate, which would later be further suggested by additional measurements and analyses [19].

The explosion of the white dwarf, after accreting mass to the point where it exceeds 1.4 solar masses, creates an extremely energetic environment in which iron elements can be formed by nuclear fusion in the exploded white dwarf's ejecta [2], [77]. In this way, a population of nickel can be formed by nuclear fusion in the explosion and would decay into iron via the radioactive process

$$^{56}\text{Ni} \rightarrow ^{56}\text{Co} \rightarrow ^{56}\text{Fe}. \tag{3.18}$$

The population of ^{56}Ni produced in the explosion will decay into ^{56}Co by electron capture, which, in turn, decays into ^{56}Fe, also via electron capture [2]. Early after the explosion, the resulting ejecta is optically thick to the gamma rays produced by these nuclear decays,

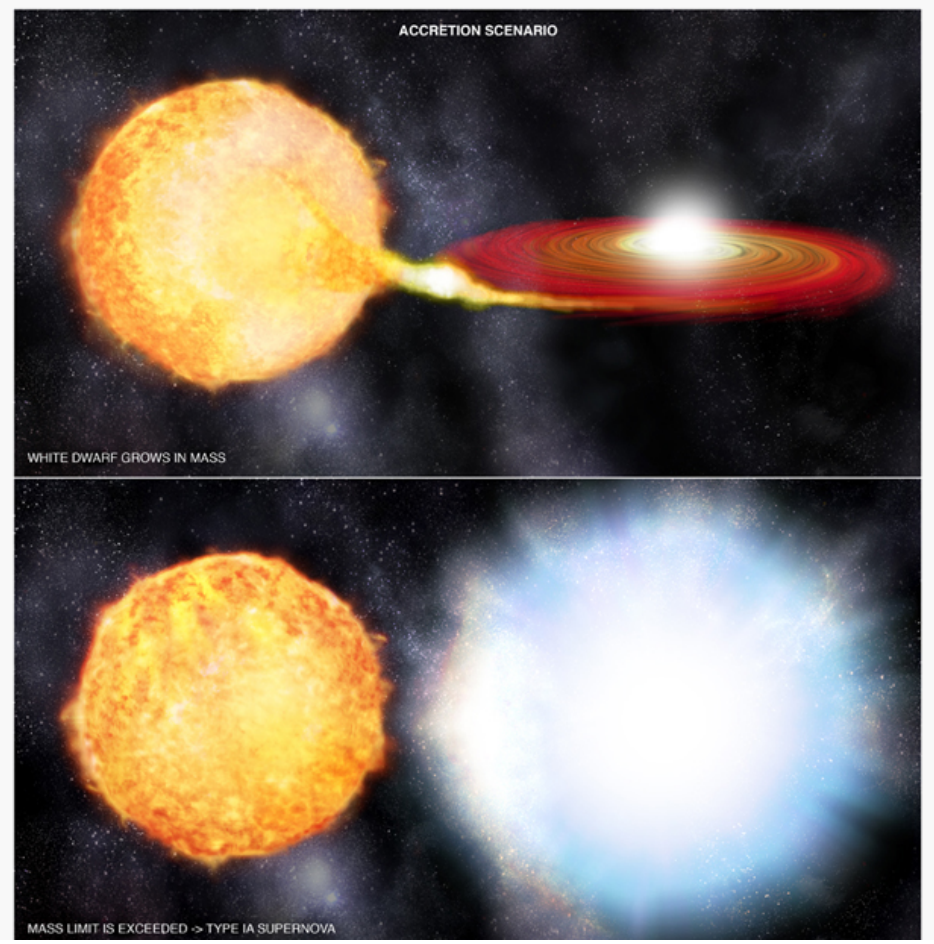

Figure 3.1. Artistic rendition of a white dwarf accreting enough mass from a main sequence companion star to explode in a Type Ia supernova. Image is taken from [79]

.

resulting in a spectrum that contains UV, optical, and IR lines. Only 10–30 days after the explosion will the ejecta be optically thin and the gamma-ray spectrum be available [80]. Since ^{56}Ni has a half life of 6 days (see [3]), the gamma rays produced by the decays of the population of ^{56}Ni cannot be directly observed. Rather, a gamma ray spectrum will only be available once the population of ^{56}Co, which has a half life of approximately 77 days (see [3]), is decaying into ^{56}Fe. The decay of ^{56}Co into ^{56}Fe occurs with an intensity of 100% and produces ^{56}Fe in an excited state 100% of the time [3]. The nuclei of the ^{56}Fe population will deexcite to its ground state by emitting photons. The gamma ray spectra produced by

these nuclear deexcitations will be dominated by the transition from the second excited 4+ state to the first excited 2+ state and the transition from the first excited 2+ state to the 0+ ground state [3], [4]. This is due to the fact that after the decay of ^{56}Co, a gamma ray of energy 1238 keV is produced in 66.46% of the time and a gamma ray of 847 keV is produced 99.94% of the time [3]. Taking this into account, along with when SN 1991T was observed (two 14 day periods 66 and 176 days after the explosion and when the ejecta is optically thin [5]), the relaxation of the ^{56}Fe nucleus to its ground state will be the gamma ray production process considered in this work. This places an emphasis on gamma rays produced with energies approximately 1238 keV and 847 keV, since these are the energies that correspond to the dominant transitions.

The gamma ray lines that correspond to Dirac peaks in the laboratory will appear as curves with some width based on the velocity of the ejecta. There are two possibilities assuming a symmetric ejecta shape, which is a common first-order approximation to make for a Type Ia supernova. The first possibility of the line profile is a flat-topped peak (see Figure 3.2). This occurs when an ejecta layer is optically thin and acts like a shell with an outer region of higher density and an inner region of lower density. The second possibility is the line profile appearing as a parabolic curve (see Figure 3.3). This occurs in an ejecta layer where the density is similar at every point within the layer. The radioactive layer where the formation of new elements occurs in Type Ia supernovae does not behave as a shell, but a dense layer of material. Therefore, the true line shape will be in the form of a parabolic curve. These parabolic line profiles from the radioactive layer are expected to correspond to Gaussian peaks (see ^{56}Co template in [5]) in the observing detector and subsequent data analyses assume a Gaussian line profile when observing in the appropriate energy regime. This is due to the fact that the energy resolution of gamma ray detectors is not small relative to the energy width caused by Doppler broadening (which will be shown after the 91T data has been fit). For these Gaussian line profiles, the line energy corresponds to the centroid of the peak and is not shifted by the line broadening.

The line energy will be affected by the redshift caused by the host galaxy's motion relative to the Milky Way. It shall be seen in the coming chapters that a light pseudoscalar field that

acts as dark energy and interacts with the iron nucleus can also possibly induce an energy shift in the detected gamma rays of Type Ia supernovae.

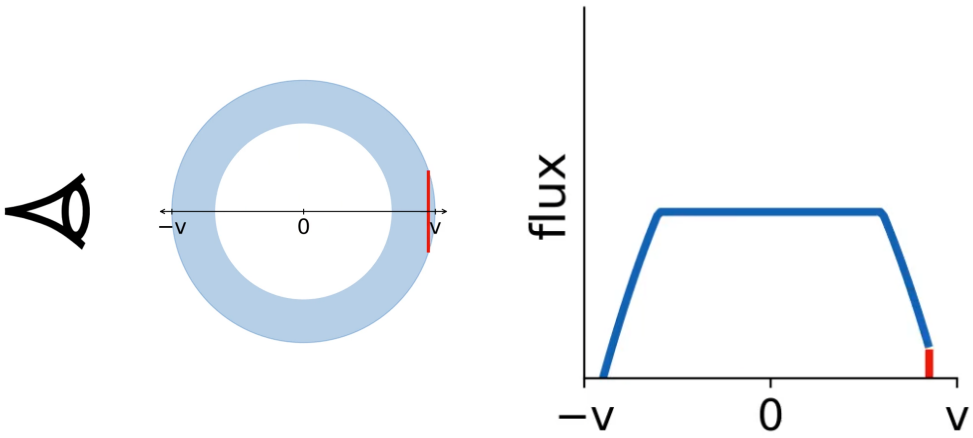

Figure 3.2. Line shape for ejecta layer that behaves as a hollow spherical shell. The width of detected lines, which are in units of energy, will correspond to the velocity (v) of the ejecta in both directions. The ejecta on the near side of the star will travel closer to the point of observation and cause a blueshift of any light emitted. The ejecta on the far side of the star will move farther from the point of observation and cause a redshift of the light emitted. These images are contained in a seminar by Dr. Lindsey Kwok and are used with permission [81].

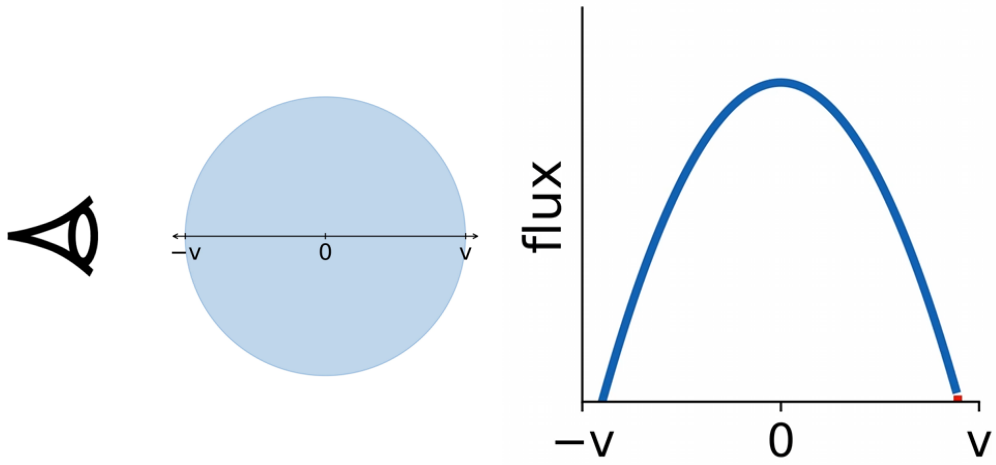

Figure 3.3. Line shape for ejecta layer that behaves as a sphere, which is more applicable to the radioactive layer. The width of detected lines, which are in units of energy, will correspond to the velocity (v) of the ejecta in both directions. The ejecta on the near side of the star will travel closer to the point of observation and cause a blueshift of any light emitted. The ejecta on the far side of the star will move farther from the point of observation and cause a redshift of the light emitted. These images are contained in a seminar by Dr. Lindsey Kwok and are used with permission [81].

4. THEORY

The theoretical foundation on which this work is based is described in this chapter. First described is the study of the variation of fundamental constants that started with the observation of quasars. This has been extended to different systems such as atoms and nuclei. In this regard, the variation of the pion mass is detailed. Two different nuclear models (i.e. the rigid rotor and the vibrating liquid drop) and the relevant equations are given next so that any observed gamma ray energy deviation can be related to a quintessence field in an unambiguous way. The theoretical uncertainty of these models is calculated based on how their predictions compare to observation. Explicit expressions are derived for the upper limit of $\dot{Q}$ for each model. These expressions will depend on two free parameters, the constant term of the field that correspond to the cosmological constant and the decay constant of the field Q. The choice made for these parameters and the reasons are given in the final section of this chapter.

4.1 The Variation of Fundamental Constants

The study of the variation of fundamental constants began after the claim that the fine structure constant was smaller in the past, as indicated by the absorption spectra of quasars [82]. The variation of the fundamental constants in physics has become closely tied to the study of physics beyond the standard model. This is due to the fact that new degrees of freedom that change in space or time with couplings to the known fields of the universe can generate these variations [48]. The study of systems associated with the fundamental constants assists in the detection of these new degrees of freedom and the creation of experimental limits on the parameters of these new fields. Specifically, from a cosmological viewpoint, the variation of constants permits the quantification of deviations from General Relativity and/or the revelation of the nature of dark energy [48].

This idea has been extended to the atomic and nuclear transition frequencies of different elements. It has been suggested that the transition frequencies depend on the nuclear charge radius, which can possibly be affected by an interaction with a scalar or pseudoscalar field

[8]. The deviations of the nuclear radius would come as a result of deviations of the hadron masses, which implies [12]

$$\frac{\delta r_0}{r_0} = \sum_h K_h \frac{\delta m_h}{m_h}, \tag{4.1}$$

where h is the hadron species, m_h is the hadron mass, and K_h is a sensitivity constant. The value of r_0 is 1.2 femtometers and is used to determine the radius of different nuclei through the relation $R_0 = r_0 A^{1/3}$. In turn, the variation of the hadron masses can be related to the variation of the quark masses by the equation [83]

$$\frac{\delta m_h}{m_h} = K_{h,q} \frac{m_q}{m_q}, \tag{4.2}$$

where $K_{h,q}$ is the sensitivity coefficient for the quarks, and m_q is the average of first-generation quark masses. The advantage of considering mass variations at the quark level is that the resulting radial variation from multiple sources can be represented by a single term with a constant coefficient. For example, the variation in the nuclear radius depends on how strongly the nucleons are interacting, which is represented by the pion mass, and how difficult it is to move the nucleons, represented by the mass of the individual nucleons. These two effects are quantified by the equation [12]

$$\frac{\delta r_0}{r_0} = 1.8 \frac{\delta m_\pi}{m_\pi} - 4.8 \frac{\delta m_N}{m_N}, \tag{4.3}$$

where m_π is the mass of the pion and m_N is the nucleon mass. However, the above relation reduces to

$$\frac{\delta r_0}{r_0} = 1.2 \frac{\delta m_\pi}{m_\pi}, \tag{4.4}$$

after relating the nucleon mass to the pion mass through their quark structure [12]

$$\frac{\delta m_N}{m_N} = 0.13 \frac{\delta m_\pi}{m_\pi}. \tag{4.5}$$

The specific fundamental constant that is relevant to this study is the mass of the pion (m_π). It is assumed that a new ALP degree of freedom acting as a quintessence-like field has

interactions with the nuclei of atoms. This assumption necessitates the coupling of the new field to the QCD vacuum term

$$\mathcal{L}_\theta = \theta \frac{g_S^2}{32\pi^2} \tilde{G}^{l\mu\nu} G_{l\mu\nu}, \tag{4.6}$$

where g_S is the coupling constant of the strong force, θ is the QCD vacuum angle, $G_{l\mu\nu}$ is the gluon field strength tensor, and $\tilde{G}^{l\mu\nu}$ is its dual [8]. The new field is not explicit in the equation above; however, just like the QCD axion, a new light pseudoscalar (ALP) field can, in principle, contribute to the small value of θ [10]. In fact, this additional pseudoscalar field will have a very small mass in this scenario, which makes the small mass (10^{-33} eV) required for a field to act as dark energy achievable by particle physics processes [10]. Since the pion mass depends on the QCD vacuum angle through

$$m_\pi^2 = \frac{2B_0}{f_\pi^2}(m_u^2 + m_d^2 + 2m_u m_d \cos\theta)^{1/2}, \tag{4.7}$$

where B_0 is a constant determined by the ratio of meson masses and has value 7.6×10^6 MeV^3, m_u and m_d are the masses of the up and down quarks taken to be 4 MeV and 7 MeV, respectively, and f_π is the pion decay constant, which has value 92.4 MeV. The coupling in Equation (4.6) is found to imply (see [8] and [11]) that the mass of the pion changes as

$$\frac{\delta m_\pi}{m_\pi} \approx -0.05\theta^2. \tag{4.8}$$

Equations (4.7) and (4.8) are derived in Appendix A. Attributing the entire value of the vacuum angle to the ALP dark energy field by $\theta = Q/f_Q$ (which is akin to what is done for axion dark matter [11], [12]), where f_Q is the decay constant of the field generates an upper limit on $\dot{Q}$. Expanding θ^2 to first order in $\dot{Q}$ yields

$$\frac{\delta m_\pi}{m_\pi} = -0.05\frac{Q^2}{f_Q^2} \approx -0.05\frac{(Q_\Lambda + \dot{Q}\Delta t)^2}{f_Q^2} = -\frac{0.05}{f_Q^2}\left(Q_\Lambda^2 + 2Q_\Lambda \dot{Q}\Delta t\right). \tag{4.9}$$

Once a nuclear model is chosen, the above expression permits a relation between the deviation of gamma ray energies to the time evolution of the quintessence field $\dot{Q}$.

4.2 Nuclear Models

Type Ia supernovae contain the characteristic decay of ^{56}Co into ^{56}Fe by the process of electron capture. Even for intermediate-mass nuclei such as these elements, nuclear dynamics and interactions become complex enough that the nuclear shell model is no longer convenient for predicting the energies of the excited states. The nuclear shell model is an analogy to the atomic shell model where valence nucleons orbit an inert nucleon core. Rather, it is much more transparent to understand the excited states of these nuclei through the collective motion of the nucleons of which they are comprised. To this end, there are two main models of the nucleus that are commonly employed. The first is a classical rotational model developed for the case that the nucleus is permanently deformed and free to rotate [84]. The second is a quantum mechanical vibrational model where the surface of the nucleus is free to vibrate and associated with the creation of phonons [85]. In a rotational frame centered on the nucleus, the nucleus will appear deformed, demonstrating the equivalency of these two models.

4.2.1 Nucleus as a Rigid Rotor

Nuclei that contain unpaired nucleons orbiting outside of closed shells have their nuclear properties determined by these valence nucleons and are best described using single particle models. However, as the number of nucleons increase outside of closed shells, so too does the number of ways the angular momenta can couple making the determination of the energies of these quantum states a complex task. Experimentally, the excited states of these nuclei exhibit a complicated structure of their spectra especially at the higher excited states. This structure, along with nuclear scattering data and the large difference in the expected and measured quadrupole moments, suggests that the shape of the nucleus (above $A \sim 150$) in the ground state is increasingly deformed from a spherical shape as more nucleons are added to unclosed shells [84]. The simplest excited states of these nuclei are represented by imbuing them with angular momentum which is associated with the classical energies of [84]

$$E = \frac{1}{2}\mathcal{I}\omega^2 = \frac{J^2}{2\mathcal{I}}, \tag{4.10}$$

where ω, $\mathcal{I}$, and J are the angular speed, moment of inertia, and angular momentum of the nucleus, respectively. However, the nucleus is comprised of quantum particles, so the appropriate quantum mechanical version of Equation (4.10) must be used

$$E = \frac{\hbar^2 J(J+1)}{2\mathcal{I}}. \tag{4.11}$$

The above equation can be used to predict the energies for the first few excited states of even-even nuclei, corresponding to low values of J. The quantum number J is restricted to even values to account for the mirror symmetry of the nuclear wavefunctions [84]. Therefore, the first excited state of ^{56}Fe corresponds with $J = 2$ and the second excited state corresponds with $J = 4$.

The moment of inertia of a rigid nucleus in the shape of an ellipsoid to lowest order in the deformation parameter (β) is [84]

$$\mathcal{I}_{rig} = \frac{2}{5} AmR_0^2(1 + 0.31\beta), \tag{4.12}$$

where A is the nuclear mass number, m is the proton mass, and R_0 is the nuclear charge radius of the spherical configuration which is given by $R_0 = r_0 A^{1/3}$ where $r_0 = 1.2$ fm. For a nucleus that is modeled as a deformed frictionless fluid, the moment of inertia of the ellipsoid is [84]

$$\mathcal{I}_{irrot} = \frac{9}{8\pi} AmR_0^2\beta^2. \tag{4.13}$$

The moment of inertia for the relevant nuclei is experimentally determined to be between these two extremes [84]. The ratio between the experimental moment of inertia ($\mathcal{I}$) and $\mathcal{I}_{rig}$ can be determined by the deformation parameter (see Figure 17.22 of [84]).

Since the deformation parameter must be known to ultimately determine the energy levels of the excited states of deformed nuclei, a well-measured quantity related to the deformation must be utilized. This quantity is the intrinsic quadrupole moment of the nucleus [84]

$$Q_0 = \frac{3}{\sqrt{5\pi}} ZR_0^2\beta(1 + 0.16\beta), \tag{4.14}$$

where Z is the atomic number. It is now possible to predict the energies associated with the different excited states with multiple nucleons in an unclosed shell using these expressions.

4.2.2 Nucleus as a Vibrating Liquid Drop

An alternative to the classical model described in the previous section is the quantization of the liquid drop model. This model likens the nucleus to a charged liquid drop made of nucleons which is free to vibrate about the equilibrium shape of a sphere [85]. The low-lying excited states of even-even nuclei are best understood by the excitations of the nucleons in the unclosed outer shell, which can be thought of as a vibration of the surface of the nucleus, rather than the vibrations of the inner layers of the liquid drop [84]. The energies of these excited states are associated with the frequencies and number of phonons that represent the vibrations of the nuclear surface. The surface of the nucleus is given in terms of the spherical harmonic functions as[85]

$$R(\theta,\phi) = R_0\left(1+\sum_{\lambda=0}^{\infty}\sum_{\mu=-\lambda}^{\lambda}\alpha_{\lambda\mu}(t)Y_\lambda^\mu(\theta,\phi)\right), \tag{4.15}$$

where $\alpha_{\lambda\mu}(t)$ are time-dependent deformation parameters. The index λ corresponds to quadrupole ($\lambda = 2$), octupole ($\lambda = 3$), and hexadecupole ($\lambda = 4$) vibrations. $\lambda = 0$ and $\lambda = 1$ correspond to radial oscillations and translations respectively. These values of λ are excluded since the nucleus is assumed to be incompressible and translations of the center of mass do not correspond to surface deformations [85]. Assuming that the deformation parameters are small, the Hamiltonian for this system takes on the form of a harmonic oscillator [84], [85]

$$H = T + V \approx \frac{1}{2}\sum_{\mu,\lambda} B_\lambda \|\dot{\alpha}_{\lambda\mu}(t)\|^2 + \frac{1}{2}\sum_{\mu,\lambda} C_\lambda \|\alpha_{\lambda\mu}(t)\|^2, \tag{4.16}$$

where B_λ is the inertia of the nucleus and C_λ is the restoring force of the potential. These coefficients are what determine the frequency of the vibrational deformation [85]

$$\omega_\lambda = \sqrt{\frac{\|C_\lambda\|}{B_\lambda}}. \tag{4.17}$$

For an irrotational incompressible fluid these coefficients were found by Rayleigh to be [85], [86]

$$B_{\lambda,irr} = \frac{\rho R_0^5}{\lambda}, \quad C_{\lambda,irr} = C_\lambda^{(1)} - C_\lambda^{(2)}, \tag{4.18}$$

where

$$C_\lambda^{(1)} = SR_0^2(\lambda-1)(\lambda+2), \quad C_\lambda^{(2)} = \frac{3}{4\pi}\frac{Z^2e^2}{R_0}\frac{\lambda-1}{2\lambda+1}. \tag{4.19}$$

Above, ρ is the nuclear mass density for the spherical configuration, e is the fundamental charge, and S is the surface energy per unit area [17]. The value of the final quantity in this list is found using the coefficient of the $A^{2/3}$ in the semi-empirical mass formula. Using the known values of the mass density and only considering quadrupole vibrational deformations ($\lambda = 2$) the coefficients become

$$B_{2,irr} = \frac{3}{8\pi}mAR_0^2, \quad C_{2,irr} = 4R_0^2S - \frac{3}{20\pi}\frac{Z^2e^2}{R_0}. \tag{4.20}$$

The quantization of these vibrations leads to phonons with energies [85]

$$E_N = N\hbar\omega_2, \tag{4.21}$$

where N is the number of phonons. It has become convention to associate the first, second, third... excited states with one, two, three... phonons [84]. Relevant to the study are the first and second excited states of ^{56}Fe which coincides with $N = 1$ and $N = 2$ respectively.

There are now two expressions from two different models of the excited states that can be used to relate any energy deviations indicated by the spectroscopic data from SN1991T to the quintessence field.

4.2.3 Theoretical Uncertainty

The models of the preceding sections cannot be used to predict the energies of excited nuclei outright. This is because nuclei, especially those of higher mass numbers, are extremely complex objects where a single nucleon experiences a high number of interactions with its neighbors. For this reason, the predicted energies given by Equations (4.11) and (4.21) must be complemented by the experimental determination of key parameters, namely $\beta, \mathcal{I}, C_2$, and B_2, to correctly match the energies of the excited states that are surmised by energies of emitted gamma rays. Since this analysis works specifically with the ^{56}Fe nucleus, the theoretical uncertainty will be found by comparing the predicted energies to the observed energies of the excited states of this iron isotope. A level diagram of ^{56}Fe can be seen in Figure 4.1.

The ^{56}Fe nucleus was determined to have a deformation $\beta = 0.2461$ [87]. This deformation corresponds to an experimental moment of inertia $\mathcal{I} \approx 0.30\mathcal{I}_{rig}$ (see Figure 17.22 of [84]). The first excited state ($J = 2$), modeling the nucleus as a rigid rotor ($\mathcal{I}_{rig} = 1.22 \times 10^4$ GeV^{-1}), is predicted to have energy

$$E_{2,rig} \approx 817 \text{ keV}, \tag{4.22}$$

whereas the measured energy of the first excited state is [3]

$$E_{2,meas} \approx 847 \text{ keV}. \tag{4.23}$$

This discrepancy increases for the second excited state ($J = 4$). The predicted energy is

$$E_{4,rig} \approx 2.72 \text{ MeV}, \tag{4.24}$$

which can be compared to the measured energy of [3]

$$E_{4,meas} \approx 2.08 \text{ MeV}. \tag{4.25}$$

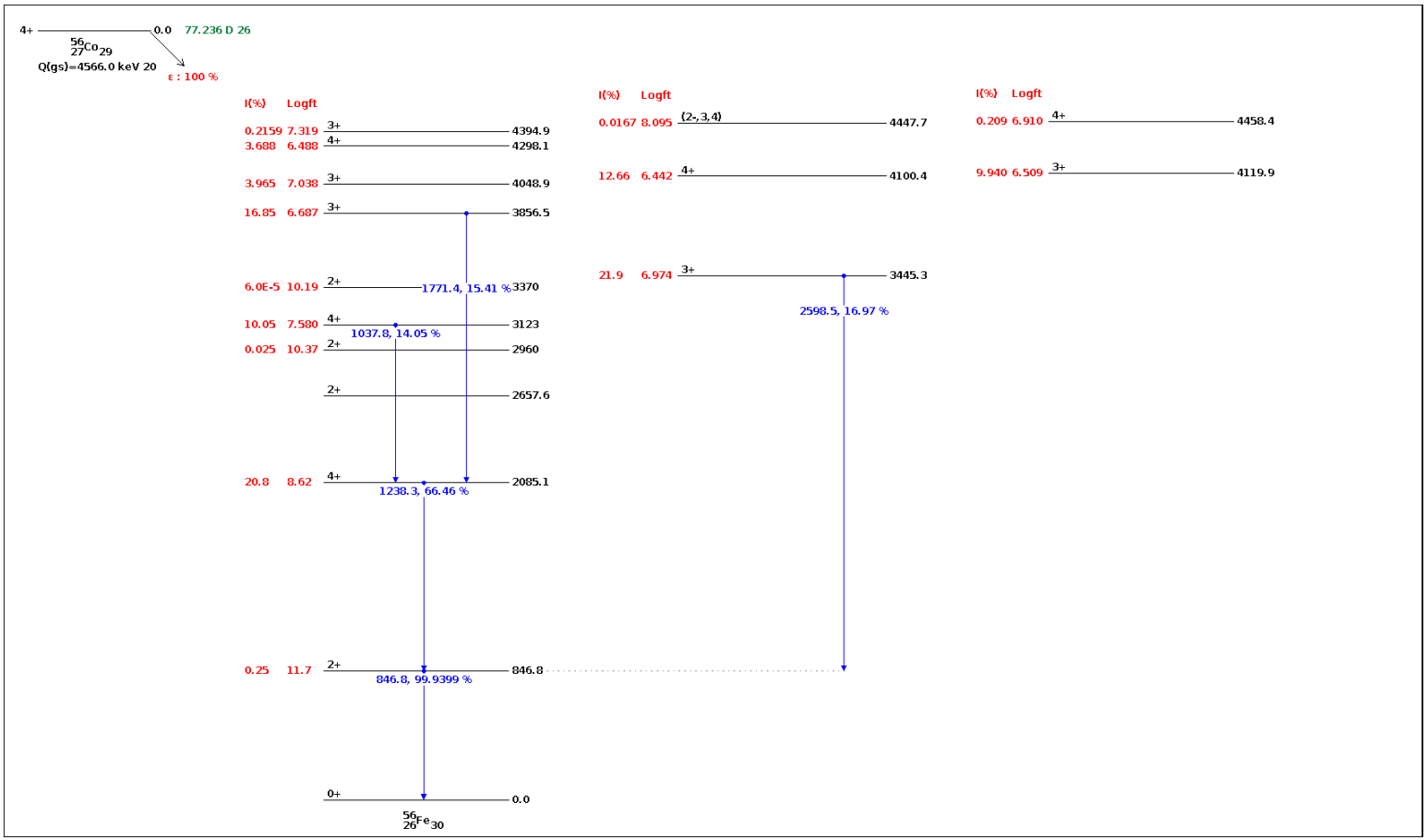

Figure 4.1. The level diagram of ^{56}Fe depicting the energies of its excited states in keV for transitions with a probability at and above 10%. As can be seen in the figure, ^{56}Co (on the left side of the figure) decays into an iron nucleus via electron capture into an excited state of ^{56}Fe. The relative intensity, given as a percentage, of the excited state produced from these decays are the red values to the left of the ^{56}Fe states. The excited iron daughter nucleus deexcites to its ground state by emitting gamma rays. The transition energies and their relative intensities are given by the values in blue between the ^{56}Fe in units of keV and as a percentage, respectively. The gamma ray spectra will be dominated by the 1238 keV and 847 keV transitions based on their relative intensities. This image is taken from [3].

This results in a difference of

$$\Delta E_{4,rig} \approx 640 \text{ keV}. \tag{4.26}$$

The origin of this large discrepancy is the approximation, used in this work, that the nucleus is permanently deformed and that this deformation is the same for all excited states. However, this is not necessarily true as the second excited state may have a different deformation and moment of inertia. This is implied by the inclusion of two different deformation parameters presented in [87].

Modeling the nucleus of ^{56}Fe as a vibrating liquid drop, the restoring force C_2 was determined to be approximately 40 MeV and the experimental inertia of the nucleus $B_2 \approx 15 B_{2,irr}$ [88]. The first and second excited states, which have one phonon and two phonons ($N = 1, 2$) respectively, are predicted to have energies of ($B_{2,irr} \approx 3.39 \times 10^3$ GeV^{-1})

$$E_{1,phon} \approx 894 \text{ keV}, \quad E_{2,phon} \approx 1.79 \text{ MeV}, \tag{4.27}$$

making the discrepancy between the predicted and measured energies of the second excited state

$$\Delta E_{2,phon} \approx 295 \text{ keV}. \tag{4.28}$$

The origin of this discrepancy comes from the fact that the second excited state is not a 2+ state but a 4+ state. The use of ω_2 corresponds to 2+ states and using $E_2 = 2\hbar\omega_2$ corresponds to the second excited 2+ state, which, in general, have lower energies than the corresponding second excited 4+ state. The theoretical uncertainty is taken to be the average of these two larger energy discrepancies for the second excited states which is

$$\Delta E_{theor} \approx \pm 470 \text{ keV}. \tag{4.29}$$

This value of the disagreement between the predicted and measured energies of the second excited ^{56}Fe is assumed to be the uncertainty on the percentage difference of the nuclear radius $\delta r_0/r_0$. The explicit value of the theoretical uncertainty is then determined to be

$$\frac{\delta r_0}{r_0} \pm \frac{\Delta E_{theor}}{E_2} = \frac{\delta r_0}{r_0} \pm 0.38. \tag{4.30}$$

However, 38% will result in theoretical uncertainties that are at least an order of magnitude larger than the results indicated by the fitting of the SN 1991T data. These uncertainties are too large to indicate anything useful for the results derived here. If a shell model was used for this analysis, there are indications that the discrepancy would grow. The theoretical treatment of the ^{8}Be nucleus employing a shell model approach results in a discrepancy of approximately 8 MeV between the predicted and measured values of its ground state energy [89]. Due to the large values of the associated theoretical uncertainties relative to the results derived here, and the difficulty in accurately predicting theoretical uncertainties that are comparable to the results derived, only the fit uncertainties will be included in the reported values. This is an approach taken in other analyses of quark mass variations for the same reasons given above, which suggests that the associated calculations can be considered 'order of magnitude estimates' (see [90]).

4.3 Relation Between Gamma Ray Energy Deviations and $\dot{Q}$

Due to the possible interaction of a new ALP degree of freedom with nucleons, it has been demonstrated that variations in the nuclear charge radius and nucleon mass will take place [11], [91]. Since the energies of gamma rays emitted from excited nuclei depend on the nuclear radius (see previous section), this will introduce a deviation in the energies of these gamma rays. This section will derive the explicit expressions that relate these energy deviations to the time-varying part of the quintessence field for the model of the nucleus as a deformed rigid rotor and vibrating liquid drop. The general prescription is to utilize the equations for the energies of each model to find its percentage difference in terms of the radial percentage difference over a finite time, insert the equations relating the variation of the nuclear radius to the variation in the pion mass, and use the dependence of the pion mass

on the QCD vacuum angle to generate a relation that is dependent on $\dot{Q}$. These expressions will depend on Q_Λ and f_Q. The values chosen for these quantities and the reasoning will be presented here.

4.3.1 Energy Deviation for the Rigid Rotor

The energy of an excited state of the nucleus as a rigid rotor with angular momentum J is

$$E = \frac{\hbar^2 J(J+1)}{2\mathcal{I}}. \tag{4.31}$$

Plugging in the moment of inertia of an ellipsoid, given in Equation (4.12), yields

$$E = \frac{5\hbar^2 J(J+1)}{4A^{5/3}M(1+0.31\beta)}\frac{1}{r_0^2}. \tag{4.32}$$

The variation of the energy with respect to r_0 is

$$\delta E = -\frac{5\hbar^2 J(J+1)}{2A^{5/3}M(1+0.31\beta)}\frac{1}{r_0^3}\delta r_0 \tag{4.33}$$

which is reduced to the very simple equation

$$\frac{\delta E}{E} = -2\frac{\delta r_0}{r_0}. \tag{4.34}$$

This energy deviation in terms of the QCD angle, using Equations (4.4) and (4.8), is

$$\frac{\delta E}{E} = -2.4\frac{\delta m_\pi}{m_\pi} = 0.12\theta^2. \tag{4.35}$$

Assuming the value of the QCD vacuum angle is entirely due to the ALP dark energy field, using Equation (4.9), produces

$$\frac{\delta E}{E} = \frac{0.12}{f_Q^2}\left(Q_\Lambda^2 + 2Q_\Lambda\dot{Q}\Delta t\right). \tag{4.36}$$

However, the first term is constant and renormalizes all energy levels within the nucleus. This will not produce any observable energy deviations as time evolves. Therefore, it is required to take the derivative of each side of the above equation

$$\frac{1}{E}\frac{dE}{dt} = \frac{0.24}{f_Q^2} Q_\Lambda \dot{Q}. \tag{4.37}$$

Making the approximation that the energy changes at the same rate ($dE/dt \approx \Delta E/\Delta t$) and then rearranging yields the final expression

$$\dot{Q}_{rig} = \frac{f_Q^2}{0.24 Q_\Lambda \Delta t}\frac{\delta E}{E}. \tag{4.38}$$

4.3.2 Energy Deviation for the Nuclear Liquid Drop

The energy of an excited nuclear liquid drop associated with quadrupole ($\lambda = 2$) surface vibrations is represented by a number of phonons (N) as

$$E_N = N\hbar\omega_2, \tag{4.39}$$

where the phonon frequency is determined to be

$$\omega_2 = \varsigma\sqrt{\frac{1}{r_0^2} - \frac{3}{10}\frac{Z^2 e^2}{\varepsilon A^{1/3}}\frac{1}{r_0^3}}, \tag{4.40}$$

after inserting the coefficients given in Equation (4.20). In the above equation, $\varepsilon \equiv 4\pi r_0^2 S$, which is approximately 18.56 MeV [17] and ς is defined as

$$\varsigma \equiv \sqrt{\frac{8\varepsilon}{3mA}}. \tag{4.41}$$

Taking the variation of ω_2 with respect to r_0 yields

$$\delta\omega_2 = -\varsigma\frac{\delta r_0}{r_0}\left(\frac{\frac{1}{r_0^2} - \frac{3}{2}\frac{\xi}{r_0^2}}{\sqrt{\frac{1}{r_0^2} - \frac{\xi}{r_0^2}}}\right), \tag{4.42}$$

where ξ is defined to be

$$\xi \equiv \frac{3}{10}\frac{Z^2 e^2}{\varepsilon A}\frac{1}{r_0}. \tag{4.43}$$

Dividing both sides by ω_2 results in

$$\frac{\delta E}{E} = \frac{\delta \omega_2}{\omega_2} = -\frac{(1-3/2\xi)}{(1-\xi)}\frac{\delta r_0}{r_0}. \tag{4.44}$$

After inserting the appropriate expressions for the variation of the pion mass and its dependence on the QCD vacuum angle, using the approximation that the change in energy is the same each year, and rearranging, $\dot{Q}$ is found to be

$$\dot{Q}_{phon} = \frac{f_Q^2}{0.12 Q_\Lambda \Delta t}\frac{(1-\xi)}{(1-3\xi/2)}\frac{\delta E}{E}. \tag{4.45}$$

Due to the similarity between Equations (4.38) and (4.45), a general form of the upper limit for $\dot{Q}$ can be written as

$$\dot{Q}_{\rm i} = \eta_{\rm i}\frac{f_Q^2}{Q_\Lambda \Delta t}\frac{\delta E}{E}, \tag{4.46}$$

where i = 1 corresponds to the nucleus as a rigid rotor and i = 2 corresponds to the nucleus as a vibrating liquid drop. This implies that the values of $\eta_{\rm i}$ are given by

$$\eta_1 = \frac{1}{0.24}, \quad \eta_2 = \frac{1}{0.12}\left(\frac{1-\xi}{1-3\xi/2}\right) \tag{4.47}$$

4.4 Choice of Parameters

The resulting upper limits on $\dot{Q}$ found in the previous section require values for the field's decay constant, f_Q, and the term of the field that corresponds to the cosmological constant, Q_Λ. This section contains the assumptions being made and the choice for the values of these parameters. The energy deviation, $\delta E/E$, will be determined from the analysis of SN 1991T spectroscopic data in the next chapter.

4.4.1 Q_Λ

A large majority of the measurements of the dark energy equation of state parameter are consistent with a cosmological constant ($w_\Lambda = -1$) with some possibility for the equation of state to deviate from this value [66]–[68]. To be consistent with this observation, it is assumed that the energy density of the quintessence field, given by Equation (3.7), is dominated by the quintessence potential $V(Q)$

$$\rho_Q \approx V(Q_\Lambda). \tag{4.48}$$

The argument of the potential is given by Q_Λ instead of Q because the contribution of $\dot{Q}$ to the potential will be very small. It is useful to use

$$\rho_Q = \Omega_\Lambda \rho_{crit}, \tag{4.49}$$

where Ω_Λ is the percentage of the energy density of dark energy and has value 0.685 [72] and ρ_{crit} is the critical energy density given by

$$\rho_{crit} = \frac{3H_0^2}{8\pi G}. \tag{4.50}$$

Here H_0 is the present-day value of the Hubble expansion rate.

One of the goals in developing a quintessence model is to alleviate the fine-tuning and coincidence problem of the cosmological constant as well as the discrepancy between the measured and expected values of the dark energy density caused by this model [31]–[33]. In order to not lose this desired characteristic of quintessence models, the simple form of a tracking potential derived by Ratra and Peebles will be utilized

$$V(Q_\Lambda) = \frac{M^{4+p}}{Q_\Lambda^p} = \frac{(8\pi G)^{-1-p/2} H_0^2}{Q_\Lambda^p}, \tag{4.51}$$

where G is Newton's gravitational constant and p is the power for the power-law potential. In the last equality, Equation (3.15) was used to allow for the slow evolution of the quintessence field. Plugging all of these equations back into Equation (4.48) and solving for Q_Λ yields

$$Q_\Lambda = \frac{1}{\sqrt{8\pi G}} \frac{1}{(3\Omega_\Lambda)^{1/p}} = \frac{M_{pl}}{\sqrt{8\pi}} \frac{1}{(3\Omega_\Lambda)^{1/p}}, \tag{4.52}$$

where M_{pl} is the (unreduced) Planck mass and has value 1.22×10^{19} GeV. In the last equality, the relation $G = 1/M_{pl}^2$ is used since $\hbar = c = 1$.

4.4.2 f_Q

The results of string theory suggest that a light pseudoscalar degree of freedom can act as dark energy if the mass of that pseudoscalar is 10^{-33} eV [16]. To ensure that this mass is generated by the quintessence field, the decay constant is taken to be

$$f_Q = \alpha M_{pl}/\sqrt{8\pi}, \tag{4.53}$$

where alpha is a coefficient of order 0.1. In fact, string constructions indicate that the coefficient can get as low as order 0.001 for dark energy and dark matter [92]. This is a common choice for ALP quintessence models (see [14], [45], [46], [60], [93]) due to the fact that this is the energy scale with which new physics is associated. ALP quintessence models have two notable successes associated with them. The first is that they are able to reproduce the surmised energy density of dark energy (specifically in the case of Electroweak Dark energy [93]) of

$$S_I = 10^{-122} M_{pl}^4, \tag{4.54}$$

where S_I is the vacuum energy indicated by the action of the Electroweak Axion. The second success of these models is that they provide an opportunity to resolve the Hubble tension [46] (see reference [36] for a review of the Hubble tension). Since this work operates on the basis that dark energy is an ALP field, and to possibly preserve the advantages of similar models, Equation (4.53) will be used for the decay constant of the quintessence-like field.

5. DATA ANALYSIS

This chapter provides a description of how a value for $\delta E/E$ is generated, the final quantity needed to produce an upper limit on $\dot{Q}$. Brief descriptions are given for SN 1991T, which is the stellar event used for this work, as well as COMPTEL, the instrument that observed SN 1991T. The best fits of the background-subtracted data are provided and described in Sections 5.4 and 5.5. Representative values of the upper limits of $\dot{Q}$ and the allowed $\alpha - p$ parameter spaces, indicated by observation, for each nuclear model are given in the final two sections. Existing limits for the quark and pion mass variations, which this work hinges on, are provided in table form so that the limits produced here can be compared and put into perspective. The best limits are derived from studies of the Oklo natural nuclear reactor. Key differences between this work and Oklo analyses are elaborated upon since the limit generated here is not expected to be as low as Oklo's.

5.1 SN 1991T

The astrophysical event utilized for this study is SN 1991T, a Type Ia supernova detected on April 13, 1991 in the host galaxy NGC 4527 at approximately 13.5 Mpc [1]. Type Ia supernovae occur when a white dwarf accretes enough mass from its companion star to reach the Chandrasekhar limit and are characterized by the absence of hydrogen and helium in their spectra with a distinct absorption line near 6100 Å[2]. However, due to the peculiar properties of SN 1991T, a new subtype of Type Ia's referred to as 91T-like supernovae was introduced. Supernovae of this subtype (along with 91T) have higher luminosities and less homogeneity in their light curves and spectra compared to those of standard Type Ia's [94].

SN 1991T was chosen on account of its distance from earth, which is 13.5 Mpc (44.0 million lightyears). This allows the derivation of limits at least as small as $\sim 10^{-9}$ yr^{-1} in terms of the pion mass variation, summing an energy shift as high as 10%, without sacrificing the approximation that $\dot{Q}$ is constant. This latter point is ensured by the fact that 44 million years is much less than the age of the universe (13.7 billion years). There do exist observed Type Ia's that are much farther from earth than SN 1991T, such as SN Wilson, which is at a distance of approximately 10 billion lightyears ($z = 1.914$) [95]. This distance would

result in an upper limit $\sim 10^{-11}$ under the same assumptions; however, $\dot{Q}$ will no longer be constant and requires a more complex analysis to account for its changes. Furthermore, gamma rays emitted by sources at these large distances will generate a trivial flux since luminosity behaves as $1/r^2$. Considering that the ratio of the luminosities of these objects result in

$$\frac{L_{Wilson}}{L_{91T}} \sim \frac{(44 \times 10^6)^2}{(10 \times 10^9)^2} = 2.0 \times 10^{-5}. \tag{5.1}$$

Assuming that a detector observing SN Wilson has the same instrumentation as COMPTEL implies that this hypothetical instrument would need to be approximately 50,000 times larger, in terms of its surface area, to generate the same flux as COMPTEL observing SN 1991T. The construction of this detector would require an amount of time, money, and labor that makes it an unrealistic project. If one wanted to improve the distance and associated values on the pion mass variation, there are specific actions that could be taken to achieve such. For example, if observing a Type Ia that is 10 times further away than SN 1991T and requiring that the same amount of counts be collected, the observation time could be increased to a little over 36 days and the radius of the detector increased by a factor of three.

5.2 COMPTEL

The instrument that observed SN 1991T was the imaging Compton telescope COMPTEL, one of four instruments aboard the Compton Gamma Ray observatory. COMPTEL orbits the earth at a radius of 450 kilometers and explores phenomena within the energy range of ∼1–30 MeV. A gamma-ray production process that is included in this energy range is nuclear de-excitation which is the process utilized for this study [96]. COMTPEL contains an upper detector array (D_1) of liquid scintillator NE213 and a lower detector array (D_2) of NaI (TI) [97]. Detection occurs when a gamma-ray is Compton-scattered in the upper D_1 detector with a subsequent interaction in the D_2 detector. A schematic of COMPTEL is available in Figure 5.1. The quantities measured are the energy losses in the D_1 and D_2 detectors, the time of flight between the two detectors, the location of the interaction in the two detectors, the shape of the pulse in the D_1 detector, and the time of the entire event. The final two quantities in this list are used for background discrimination [96], [97]. The

instrument is calibrated using the onboard decay of ^{60}Co, producing gamma rays of 1.17 MeV and 1.33 MeV [96]. For a full description of this process, see reference [98]. COMPTEL's large field-of-view, which is one steradian, makes it a source of a large amount of data for studies related to low-energy gamma-rays.

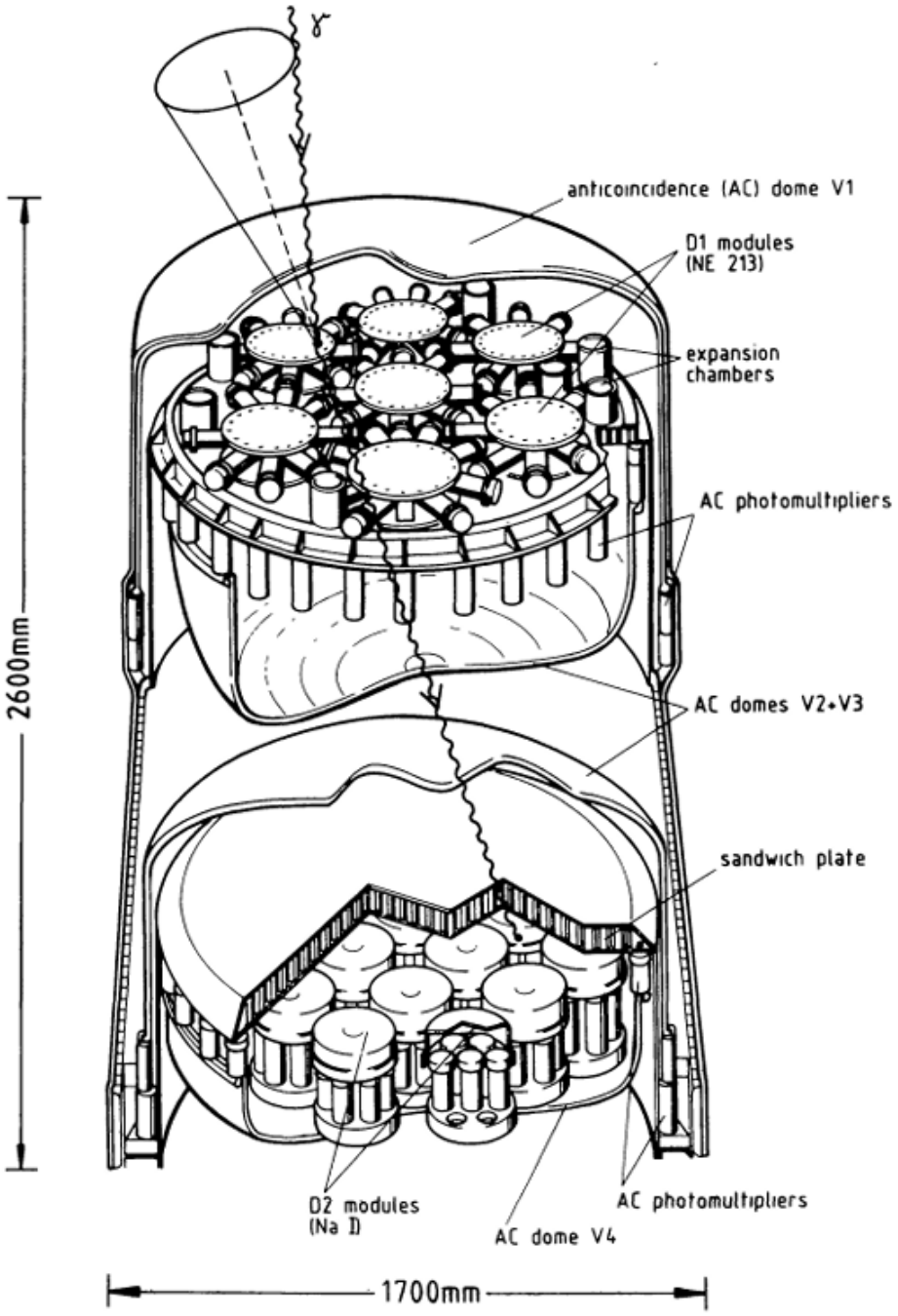

Figure 5.1. A schematic of COMPTEL, the instrument aboard the the Compton Gamma Ray Observatory that observed SN 1991T. Image is taken from [96].

5.3 Energy Resolution Values from Background Model

To correctly predict the width of the upper ^{56}Fe line, the instrumental background and the lower ^{56}Fe line were used. One example of a background model for COMPTEL is given by [5]

$$f_B = a_0(1 - \mathrm{e}^{-b(E-E_0)})\mathrm{e}^{-\alpha E} + a_K \mathrm{e}^{-\frac{1}{2}\left(\frac{E-E_K}{\sigma_K}\right)^2} + a_D \mathrm{e}^{-\frac{1}{2}\left(\frac{E-E_D}{\sigma_D}\right)^2}, \tag{5.2}$$

where the first term is a smooth, exponentially decaying background used to characterize the detectors inherit noise. The second term represents a gamma-ray emission line that consists mainly of the decay of ^{40}K in the components of the spacecraft. The third term is a line due to the formation of deuterium in the COMPTEL D1 liquid scintillator. A plot of the COMPTEL background and its best fit is provided in Figure 5.2. The background best-fit indicates that the widths of the ^{40}K complex and the deuterium peak are 79.123 keV and 77.483 keV, respectively. The width of the lower ^{56}Fe line that was used was 36 keV. These values were used to fit the energy resolution function for the combined scintillation system, which is described below.

The energy resolution function is a combination of both the liquid scintillator and NaI detector systems, which we have characterized as [99]

$$R \equiv \frac{\sigma_\mathrm{i}}{E_\mathrm{i}} = \frac{(\alpha + \beta E_\mathrm{i})^{1/2}}{E_\mathrm{i}}, \tag{5.3}$$

where E_i is the energy of the gamma ray line, α is a noise and offset parameter associated with the detector, and β is a statistical parameter associated with scintillation photon counting and taken to be the square root of the number of counts because the total energy observed is proportional to the square root of the scintillation photon counts in a single event. Using the values of the widths of the potassium complex and the deuterium Gaussian, a fit was made to determine the noise parameter α and the statistical parameter β (See Figure 5.3). Subsequently, the width of the upper iron line was determined from the above resolution function at the energy which it was placed in the best fit. This value was determined to be 76.9 keV and it will be necessary to fix this value before running `Igor` to make the fit consistent with what is known about the instrumentation of COMPTEL.

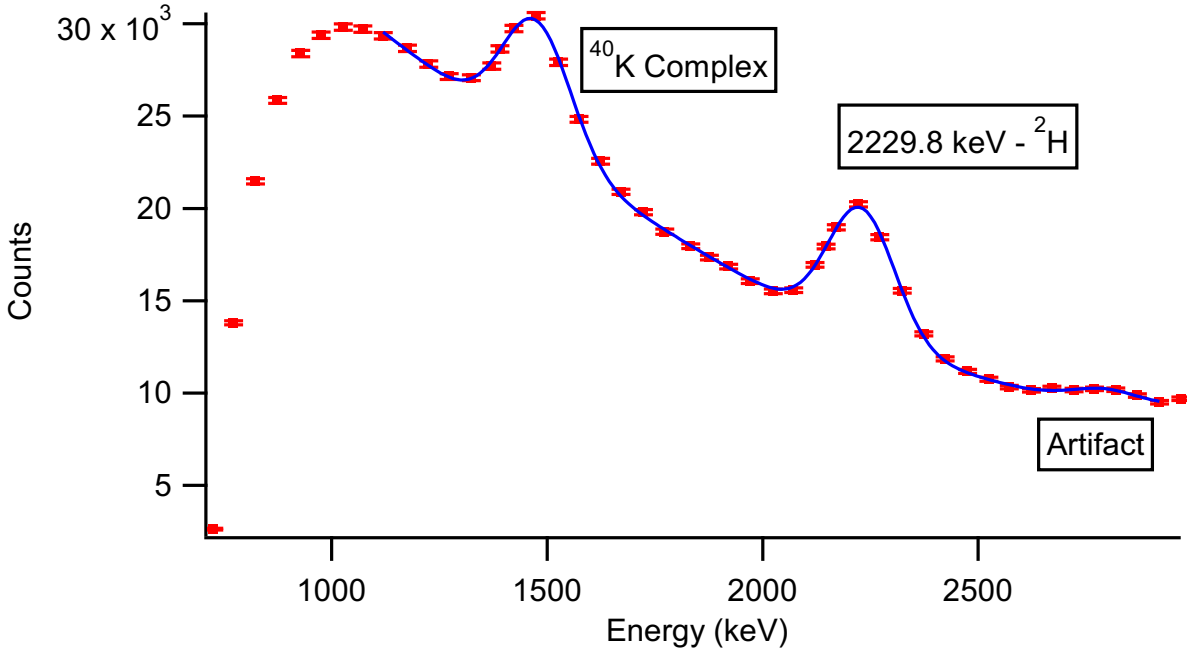

Figure 5.2. Best fit ($\chi^2/DoF \approx 1.35$) of a background model of COMPTEL. This fit was used to determine the value of σ for the upper ^{56}Fe line in the background-subtracted data.

5.4 Resulting Fits

The spectral data of SN 1991T was analyzed to determine the extent to which a quintessence -like field could shift the energies of gamma-rays produced by nuclear processes. SN 1991T was observed for two 14-day periods 66 days and 176 days after the initial supernova explosion [5]. This stellar event was determined to be a peculiar Type Ia supernova at a distance of approximately 13.5 Mpc. This makes SN 1991T a useful candidate for this study since it is known at the $\sim 3\sigma$ level that ^{56}Co nuclei are decaying to produce the observed gamma-ray lines [5] and since it is sufficiently far enough away to provide non-trivial limits. The background-subtracted data was extracted using `WebPlotDigitizer` [100] and then fit using `Igor Pro 9` [6]

Fitting the background-subtracted SN 1991T data, without any constraints on the fitting parameters, yields a best-fit ($\chi^2/DoF \approx 1.29$) with three lines. Two of the lines are are placed

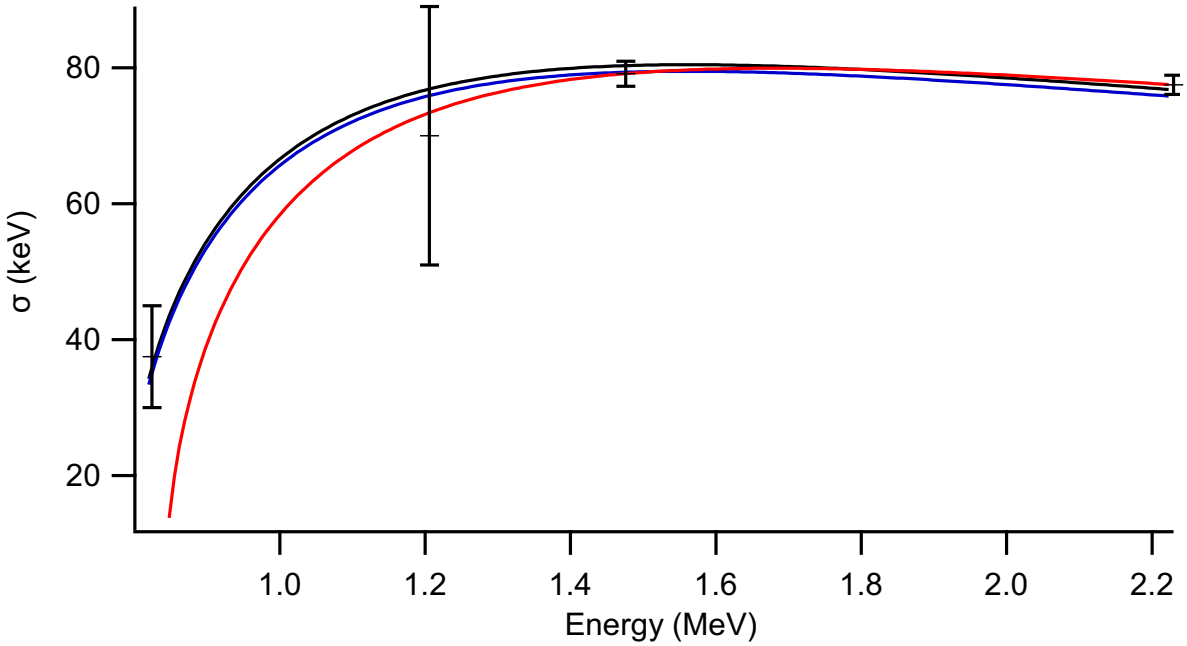

Figure 5.3. Energy resolution versus the line energy fit. The red line is the two point fit for the ^{40}K complex and deuterium. The black and blue lines are both the three point and four point fits which are identical. The three point fit uses the lower iron peak in addition to the two background peaks and the four point uses both iron peaks in addition to the two peaks in the background models. The three and four point fits are offset by 1 keV so that they do not lay on top of one another.

at 824.89 ± 7.78 keV and 1243.6 ± 22.2 keV and correspond to the deexcitations of the ^{56}Fe nucleus (see Figure 5.4). This fit also places a line between the two iron lines at 1117.2 ± 30.9 keV. The existence of this line results from a reduction in the degrees of freedom in the user-defined fitting function compared to the fits excluding the line. The fitting function defined and utilized contains three Gaussian peaks to allow for the an additional line to be produced that is associated with the decay of ^{27}Mg in the instrumentation of COMPTEL [5]. However, this decay produces a 1014 keV gamma ray, meaning that the middle line, which will not be shifted by any astrophysical effect, is placed at too high an energy to be associated with ^{27}Mg. Furthermore, this fit determines the width of this line to be 29.2±27.6 keV, which is completely inconsistent with the energy resolution function of COMPTEL. The

fit of the energy resolution function indicates the width of this line to be ~ 70 keV. For these reasons, this fit is discarded.

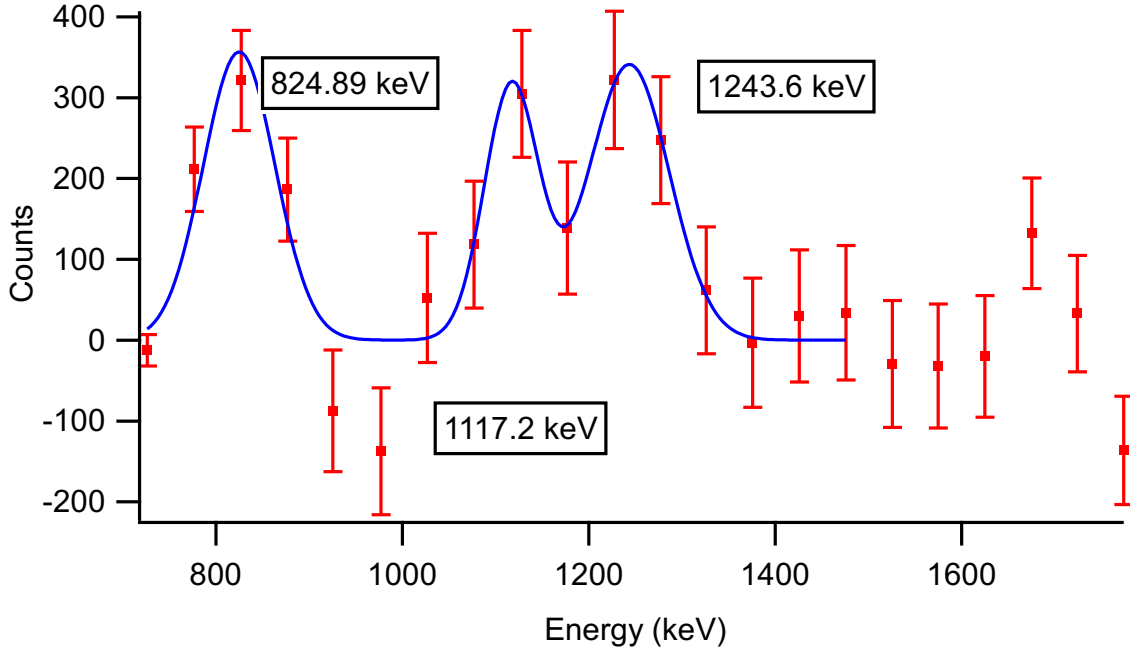

Figure 5.4. Best fit ($\chi^2/DoF \approx 1.29$) of the SN 1991T data. However, this fit is discarded because it does not obey the energy resolution function given in Equation (5.3) and places a ^{27}Mg decay line at an incorrect energy.

Fitting the SN 1991T data after fixing the values of the widths to those determined by utilizing Equation (5.3) and fixing the position of the ^{27}Mg at 1014 keV results in the best fit ($\chi^2/DoF \approx 1.42$), provided in Figure 5.5. In this fit, the two ^{56}Fe are placed at 822.91 ± 7.10 keV and 1200.0 ± 18.2 keV where the plus-minus value indicates one standard deviation. The lower iron line, which is observed to be associated with a nuclear de-excitation that produces a gamma-ray of energy 846.8 keV [3] here on Earth, is expected to be placed at 841.9 keV after factoring in the redshift that will be caused by the relative velocity of NGC4527. This is done using the equation

$$E_{exp} = \frac{E_E}{1+z}, \tag{5.4}$$

where E_{exp} is the expected gamma ray energy, E_E is the observed gamma ray energy here on earth, and z is the redshift of NGC4527 and has value 0.005791 [7]. The upper iron line,

which is related to a 1238.3 keV gamma-ray, is expected to be placed at 1231.2 keV after factoring in the appropriate redshift. It should be noted that the ^{27}Mg line is absent in this best fit. Both iron lines are shifted downward in energy, the first with a 2.7σ significance and the second with a 1.7σ significance. The resulting percentage difference for the first and second excited state energies are

$$\frac{\delta E_1}{E_1} = 0.023 \pm .008, \quad \frac{\delta E_2}{E_2} = 0.025 \pm 0.015, \tag{5.5}$$

given to one standard deviation. The weighted average in the energy percentage difference and the combined standard deviation is found using

$$\frac{\delta E}{E} = \frac{\sum_{\mathrm{i}} (\delta E/E)_{\mathrm{i}} (1/\sigma_{\mathrm{i}})^2}{\sum_{\mathrm{j}} (1/\sigma_{\mathrm{j}})^2}, \quad \frac{1}{\sigma^2} = \sum_{\mathrm{i}} \frac{1}{\sigma_{\mathrm{i}}^2}, \tag{5.6}$$

which result in the values

$$\frac{\delta E}{E} = 0.023 \pm 0.007, \tag{5.7}$$

which is an indication of a 3.2σ result. A collection of these values indicated by the fit is provided in Table 5.1.

Table 5.1. Table of the energies of terrestrial, redshifted, and fitted (with uncertainty) gamma rays from the deexcitations of ^{56}Fe along with the value of the difference between the expected and fitted energies and their significance. Also included are the combined percentage difference in the energies and its significance.

State of ^{56}Fe	E_E (keV)	E_{exp} (keV)	E_{fit}(Uncrty.) (keV)	$\Delta E_{exp,fit}$ (keV)	σ-value
Second Excited State	1238.3	1231.2	1200.0(18.2)	31.2	1.7σ
First Excited State	846.8	841.9	822.91(7.10)	18.99	2.7σ
		$\delta E/E$	Significance		
	Combined	0.023±0.0073	3.2σ		

The implied pion mass variation from this averaged energy deviation, along with Equations (4.34) and (4.44), is

$$\left(\frac{\delta \dot{m}_\pi}{m_\pi}\right)_{rig} = -(2.2 \pm 0.7) \times 10^{-10}\ \mathrm{yr}^{-1}, \quad \left(\frac{\delta \dot{m}_\pi}{m_\pi}\right)_{phon} = -(2.5 \pm 0.8) \times 10^{-10}\ \mathrm{yr}^{-1} \tag{5.8}$$

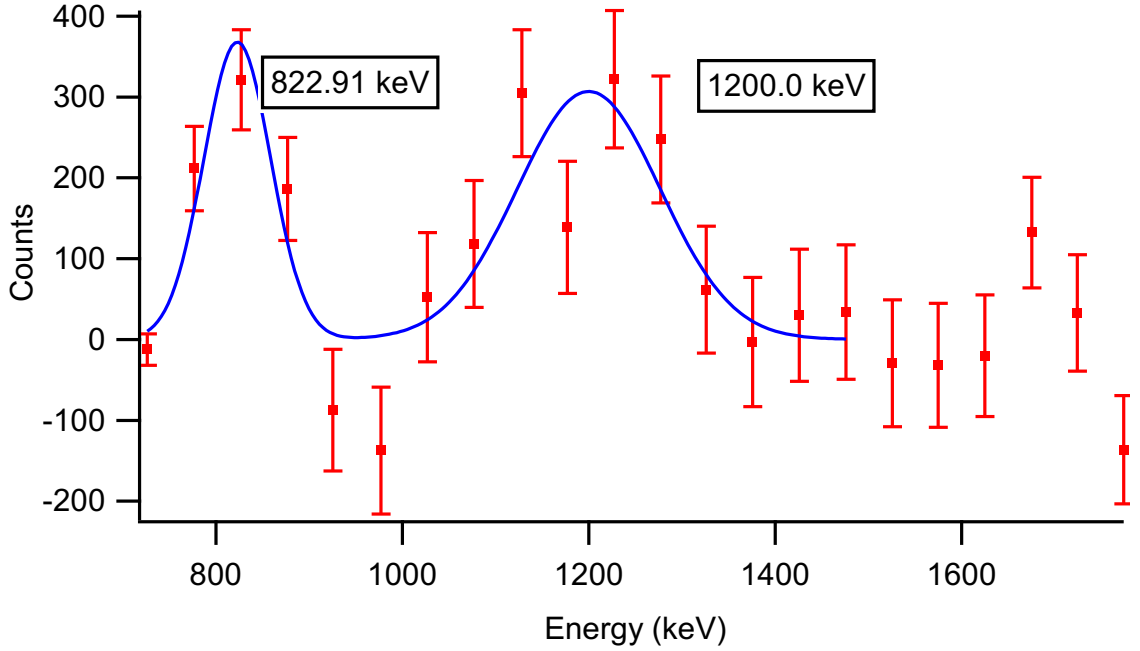

Figure 5.5. Best fit ($\chi^2/DoF \approx 1.42$) of the background subtracted SN 1991T gamma ray data after fixing Gaussian widths and ^{27}Mg decay energy. Negative counts occur when the background counts exceeds that of the collected data. This can occur when the model predicts an excess of counts in a particular energy region and/or the instrument does not register a count for a relevant gamma ray.

for both the rigid rotor and liquid drop models given to one standard deviation. It is reiterated that these values are given only with the fit uncertainty since the theoretical uncertainties are too large and difficult to predict. These values can be compared with the existing limits compiled in Table 5.2.

5.5 Discussion of Fits

The combined spectral data of SN 1991T indicates the decay of ^{56}Co with a significance above 3σ [5]. However, this claim is contested in the literature (see [101] and the references therein). This disagreement arises from the observed gamma rays fluxes being too small relative to the mass of ^{56}Ni SN 1991T is believed to contain based on its luminosity [102], [103]. The small flux of gamma rays cannot be predicted with any known model of Type Ia

supernovae. In contrast to this objection, it should be noted that Reference [5] was produced after the publication of References [102] and [103] to address any systematic errors that would produce a signal that mimics the decay of ^{56}Co. It was concluded by the authors that the 3.3σ signal does not overstate the confidence that there are ^{56}Co decays occurring in SN 1991T suggesting that the objections has been resolved.

The best fits indicate the absence of the ^{27}Mg in the SN 1991T background-subtracted data, both before and after fixing fitting parameters. This is contrary to the explicit inclusion of this line by the authors of [5] despite its weak flux relative to the two iron lines. However, many datasets using COMPTEL were collected, of which one example is provided in [5]. The dataset included is the combined data collected within three degrees of SN 1991T. Due to the authors' certainty of the existence of the ^{27}Mg line and their knowledge of the instrumentation of COMPTEL, it is highly likely that this line was seen in other datasets and not in the one provided in the dataset publication used in this analysis.

The only line within the background data that is not contaminated by other processes is the line produced by the formation of deuterium within the D_1 liquid scintillator. Deuterium is known to form after hydrogen captures a neutron and subsequently emits a gamma-ray of approximately 2223 keV. However, when the background model is fit, the best fits ($\chi^2/DoF \approx 1.35$) place the line associated with deuterium formation at 2229$\pm$1.18 keV. This may be due to a spectral artifact above the deuterium line which deviates from the background function. We have found this artifact can reliably be fit with a Gaussian that is wide relative to the deuterium Gaussian or a function quadratic in the energy, possibly causing the line to shift to marginally higher energies. Various methods were employed to determine if this was the case including finding the residual of the artifact and subtracting it out from the background model or using a different background function to the one provided. Despite the attempts to account for the artifact, the deuterium line was consistently placed approximately 6 keV above its expected position. Assuming to first order the COMPTEL calibration is a linear response function ($E(x) = a+bx$), this 6 keV shift would correspond to either a 6 keV shift if due to an error in the a term calibration or an approximate 3 keV shift at the position of the upper iron-line if due to an error in the b term calibration. Assuming the maximum shift indicated by the deuterium line to higher energies by 6 keV, this implies

that the energy deviation of the upper iron-line would be larger by 20% downwards in energy. In order to present a conservative iron offset, this systematic effect is ignored. Furthermore, this maximum 6 keV shift will be less than 3% of the combined estimated shift of both lines.

At this point it can be shown that the resolution of COMPTEL is not sufficient for the spectral line to attain its true parabolic shape when detected. The arithmetic average of the ratio of the line width (σ) divided by the line energy (E) has the value

$$\frac{\sigma}{E} \approx 0.055, \tag{5.9}$$

implying that any value below this cannot be fully resolved. It is known that the ejecta of SN 1991T initially expands with a speed of $\sim 10,000$ km/s that exponentially decays with time [104]. This speed can be used to predict the maximum value of the ratio of the width to the energy as determined by the velocity of the ejecta. The width of the parabolic peak is taken to be $\sim 20,000/3 \approx 6,500$ km/s and results in the value

$$\frac{\sigma}{E} = \frac{1}{1-z} - \frac{1}{1+z} \approx 0.044. \tag{5.10}$$

This energy width that is determined by the velocity of the ejecta will only decrease with time implying that the true line shape is not resolvable by COMPTEL. Therefore, it is reasonable to expect that the detected lines will be in the shape of a Gaussian.

One may argue that the energy shifts may be caused by an asymmetric shape of the ejecta. However, it has been found that SN 1991T is a marginal case of a spherical explosion [104]. Furthermore, the detonation of a white dwarf, regardless of any initial asymmetry, is expected to create a spherically symmetric distribution of ^{56}Ni after the ejecta is optically thin [105]. Even if these expectations are dismissed, applying the conservation of momentum to an asymmetric radioactive layer will imply that there is a large mass of slow-moving red-shifted radioactive matter and a small mass of fast-moving blue-shifted radioactive matter (for example). The larger blue-shift will balance the larger mass of the red-shifted material and is expected to result in a broadened line at the expected energy. Therefore, the observed

shift to lower energies in SN 1991T is not likely to be caused by an asymmetric shape of the ejecta.

5.6 Comparison of Limit on Pion Mass Variation to Existing Limits Derived from Terrestrial Experiments

The variation of fundamental constants and the resulting effect on the energies and frequencies of nuclear and optical transitions is a topic of intense study. This is due to the fact that deviations in these quantities allows one to put constraints on models of new degrees of freedom such as ultralight dark matter (for an example see reference [8]). It has become a standard to compare these limits, in terms of the quark and pion mass variations, for this reason. This study places a limit on a parameter of dynamical dark energy as a consequence of these mass variations. Therefore, it is instructive to compare this limit, which is generated by astrophysical considerations, with the limits produced by lab-based experiments. This section contains a table of those existing upper limits (Table 5.2) with the source that was used to produce them, as well as the reference from which they are taken. Uncertainties are provided in parentheses when available.

Table 5.2. Theoretical and experimental upper limits on quark and pion mass variations. Values with a * are an average of strange and charm mass variations. The values with a † is the mass variation of the strange quark. The pion mass will not vary in these scenarios since pions are only comprised of first-generation quarks. The variation of the pion mass is not usually reported (except in [12]), but can be found by multiplying the quark mass variation by the appropriate sensitivity coefficient ($K_{\pi,q} = 0.498$).

Source	$\|\delta\dot{m}_q/m_q\|$ (yr^{-1})	$\|\delta\dot{m}_\pi/m_\pi\|$ (yr^{-1})	Reference
Yb^+ transition frequency	$0.83(1.25)\times10^{-15}$	$0.21(0.31)\times10^{-15}$	[12]
Oklo	2.2×10^{-18}	1.1×10^{-18}	[13]
Oklo	$3.8\times10^{-19*}$	N/A	[106]
Ratio of p and e^- mass	$6.6\times10^{-16*}$	N/A	[106]
Nuclear magnetic moments	$9.8\times10^{-15\dagger}$	N/A	[106]
Throium nuclear clock	$1.5\times10^{-22*}$	N/A	[106]
Rb transition frequency drift	$0.3(2.5)\times10^{-14}$	1.5×10^{-15}	[107]
Global fit to transition frequency ratios	$7.1(4.4)\times10^{-15}$	3.1×10^{-15}	[75]

5.6.1 Differences Between This Analysis and Terrestrial Analyses

As can be seen from Table 5.2, the best experimental limits on the quark mass variation and the resulting pion mass variation are obtained from the Oklo natural nuclear reactor. This is because Oklo was active 1.8 billion years ago. Since this work will utilize light that is 44 million years old, limits as low as 10^{-18} yr^{-1} will not be derived for the quark mass variation as indicated by deviations in the energies of nuclear gamma rays. In fact, the limits derived are

$$\left(\frac{\delta\dot{m}_\pi}{m_\pi}\right)_{rig} = -(2.2 \pm 0.7) \times 10^{-10}\ \text{yr}^{-1}, \quad \left(\frac{\delta\dot{m}_\pi}{m_\pi}\right)_{phon} = -(2.5 \pm 0.8) \times 10^{-10}\ \text{yr}^{-1}, \quad (5.11)$$

which are both eight orders of magnitude larger than the Oklo limits and at least four orders of magnitude larger than other experimental limits. However, there are key differences between this work and Oklo studies that make this analysis worthwhile despite the large difference in 'look-back' time. There also exist differences between this work and the other experiments/analyses in the table that can be commented on.

The first and most obvious difference with Oklo is that an extragalactic source is utilized for this work. Oklo is a terrestrial nuclear reactor that will be subject to the same ambient conditions as any experiment conducted on or near the earth. Any effect observed using Oklo cannot be used to indicate differences in the local dark matter and/or dark energy densities and any inhomogeneities that exist across intergalactic distances. These inhomogeneities can be caused by the local mass content warping spacetime, which can vary at different regions in space depending on the amount of mass present. For dark matter, an example of these inhomogeneities are dark matter haloes [108]. An analogous case for dark energy is presented in References [109], [110]. Although not performed here, this work provides an avenue for using energy deviations to inform the interactions of photons as they travel to us from distant supernovae.

The second difference is that Oklo studies and this work use different processes to place limits. The limit produced from the Oklo reactor is based on the disappearance of certain isotopes, mainly Samarium-149 ($Z = 62$), which contain a neutron resonance close to zero

and can be understood with single-particle scattering models [90]. This work compares astrophysical gamma rays arising from collective models of nuclear deexcitations to their terrestrial counterparts using spectroscopic data to generate an average energy deviation over some time interval. This approach requires a new framework to be developed that is different from the framework used for the Oklo reactor.

The third difference is the type of nucleus utilized for this work. Samarium is a heavy nucleus with a complex structure. This work uses an intermediate-mass isotope, ^{56}Fe, which is the most abundant isotope of iron. The less complicated nature of the ^{56}Fe nucleus reduces the opportunity for the introduction of experimental and theoretical uncertainties. An added benefit is that ^{56}Fe is known to be synthesized naturally in Type Ia supernovae, of which the capabilities of observing are currently experiencing an increase in quantity and quality.

This work is distinct when compared to the limits obtained from the variation of atomic transitions frequencies. Included in these experiments are the Yb+ and Rb atoms, whereas the global fit includes the results of Hg+, Sr, and Al+ atoms among others [75]. These limits are derived by using the experimental results of the drift of electronic oscillations to a fiducial atom, which, in most cases, is the Cs atom [12]. The electronic transition frequency drift can be related to a variation in the nuclear radius and is derived in other works [12], [83], [111]. Subsequently, it is then determined what the maximum dark matter energy density can be to produce this quark mass variation. However, this work considers the energies produced by nuclear processes, in contrast to atomic processes, and their dependence on the nuclear radius to intermediately determine the limit on a possible quark and pion mass variation. The ultimate goal of this work is to determine the configuration of a dark energy field, instead of a dark matter field, that would produce the pion mass variation required by any observed energy deviation. A summary of these various differences is provided in Table 5.3.

Table 5.3. Collection of differences between analyses of the Oklo natural nuclear reactor and this work which studies a Type Ia supernova through its spectroscopic data.

System		This Work
Oklo	Same Galaxy	Different Galaxy
	^{149}Sm	^{56}Fe
	Single Particle Quantum States	Collective Quantum States
	Parity-Odd Fermion State (7/2−)	Parity-Even Boson States (4+, 2+, 0+)
	1.8×10^9 years ago	44×10^6 years ago
	Goal is quark mass variation	Goal is implied configuration of Q
	Subsequent analyses for Dark Matter	Analysis for Dark Energy
Atomic Transition Frequency Experiments	Atomic Processes	Nuclear Processes
	Terrestrial	Extragalactic
	Goal is quark mass variation	Goal is implied configuration of Q
	Subsequent analyses for Dark Matter	Analysis for Dark Energy

5.7 Resulting Upper Limit on $\dot{Q}$

Representative values of the upper limit for different values of the decay constant coefficient (α) and the tracker potential power (p) are provided in Tables C.1 and C.2 of Appendix C for the deformed rigid rotor and the vibrating liquid drop, respectively. These values are calculated after plugging Equations (4.52) and (4.53) into both Equation (4.38) and Equation (4.45). This yields the two equations

$$\dot{Q}_{rig}(\alpha, p) = \frac{\alpha^2 M_{pl}}{0.24\sqrt{8\pi}\Delta t} (3\Omega_\Lambda)^{1/p} \frac{\delta E}{E}, \tag{5.12}$$

$$\dot{Q}_{phon}(\alpha, p) = \frac{\alpha^2 M_{pl}}{0.12\sqrt{8\pi}\Delta t} (3\Omega_\Lambda)^{1/p} \left(\frac{1-\xi}{1-3\xi/2}\right) \frac{\delta E}{E}, \tag{5.13}$$

where $M_{pl} = 1.22 \times 10^{19}$ GeV, $\Delta t = 44 \times 10^6$ yrs, $\Omega_\Lambda = 0.685$, $\xi = 2.94$, and $\delta E/E = 0.023$. The `MATLAB` code for calculating these values, as well as generating the allowed parameter spaces seen in the next section, is available in Appendix D.

There are two characteristics of these values that should be taken into account. The first of these characteristics is that all values of $\dot{Q}\Delta t$ are small relative to Q_Λ. For reference, Q_Λ takes its smallest value when $p = 1$ which results in the value

$$Q_\Lambda(p=1) = \frac{M_{pl}}{\sqrt{8\pi}} \frac{1}{(3\Omega_\Lambda)} \approx 1.2 \times 10^{18} \text{ GeV}. \tag{5.14}$$

The largest value of $\dot{Q}\Delta t$ for $p = 1$ is obtained when $\alpha = 0.1$ for both models and has values

$$\dot{Q}_{rig}(p=1, \alpha=0.1)\Delta t = (4.7 \pm 1.5) \times 10^{15} \text{ GeV}, \tag{5.15}$$

$$\dot{Q}_{phon}(p=1, \alpha=0.1)\Delta t = (5.4 \pm 1.7) \times 10^{15} \text{ GeV}, \tag{5.16}$$

implying the quintessence-like field behaves roughly as a cosmological constant. This is expected because of the approximation

$$\rho_Q \approx V(Q_\Lambda), \tag{5.17}$$

made throughout this analysis. The second notable characteristic is that the values of $\dot{Q}_{phon}$ are 12% higher than $\dot{Q}_{rig}$ for a given value of α and p. This is also expected because the ratio of Equation (4.38) to (4.45)

$$\frac{\dot{Q}_{rig}}{\dot{Q}_{phon}} = \frac{1}{2}\frac{(1-3\xi/2)}{(1-\xi)} \approx 0.88, \tag{5.18}$$

where ξ is approximately 2.94 for the ^{56}Fe nucleus.

It is not conventional to place limits on the field itself, but on the observable quantities that the field will produce. These values are the fractional dark energy density Ω_Λ, the fractional matter energy density $\Omega_m \approx 1 - \Omega_\Lambda$ (assuming the current energy density of radiation is negligible), and the dark energy equation of state parameter w_Q. A recent and extensive review of the observational constraints on these quantities is available in [112]. This review compiles results for quintessence and quintessence-like models with various potentials, focusing on the original tracker potential of Ratra and Peebles due to its simplicity. A summary of the derived constraints is that none of the recent measurements of the observed quantities definitively rules out the possibility of dynamical dark energy, including dark energy as a scalar field with a potential of the form given in Equation (3.14), for different values of the tracking potential power (here referred to as p) [112], [113]. Noting that the pseudoscalar nature of the field will not affect the value of these quantities (but the fundamental interactions it has), the values provided in Tables C.1 and C.2 are considered workable since recent values were used for the observational quantities. This will become more apparent in the next section where the combined and non-combined DESI data [65]–[68] was used to generate allowed parameter spaces.

These upper limits, which are crucial for determining the current configuration of the quintessence-like field Q today, can act as a 'bridge' to help inform the fundamental micro-physical nature of dark energy. This can be achieved by factoring in the interactions this field would have with experiments that are conducted here on earth. Assuming that the field is of a pseudoscalar nature provides a starting point of what kind of interactions and effects to look for, while the limits in the tables above will determine the maximum magnitude of those interactions. The systems that would most immediately assist in the achievement of

this goal are those that contain anomalies and tensions. A few famous examples are the magnetic moment of the muon, neutrino oscillations, and non-zero neutrino masses.

There exists a discrepancy between the theoretical prediction and experimental measurement of the muon magnetic moment. This disagreement, which has been known of for about fifteen years, is a 3σ-4σ deviation [114]. This discrepancy has become known as the Anomalous Magnetic Moment of the Muon. Since the method of determining the magnetic moment of the electron, theoretically and experimentally, produces such a good agreement between the two (0.1% deviation [115]), why does the same method produce such a large disagreement for the muon? It is possible, and even likely, that the disagreement comes from systematics and incomplete theory. However, factoring in the effects the field Q would have on the muon magnetic moment would either support or vitiate its existence and further indicate if dark energy does, in reality, exist in this dynamical pseudoscalar form. The limits derived above allow for the quantification of any as of yet unaccounted effect.

After the discovery of the neutrino, it was determined that the neutrino should be massless as indicated by standard model symmetries [116]. However, it is strongly implied, from the excesses and deficiencies in the fluxes of neutrinos of a certain flavor (electron, muon, tau), that neutrinos oscillate as they propagate to detectors from their source [117]. This fact necessitates the existence of a neutrino mass since it would require flavor states to be a superposition of mass states [116], [117]. In fact, the kinematics of beta-decays imply the mass of the neutrino to be very small compared to other standard model masses [117], [118]. This observation is in direct contrast with a prediction from the standard model. Does the field Q and any interactions it has with neutrinos contribute to their small masses and oscillations? Studying this question provides an avenue to a greater understanding of both neutrinos and dark energy, which requires the configuration of the field to be known so that the magnitude of a pseudoscalar effect can be predicted. Furthermore, the recent measurement of a negative value for $m^2_{\nu_e}$ as indicated by the KATRIN data (see [119]) presents another opportunity for determining the configuration of the field and comparing it to the results found here. This is due to the fact that a dark energy field shifting the energy levels within the nucleus can, in principle, shift the beta-decay endpoint energy from which the value of the neutrino mass-squared is determined.

5.8 Allowed Parameter Space

In this section the allowed parameter spaces for the decay constant coefficient α and tracking potential power p are derived. These parameter spaces are produced for the nucleus as a rigid rotor and a vibrating liquid drop. There were three main requirements, represented by the three different plots for each model in Figures 5.6 and 5.7, for a region not to be excluded in the parameter spaces. The first was that the fractional kinetic energy density could not be more than ten percent of the total dark energy density indicated by observation. This was an arbitrary constraint to remain consistent with the approximation

$$\rho_Q \approx V(Q_\Lambda), \tag{5.19}$$

assumed throughout this work. This constraint was ensured by finding the maximum value of α for each model using the equations

$$\alpha_{max,rig} = \frac{\sqrt{8\pi}}{M_{pl}} \left(\frac{\Omega_\Lambda \rho_{crit}}{5} \right)^{1/4} \sqrt{\frac{0.24 Q_\Lambda \Delta t}{\delta E/E}}, \tag{5.20}$$

$$\alpha_{max,phon} = \frac{\sqrt{8\pi}}{M_{pl}} \left(\frac{\Omega_\Lambda \rho_{crit}}{5} \right)^{1/4} \sqrt{\frac{0.12 Q_\Lambda \Delta t}{\delta E/E} \frac{(1-3\xi/2)}{(1-\xi)}}, \tag{5.21}$$

which are derived from the relation

$$\frac{\dot{Q}^2_{rig,phon}}{2\rho_{crit}} \leq \frac{\Omega_\Lambda}{10}, \tag{5.22}$$

where ρ_{crit} is the critical energy density and has value 4.76×10^{-6} GeV/cm^3. The second constraint that was enforced was that the maximum value of the fractional kinetic energy density cannot produce a dark energy equation of state that exceeded the max value indicated by DESI observations ($w_{Q,max} = -0.84$) [65]. The third constraint is similar to the previous one, where DESI observations are complemented with observations of the CMB

and supernovae by the Planck collaboration. This indicates a maximum equation of state of -0.972 [65]. These last two constraints are ensured by using the equation

$$\Omega_{KE,max} = -\frac{(w_{Q,max}+1)}{(w_{Q,max}-1)}\Omega_{\Lambda}, \tag{5.23}$$

which is derived from

$$w_Q \approx \frac{\Omega_{KE}-\Omega_{\Lambda}}{\Omega_{KE}+\Omega_{\Lambda}}. \tag{5.24}$$

The parameter spaces produced exhibit notable behaviors. The first of these is that for values of $\alpha \geq 0.08$, the values of Ω_{KE} (and, by association, $\dot{Q}$) change rapidly. This can be seen by the thin areas of a single color as one travels along the vertical axis for a given value of p. This is in contrast to values of α below 0.08 where the color gradient is more smooth.

A second notable characteristic of these plots is that the curves become horizontal at higher values of p. This implies that the predictions of quintessence models for the kinetic energy density of the field will not differ greatly for different values of p around 10 (and beyond) and a given value of α. This may be more generally true not only for the kinetic energy density, but other quantities as well. However, for $p \leq 3$, models with different powers in the potential will make significantly different predictions for the values of $\dot{Q}$, Ω_{KE}, and w_{DE} for a given value of α. Once again, this may be more generally true for quantities other than these.

Since the values of $\dot{Q}_{phon}$ are higher by about 12% than $\dot{Q}_{rig}$ for a given value of α and p, a smaller parameter space is allowed when modeling the nucleus as a drop of vibrating liquid. However, this difference is small, and there is a large overlap between the parameter spaces of the same constraint for the rigid rotor and the vibrating liquid drop. In the same vein, for a given model, there is a large overlap between the spaces for the permissive constraint that $w_Q \leq -0.84$ and $\Omega_{KE} \leq 0.10\Omega_{\Lambda}$. Using the far more restrictive constraint that $w_Q \leq -0.972$ reduces the allowed parameter space by approximately half.

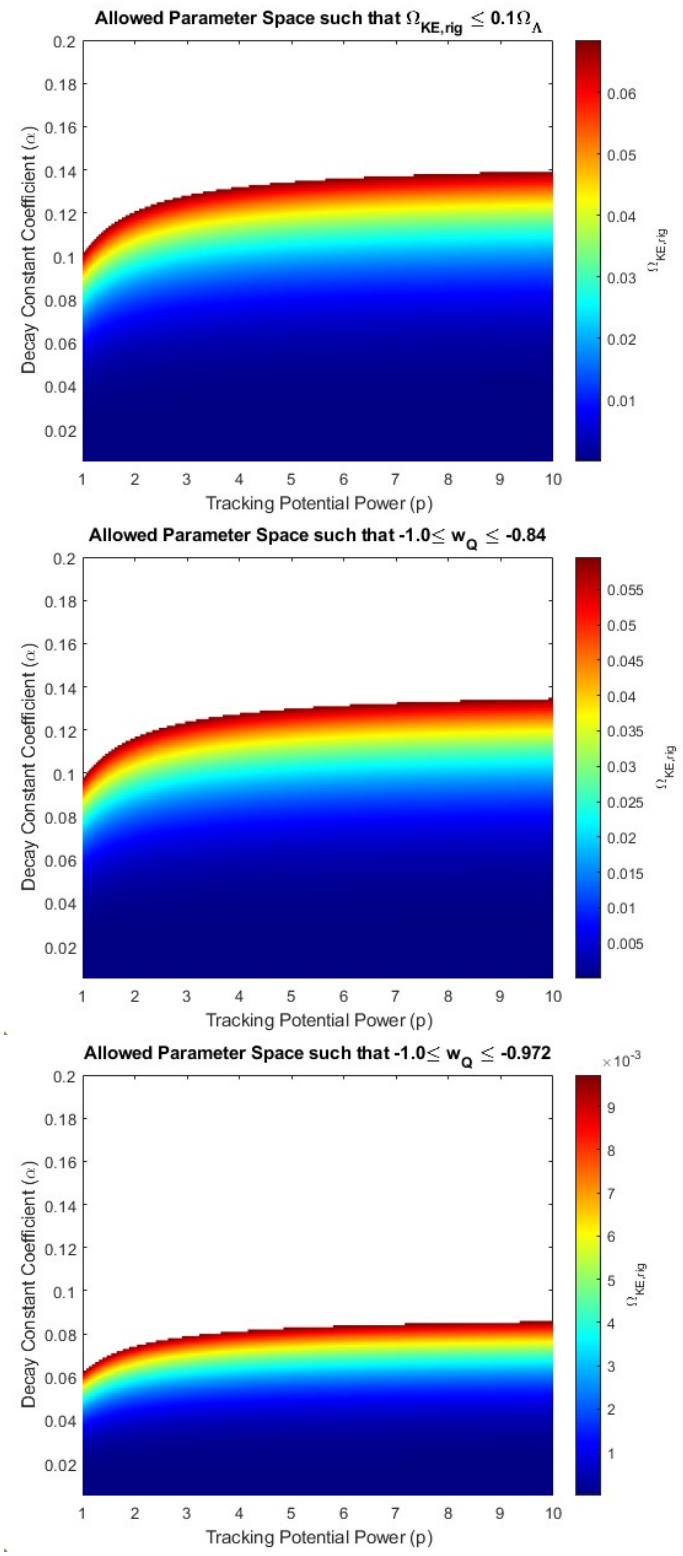

Figure 5.6. Allowed parameter spaces for the nucleus modeled as a rigid rotor along with the value of the fractional kinetic energy density. All constraints used to produce the plots are given in the titles.

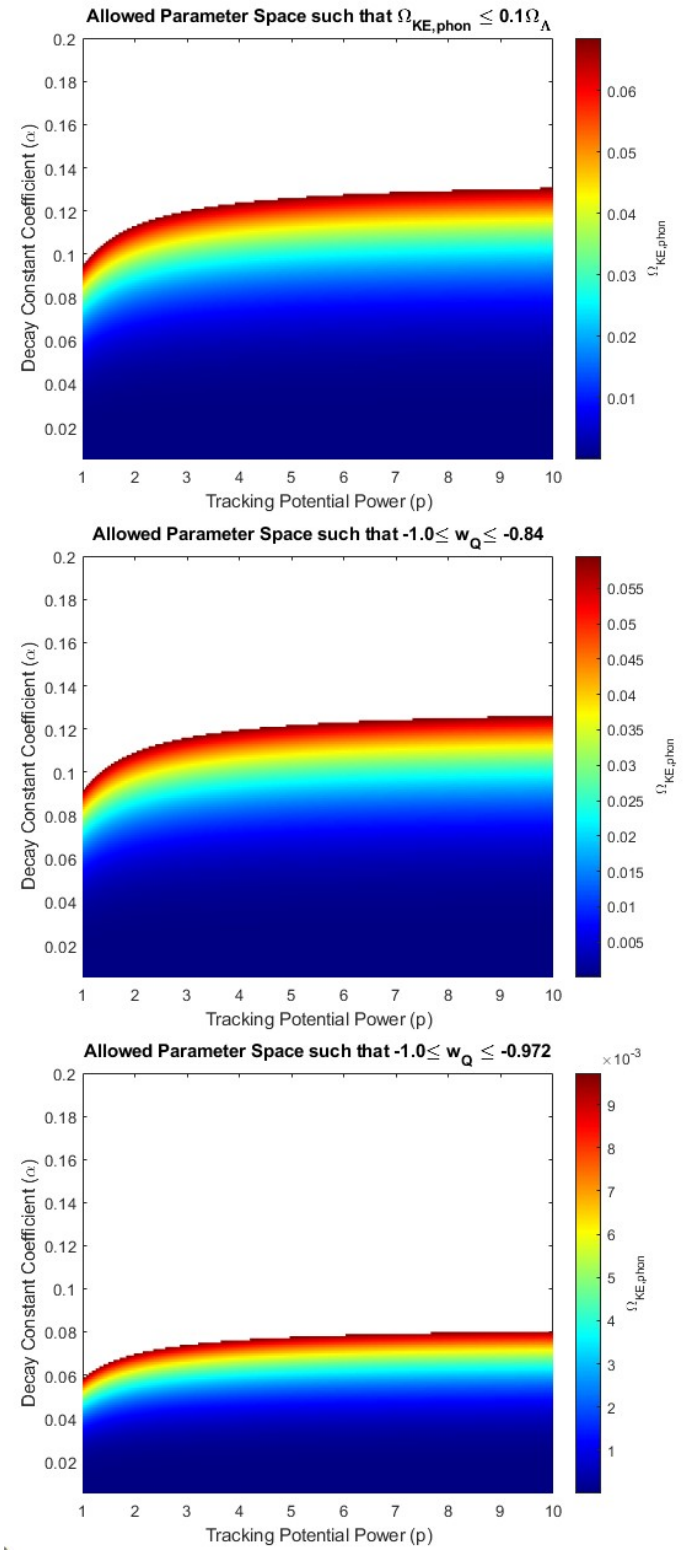

Figure 5.7. Allowed parameter spaces for the nucleus modeled as a vibrating liquid drop along with the value of the fractional kinetic energy density. All constraints used to produce the plots are given in the titles.

It is easy to disregard the importance of the parameters α and p, which is caused by the approximation that $\dot{Q}$ is constant. However, these two parameters have profound implications for the evolution of Q over the course of cosmic history. Therefore, a discussion of the effects α and p, as well as how values for these parameters can be excluded, will be given here.

Operating under a dynamical view of dark energy, a non-vanishing vacuum energy can be produced by a field that is not at the true minimum of its potential due to its flatness [120]. This behavior is sometimes referred to as slow-roll (see Figure 5.8 for a visual representation) In order for the non-vanishing vacuum energy to produce the observed cosmic acceleration, the effective mass of the field must be [120]

$$m_Q \leq H_0 \approx 10^{-33} \text{ eV}. \tag{5.25}$$

The parameter α, as mentioned previously, will determine the effective mass of the field Q. The choice that the field decay constant is $f_Q = \alpha M_{pl}$ results in an effective mass that is approximately 10^{-33} eV when α is of the order of 0.1 [15]. Therefore, values of the mass (and, by association, α) that are above this value result in a cosmic acceleration that is too fast and creates a scenario that is inconsistent with observation.

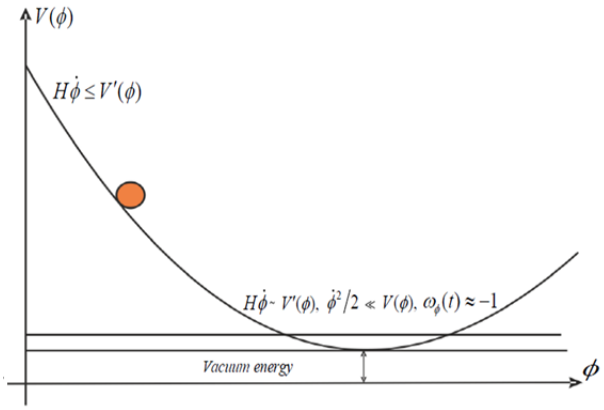

Figure 5.8. Visual representation of a dynamical field (ϕ denoted by the orange ball) 'rolling' down its potential $V(\phi)$. Slow-roll would occur when the field gets very close to the minimum, but does not yet reach it. This behavior is more long term for potentials that are very flat. Diagram is taken from [112].

The power of the tracker potential p will determine if a tracker solution exists and will determine the evolution of Q and the associated quantities Ω_Λ, Ω_m, and w_Q for time scales where the field is not constant. The existence of a tracker solution is determined by the quantity [121]

$$\Gamma \equiv \frac{V''(Q)V(Q)}{V'(Q)^2}, \tag{5.26}$$

where a prime denotes a derivative with respect to Q. If $\Gamma > 1$, the equation of state evolves towards a fixed value independent of initial conditions. For the inverse power law tracker potential of Ratra and Peebles, this quantity has the value [121]

$$\Gamma = 1 + \frac{1}{p}, \tag{5.27}$$

implying that the aforementioned tracking behavior is ensured for $p > 0$. The behavior of the energy density and the equation of state of dark energy for different values of the power (referred to as n) are given in Figure 5.9. It is clear from this figure that the power p will determine, in addition to its evolution, the value of the present-day equation of state, which provides an opportunity to exclude values of p that are not consistent with observation. Furthermore, the power p determines the evolution of the dark energy density and if there exists a time in cosmic history that it overtakes the energy densities of matter and radiation. Values of p that result in dark energy overtaking matter and radiation too early in cosmic history, or not at all, can be excluded.

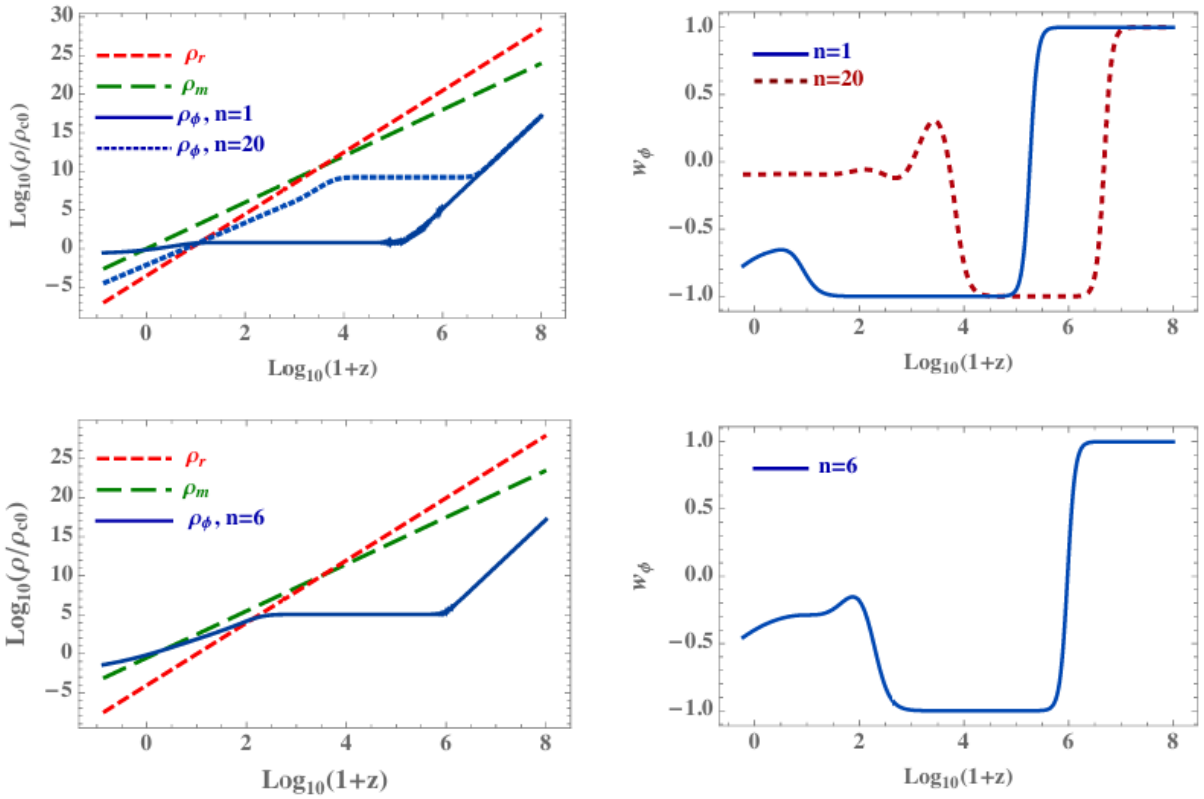

Figure 5.9. Evolution of the dark energy, matter, and radiation energy densities (left) and the dark energy equation of state (right) for the inverse power law potential (n here) versus redshift. The choice of n will determine the evolution of both of these quantities as can be seen from the shapes of the curves. More observationally relevant is the fact that different values of n predict a different dark energy equation of state and different times in cosmic history for when the dark energy density overtakes the energy density of matter and radiation. These plots are taken from [121].

6. FUTURE WORK

There exist many avenues by which to extend this work. The most obvious and most pressing extension is to study other Type Ia supernovae. One specific supernova was chosen for this analysis so that the details and nuances of relating potential gamma ray energy deviations to a quintessence field could be explored. Now that this framework exists, it is imperative to produce limits on $\dot{Q}$ from other supernovae to compare them to each other. There are two interesting determinations that can be made from this line of inquiry. The first is determining how the limits change as a function of distance. If a Type Ia supernova is twice as close to the earth as SN 1991T, are the limits increased/decreased by a factor of two? Is the relation linear or quadratic? Related to this is determining how the limit on the pion mass variation changes as a function of distance. Since the pion mass is approximately the same as $\frac{1}{\Delta t}\frac{\delta E}{E}$, there is the possibility that the limit ($\approx 10^{-10}$ yr^{-1}) will not improve. This is because a gamma ray traveling to earth from a supernova that is closer will take less time to arrive. However, it is possible that the percentage difference in the expected and measured energies of the gamma ray is smaller. It would be instructive to determine if this is the case or if there is any change in this value.

Additionally, this work can be extended to other stellar events as long as they generate a gamma ray spectrum via nuclear deexcitations. The most immediate stellar events that can be included are Type II supernovae, since they too contain ^{56}Co decaying into ^{56}Fe. However, it would be desirable to include stellar events that contain a different nucleus emitting gamma rays. This would permit the comparison of the upper limit on $\dot{Q}$ between different nuclei belonging to astrophysical objects at roughly the same distance. The dependence of $\dot{Q}$ on the atomic number Z and the mass number A could then be determined.

Furthermore, there are many variations that can be made to the quintessence model for further studies. An approximation made in this work is that $\dot{Q}$ was constant, which makes this work applicable only for time intervals small relative to the age of the universe. Higher-order expansions of the quintessence field would permit the determination of how $\dot{Q}$ changes as the universe evolves. This, in turn, makes the expansion valid for earlier epochs in cosmic history and permits one to study more ancient phenomena.

The potential chosen for this work was a generalized tracking potential of the form

$$V(Q) = \frac{M^{4+p}}{Q^p}. \tag{6.1}$$

However, there exists a generalized potential that includes a larger class of quintessence models which has the form [113]

$$V(Q) = \frac{M^{4+p}}{Q^p} \mathrm{e}^{\frac{1}{2}(\kappa Q)^n}, \tag{6.2}$$

where $\kappa \equiv \sqrt{8\pi G}$ and n is some power. Included above are tracking potentials ($n = 0$) and supergravity ($n = 2$).

A quintessence model was chosen for this analysis since it is the simplest extension to the cosmological constant. There do exist more complex models of dark energy that include the behaviors that are associated with quintessence fields. An example of this are K-essence models. To further relax the fine-tuning associated with quintessence models that come from the definition of a potential and the determination of its free parameters, K-essence models are defined by the inclusion of a non-canonical kinetic energy term into its Lagrangian. This term becomes the source of universal accelerated expansion (see [122]–[125]). A generalized form of this kinetic energy term is given by [125]

$$\mathcal{L}_K = K(Q)\tilde{p}(X), \tag{6.3}$$

where $K(Q) > 0$ and $X \equiv \frac{1}{2}\partial_\mu Q \partial^\mu Q$.

Similar to quintessence models are phantom dark energy models. These models replace the quintessence field Q with a phantom field ϕ and a positive kinetic energy term with a negative kinetic energy term in the Lagrangian [126]

$$\mathcal{L}_{phan} = -\frac{1}{2} g^{\mu\nu} \partial_\mu \phi \partial_\nu \phi - V(\phi). \tag{6.4}$$

The main feature of phantom dark energy models is that a dark energy equation of state less than -1.0 can be produced, which is a value that is allowed by most datasets.

Quintom dark energy is a model where both a quintessence field and phantom field is posited that obey the Lagrangian [127]

$$\mathcal{L}_{Quint} = \frac{1}{2} g^{\mu\nu} \partial_\mu Q \partial_\nu Q - \frac{1}{2} g^{\mu\nu} \partial_\mu \phi \partial_\nu \phi - V(Q, \phi). \tag{6.5}$$

These models allow for a dark energy equation of state less than -1.0 in addition to an equation of state greater than -1.0. It is evident that there is no shortage of dark energy models that can be used to place a limit on $\dot{Q}$ (in addition to $\dot{\phi}$ for the appropriate models). All these limits can be compared to one another while also determining model-dependent behavior of $\dot{Q}$ or $\dot{\phi}$. The framework developed here would have to be extended to quintom models since these posit two dark energy fields.

7. SUMMARY

The framework for relating astrophysical gamma ray energy deviations to a pseudoscalar quintessence field using an observed 3.2σ effect has been developed here. The existence of this quintessence field is posited because of the inconsistencies and theoretical issues that go undressed with dark energy in the form of a cosmological constant. The pseudoscalar nature of this field is suggested by the anomalous measurement of cosmic birefringence. A tantalizing microphysical object to associate with this pseudoscalar field are ultralight ALPs because of their simplicity, their suggested existence across many subfields of physics, and the observational signatures they would reproduce.

This work is based on the possible variations of the pion and quark masses that would result from the coupling of the pseudoscalar field to nucleons, which fits into the study of the variation of fundamentals constants more generally. To unambiguously relate the quintessence field to the gamma ray energy deviations surmised from the spectroscopic data of SN 1991T, a nuclear model must be chosen. The two models chosen for this purpose are the nucleus as a rigid rotor and a vibrating liquid drop. In order for a limit to be derived for the time-varying component of the quintessence field using these models, the lowest order of the field and the decay constant of the field must be chosen. The former can be calculated by assuming that most of the energy density of dark energy today is generated by the field's potential, which makes this work consistent with observation. The decay constant was chosen to be proportional to the Planck mass. This choice is common among ALP dark energy models since this is the scale with which new physics is associated.

The analysis of the SN 1991T data indicates an energy deviation of approximately 2.3%, which is the averaged shift of the first and second excited states of ^{56}Fe. This deviation corresponds to a 3.2σ effect. The resulting upper limit on $\dot{Q}$ is at least 11 orders of magnitude smaller than the constant term of the field Q_Λ. There exists an allowed parameter space for the free parameters α and p as indicated by the fractional kinetic energy density Ω_{KE} and the dark energy equation of state w_Q. This parameter space is large when using only the observations of DESI, but is drastically reduced by complementing DESI observations with Planck observations of the cosmic microwave background and supernovae. The upper

limits on $\dot{Q}$ correspond to a pion mass variation of approximately 10^{-10} yr^{-1}. This limit is eight orders of magnitude higher than the best limits placed using the Oklo natural nuclear reactor. However, there are distinct differences in this work, as well as future opportunities for analyses of this type not available to Oklo, that make this work complementary to the studies Oklo, rather than eclipsed by them. The main results of this study are contained in Table 7.1

There exist many opportunities to expand this work. The most pressing and immediate of these is to extend this analysis to other Type Ia supernovae. However, this work can include other astrophysical events as long as a gamma ray spectrum generated by nuclear deexcitations is available. The inclusion of other astrophysical objects allows for nuclei different from ^{56}Fe to be used for placing a limit on $\dot{Q}$. Additionally, different models of dark energy can be used to generate a limit. These dark energy models include K-essence, phantom dark energy, and quintom dark energy, to name a few.

Table 7.1. Result for energy deviation indicated by the detected gamma rays of SN 1991T, energy shift per year, pion mass variation per year for the rigid rotor & phonon models, and max values of the time-varying part of the quintessence field for the rigid rotor & phonon models. Uncertainties are given at one standard deviation.

Quantity	**Result**
$\delta E/E$	0.023 ± 0.0073
$\delta \dot{E}/E$	$(5.2 \pm 1.7) \times 10^{-10}$ yr^{-1}
$(\delta \dot{m}_\pi/m_\pi)_{rig}$	$-(2.2 \pm 0.69) \times 10^{-10}$ yr^{-1}
$(\delta \dot{m}_\pi/m_\pi)_{phon}$	$-(2.5 \pm 0.79) \times 10^{-10}$ yr^{-1}
$\dot{Q}_{max,\mathrm{rig}}$	$(1.07 \pm 0.35) \times 10^{8}$ GeV/yr
$\dot{Q}_{max,phon}$	$(1.22 \pm 0.39) \times 10^{8}$ GeV/yr

REFERENCES

[1] B. P. Schmidt, R. P. Kirshner, B. Leibundgut, *et al.*, "Sn 1991t: Reflections of past glory," *The Astrophysical Journal*, vol. 434, p. L19, Oct. 1994, ISSN: 1538-4357. DOI: 10.1086/187562. [Online]. Available: http://dx.doi.org/10.1086/187562.

[2] B. Leibundgut, "Type ia supernovae," *Astronomy and Astrophysics Review*, vol. 10, no. 3, pp. 179–209, Sep. 2000, ISSN: 1432-0754. DOI: 10.1007/s001590000009. [Online]. Available: http://dx.doi.org/10.1007/s001590000009.

[3] R. R. K. et al., *The nudat/pcnudat program for nuclear data*, https://www.nndc.bnl.gov/nudat3/, [Accessed 08-01-2025] Data extracted from the NUDAT database, 1996.

[4] N. Fotiades, R. O. Nelson, and M. Devlin, "First 3^- excited state of ^{56}Fe," *Phys. Rev. C*, vol. 81, p. 037 304, 3 Mar. 2010. DOI: 10.1103/PhysRevC.81.037304. [Online]. Available: https://link.aps.org/doi/10.1103/PhysRevC.81.037304.

[5] D. J. Morris, K. Bennett, H. Bloemen, *et al.*, "Reassessment of the ^{56}Co emission from SN 1991T," in *Proceedings of the Fourth Compton Symposium*, C. D. Dermer, M. S. Strickman, and J. D. Kurfess, Eds., ser. American Institute of Physics Conference Series, vol. 410, AIP, May 1997, pp. 1084–1088. DOI: 10.1063/1.54174.

[6] WaveMetrics, *Igor pro*, version 9.05. [Online]. Available: https://www.wavemetrics.com/.

[7] D. O. Cook, J. M. Mazzarella, G. Helou, *et al.*, *Completeness of the nasa/ipac extragalactic database (ned) – local volume sample*, 2023. arXiv: 2306.06271 [astro-ph.GA]. [Online]. Available: https://arxiv.org/abs/2306.06271.

[8] V. V. Flambaum and I. B. Samsonov, *Fluctuations of atomic energy levels due to axion dark matter*, 2023. arXiv: 2302.11167 [hep-ph]. [Online]. Available: https://arxiv.org/abs/2302.11167.

[9] Y. Minami and E. Komatsu, "New extraction of the cosmic birefringence from the planck 2018 polarization data," *Phys. Rev. Lett.*, vol. 125, p. 221 301, 22 Nov. 2020. DOI: 10.1103/PhysRevLett.125.221301. [Online]. Available: https://link.aps.org/doi/10.1103/PhysRevLett.125.221301.

[10] M. Pospelov, A. Ritz, and C. Skordis, "Pseudoscalar perturbations and polarization of the cosmic microwave background," *Physical Review Letters*, vol. 103, no. 5, Jul. 2009, ISSN: 1079-7114. DOI: 10.1103/physrevlett.103.051302. [Online]. Available: http://dx.doi.org/10.1103/PhysRevLett.103.051302.

[11] L. Ubaldi, "Effects of θ on the deuteron binding energy and the triple-alpha process," *Phys. Rev. D*, vol. 81, p. 025 011, 2 Jan. 2010. DOI: 10.1103/PhysRevD.81.025011. [Online]. Available: https://link.aps.org/doi/10.1103/PhysRevD.81.025011.

[12] V. V. Flambaum and A. J. Mansour, "Variation of the quadrupole hyperfine structure and nuclear radius due to an interaction with scalar and axion dark matter," *Phys. Rev. Lett.*, vol. 131, p. 113 004, 11 Sep. 2023. DOI: 10.1103/PhysRevLett.131.113004. [Online]. Available: https://link.aps.org/doi/10.1103/PhysRevLett.131.113004.

[13] V. V. Flambaum and R. B. Wiringa, "Enhanced effect of quark mass variation in ^{229}Th and limits from oklo data," *Physical Review C*, vol. 79, no. 3, Mar. 2009, ISSN: 1089-490X. DOI: 10.1103/physrevc.79.034302. [Online]. Available: http://dx.doi.org/10.1103/PhysRevC.79.034302.

[14] G. Choi, W. Lin, L. Visinelli, and T. T. Yanagida, "Cosmic birefringence and electroweak axion dark energy," *Physical Review D*, vol. 104, no. 10, Nov. 2021. DOI: 10.1103/physrevd.104.l101302. [Online]. Available: https://doi.org/10.1103%2Fphysrevd.104.l101302.

[15] M. Kamionkowski, J. Pradler, and D. G. E. Walker, "Dark energy from the string axiverse," *Phys. Rev. Lett.*, vol. 113, p. 251 302, 25 Dec. 2014. DOI: 10.1103/PhysRevLett.113.251302. [Online]. Available: https://link.aps.org/doi/10.1103/PhysRevLett.113.251302.

[16] S. Panda, Y. Sumitomo, and S. P. Trivedi, "Axions as quintessence in string theory," *Physical Review D*, vol. 83, no. 8, Apr. 2011, ISSN: 1550-2368. DOI: 10.1103/physrevd.83.083506. [Online]. Available: http://dx.doi.org/10.1103/PhysRevD.83.083506.

[17] A. Deshalit and H. Feshbach, *Theoretical nuclear physics*. New York, NY (USA); John Wiley and Sons Inc., Jan. 1990. [Online]. Available: https://www.osti.gov/biblio/6510983.

[18] D. E. Osterbrock, J. A. Gwinn, and R. S. Brashear, "Edwin hubble and the expanding universe," *Scientific American*, vol. 269, no. 1, pp. 84–89, 1993, ISSN: 00368733, 19467087. [Online]. Available: http://www.jstor.org/stable/24941551.

[19] J. A. Frieman, M. S. Turner, and D. Huterer, "Dark energy and the accelerating universe," *Annual Review of Astronomy and Astrophysics*, vol. 46, no. 1, pp. 385–432, Sep. 2008, ISSN: 1545-4282. DOI: 10.1146/annurev.astro.46.060407.145243. [Online]. Available: http://dx.doi.org/10.1146/annurev.astro.46.060407.145243.

[20] H. K. Jassal, J. S. Bagla, and T. Padmanabhan, "Understanding the origin of cmb constraints on dark energy," *Monthly Notices of the Royal Astronomical Society*, vol. 405, no. 4, pp. 2639–2650, Jul. 2010, ISSN: 0035-8711. DOI: 10.1111/j.1365-2966.2010.16647.x. eprint: https://academic.oup.com/mnras/article-pdf/405/4/2639/18444964/mnras0405-2639.pdf. [Online]. Available: https://doi.org/10.1111/j.1365-2966.2010.16647.x.

[21] J. Zheng, D.-C. Qiang, and Z.-Q. You, *Cosmological constraints on dark energy models using desi bao 2024*, 2024. arXiv: 2412.04830 [astro-ph.CO]. [Online]. Available: https://arxiv.org/abs/2412.04830.

[22] H.-J. He and Z. Zhang, "Direct probe of dark energy through gravitational lensing effect," *Journal of Cosmology and Astroparticle Physics*, vol. 2017, no. 08, p. 036, Aug. 2017. DOI: 10.1088/1475-7516/2017/08/036. [Online]. Available: https://dx.doi.org/10.1088/1475-7516/2017/08/036.

[23] T. P. Sotiriou and V. Faraoni, "$f(R)$ Theories of gravity," *Rev. Mod. Phys.*, vol. 82, pp. 451–497, 1 Mar. 2010. DOI: 10.1103/RevModPhys.82.451. [Online]. Available: https://link.aps.org/doi/10.1103/RevModPhys.82.451.

[24] M. Milgrom, *Mond–a pedagogical review*, 2001. arXiv: astro-ph/0112069 [astro-ph]. [Online]. Available: https://arxiv.org/abs/astro-ph/0112069.

[25] K. Koyama, "Ghosts in the self-accelerating universe," *Classical and Quantum Gravity*, vol. 24, no. 24, R231, Nov. 2007. DOI: 10.1088/0264-9381/24/24/R01. [Online]. Available: https://dx.doi.org/10.1088/0264-9381/24/24/R01.

[26] L. Miao, L. Xiao-Dong, W. Shuang, and W. Yi, "Dark energy," *Communications in Theoretical Physics*, vol. 56, no. 3, p. 525, Sep. 2011. DOI: 10.1088/0253-6102/56/3/24. [Online]. Available: https://dx.doi.org/10.1088/0253-6102/56/3/24.

[27] J. YOO and Y. WATANABE, "Theoretical models of dark energy," *International Journal of Modern Physics D*, vol. 21, no. 12, p. 1 230 002, Nov. 2012, ISSN: 1793-6594. DOI: 10.1142/s0218271812300029. [Online]. Available: http://dx.doi.org/10.1142/S0218271812300029.

[28] S. M. Carroll, "The cosmological constant," *Living Reviews in Relativity*, vol. 4, no. 1, Feb. 2001, ISSN: 1433-8351. DOI: 10.12942/lrr-2001-1. [Online]. Available: http://dx.doi.org/10.12942/lrr-2001-1.

[29] S. Dodelson, E. I. Gates, and M. S. Turner, "Cold dark matter," *Science*, vol. 274, no. 5284, pp. 69–75, 1996. DOI: 10.1126/science.274.5284.69. eprint: https://www.science.org/doi/pdf/10.1126/science.274.5284.69. [Online]. Available: https://www.science.org/doi/abs/10.1126/science.274.5284.69.

[30] L. Perivolaropoulos and F. Skara, "Challenges for Λcdm: An update," *New Astronomy Reviews*, vol. 95, p. 101 659, Dec. 2022, ISSN: 1387-6473. DOI: 10.1016/j.newar.2022.101659. [Online]. Available: http://dx.doi.org/10.1016/j.newar.2022.101659.

[31] H. Fischer, C. Käding, H. Lemmel, S. Sponar, and M. Pitschmann, "Search for dark energy with neutron interferometry," Oct. 2023. arXiv: 2310.18109 [hep-ph].

[32] N. Tamanini, "Dynamics of cosmological scalar fields," *Physical Review D*, vol. 89, no. 8, Apr. 2014. DOI: 10.1103/physrevd.89.083521. [Online]. Available: https://doi.org/10.1103%2Fphysrevd.89.083521.

[33] S. Weinberg, "The cosmological constant problem," *Rev. Mod. Phys.*, vol. 61, pp. 1–23, 1 Jan. 1989. DOI: 10.1103/RevModPhys.61.1. [Online]. Available: https://link.aps.org/doi/10.1103/RevModPhys.61.1.

[34] D. SAPONE, "Dark energy in practice," *International Journal of Modern Physics A*, vol. 25, no. 29, pp. 5253–5331, Nov. 2010, ISSN: 1793-656X. DOI: 10.1142/s0217751x10050743. [Online]. Available: http://dx.doi.org/10.1142/S0217751X10050743.

[35] D. Bettoni and J. Rubio, "Quintessential inflation: A tale of emergent and broken symmetries," *Galaxies*, vol. 10, no. 1, p. 22, Jan. 2022, ISSN: 2075-4434. DOI: 10.3390/galaxies10010022. [Online]. Available: http://dx.doi.org/10.3390/galaxies10010022.

[36] W. L. Freedman, "Measurements of the hubble constant: Tensions in perspective*," *The Astrophysical Journal*, vol. 919, no. 1, p. 16, Sep. 2021, ISSN: 1538-4357. DOI: 10.3847/1538-4357/ac0e95. [Online]. Available: http://dx.doi.org/10.3847/1538-4357/ac0e95.

[37] E. Di Valentino, O. Mena, S. Pan, *et al.*, "In the realm of the hubble tensiona review of solutions*," *Classical and Quantum Gravity*, vol. 38, no. 15, p. 153 001, Jul. 2021, ISSN: 1361-6382. DOI: 10.1088/1361-6382/ac086d. [Online]. Available: http://dx.doi.org/10.1088/1361-6382/ac086d.

[38] L. Yin, J. Kochappan, T. Ghosh, and B.-H. Lee, *Is cosmic birefringence model-dependent?* 2023. arXiv: 2305.07937 [astro-ph.CO].

[39] C. Wetterich, "Quintessence - the Dark Energy in the Universe?", vol. 100, pp. 195–206, Jan. 2002. DOI: 10.1023/A:1015878430289. arXiv: astro-ph/0110211 [astro-ph].

[40] J. MARTIN, "Quintessence: A mini-review," *Modern Physics Letters A*, vol. 23, no. 17n20, pp. 1252–1265, Jun. 2008, ISSN: 1793-6632. DOI: 10.1142/s0217732308027631. [Online]. Available: http://dx.doi.org/10.1142/S0217732308027631.

[41] S. Tsujikawa, "Quintessence: A review," *Classical and Quantum Gravity*, vol. 30, no. 21, p. 214 003, Oct. 2013. DOI: 10.1088/0264-9381/30/21/214003. [Online]. Available: https://dx.doi.org/10.1088/0264-9381/30/21/214003.

[42] Y. Gong, "The general property of dynamical quintessence field," *Physics Letters B*, vol. 731, pp. 342–349, 2014, ISSN: 0370-2693. DOI: https://doi.org/10.1016/j.physletb.2014.03.013. [Online]. Available: https://www.sciencedirect.com/science/article/pii/S0370269314001695.

[43] E. J. COPELAND, M. SAMI, and S. TSUJIKAWA, "Dynamics of dark energy," *International Journal of Modern Physics D*, vol. 15, no. 11, pp. 1753–1935, 2006. DOI: 10.1142/S021827180600942X. eprint: https://doi.org/10.1142/S021827180600942X. [Online]. Available: https://doi.org/10.1142/S021827180600942X.

[44] W. J. Wolf and P. G. Ferreira, "Underdetermination of dark energy," *Phys. Rev. D*, vol. 108, p. 103 519, 10 Nov. 2023. DOI: 10.1103/PhysRevD.108.103519. [Online]. Available: https://link.aps.org/doi/10.1103/PhysRevD.108.103519.

[45] S. Gasparotto and E. I. Sfakianakis, *Cosmic birefringence from the axiverse*, 2023. arXiv: 2306.16355 [astro-ph.CO]. [Online]. Available: https://arxiv.org/abs/2306.16355.

[46] G. Choi, M. Suzuki, and T. T. Yanagida, "Quintessence axion dark energy and a solution to the hubble tension," *Physics Letters B*, vol. 805, p. 135 408, Jun. 2020, ISSN: 0370-2693. DOI: 10.1016/j.physletb.2020.135408. [Online]. Available: http://dx.doi.org/10.1016/j.physletb.2020.135408.

[47] H. Nakatsuka, T. Namikawa, and E. Komatsu, "Is cosmic birefringence due to dark energy or dark matter? a tomographic approach," *Physical Review D*, vol. 105, no. 12, Jun. 2022, ISSN: 2470-0029. DOI: 10.1103/physrevd.105.123509. [Online]. Available: http://dx.doi.org/10.1103/PhysRevD.105.123509.

[48] J.-P. Uzan, *Fundamental constants: From measurement to the universe, a window on gravitation and cosmology*, 2024. arXiv: 2410.07281 [astro-ph.CO]. [Online]. Available: https://arxiv.org/abs/2410.07281.

[49] J. R. Eskilt and E. Komatsu, "Improved constraints on cosmic birefringence from the wmap and planck cosmic microwave background polarization data," *Phys. Rev. D*, vol. 106, p. 063 503, 6 Sep. 2022. DOI: 10.1103/PhysRevD.106.063503. [Online]. Available: https://link.aps.org/doi/10.1103/PhysRevD.106.063503.

[50] P. Montero-Camacho and C. M. Hirata, "Exploring circular polarization in the cmb due to conventional sources of cosmic birefringence," *Journal of Cosmology and Astroparticle Physics*, vol. 2018, no. 08, p. 040, Aug. 2018. DOI: 10.1088/1475-7516/2018/08/040. [Online]. Available: https://dx.doi.org/10.1088/1475-7516/2018/08/040.

[51] P. A. R. Ade, K. Arnold, M. Atlas, *et al.*, "Polarbear constraints on cosmic birefringence and primordial magnetic fields," *Phys. Rev. D*, vol. 92, p. 123 509, 12 Dec. 2015. DOI: 10.1103/PhysRevD.92.123509. [Online]. Available: https://link.aps.org/doi/10.1103/PhysRevD.92.123509.

[52] D. Colladay and V. A. Kostelecký, "Lorentz-violating extension of the standard model," *Physical Review D*, vol. 58, no. 11, Oct. 1998, ISSN: 1089-4918. DOI: 10.1103/physrevd.58.116002. [Online]. Available: http://dx.doi.org/10.1103/PhysRevD.58.116002.

[53] P. Aschieri, B. Juro, P. Schupp, and J. Wess, "Noncommutative guts, standard model and c,p,t," *Nuclear Physics B*, vol. 651, no. 1, pp. 45–70, 2003, ISSN: 0550-3213. DOI: https://doi.org/10.1016/S0550-3213(02)00937-9.

[54] R. Mohammadi, "Evidence for cosmic neutrino background from cmb circular polarization," *The European Physical Journal C*, vol. 74, no. 10, Oct. 2014, ISSN: 1434-6052. DOI: 10.1140/epjc/s10052-014-3102-1. [Online]. Available: http://dx.doi.org/10.1140/epjc/s10052-014-3102-1.

[55] T. Fujita, K. Murai, H. Nakatsuka, and S. Tsujikawa, "Detection of isotropic cosmic birefringence and its implications for axionlike particles including dark energy," *Physical Review D*, vol. 103, no. 4, Feb. 2021, ISSN: 2470-0029. DOI: 10.1103/physrevd.103.043509. [Online]. Available: http://dx.doi.org/10.1103/PhysRevD.103.043509.

[56] J. E. Kim and G. Carosi, "Axions and the strong CP problem," *Rev. Mod. Phys.*, vol. 82, pp. 557–601, 1 Mar. 2010. DOI: 10.1103/RevModPhys.82.557. [Online]. Available: https://link.aps.org/doi/10.1103/RevModPhys.82.557.

[57] G. Raffelt, "Axions," in *Matter in the Universe: Proceedings of an ISSI Workshop 19–23 March 2001, Bern, Switzerland*, P. Jetzer, K. Pretzl, and R. Von Steiger, Eds. Dordrecht: Springer Netherlands, 2002, pp. 153–158, ISBN: 978-94-017-2215-5. DOI: 10.1007/978-94-017-2215-5_13. [Online]. Available: https://doi.org/10.1007/978-94-017-2215-5_13.

[58] B. R. Safdi, *Tasi lectures on the particle physics and astrophysics of dark matter*, 2023. arXiv: 2303.02169 [hep-ph].

[59] M. Kamionkowski, J. Pradler, and D. G. E. Walker, "Dark energy from the string axiverse," *Physical Review Letters*, vol. 113, no. 25, Dec. 2014, ISSN: 1079-7114. DOI: 10.1103/physrevlett.113.251302. [Online]. Available: http://dx.doi.org/10.1103/PhysRevLett.113.251302.

[60] L. McLerran, R. D. Pisarski, and V. Skokov, "Electroweak instantons, axions, and the cosmological constant," *Physics Letters B*, vol. 713, no. 3, pp. 301–303, Jul. 2012, ISSN: 0370-2693. DOI: 10.1016/j.physletb.2012.05.057. [Online]. Available: http://dx.doi.org/10.1016/j.physletb.2012.05.057.

[61] R. D. Peccei, "The strong CP problem and axions," in *Lecture Notes in Physics*, Springer Berlin Heidelberg, 2008, pp. 3–17. DOI: 10.1007/978-3-540-73518-2_1. [Online]. Available: https://doi.org/10.1007%5C%2F978-3-540-73518-2_1.

[62] H.-Y. Cheng, "The strong cp problem revisited," *Physics Reports*, vol. 158, no. 1, pp. 1–89, 1988, ISSN: 0370-1573. DOI: https://doi.org/10.1016/0370-1573(88)90135-4. [Online]. Available: https://www.sciencedirect.com/science/article/pii/0370157388901354.

[63] L. Abbott and P. Sikivie, "A cosmological bound on the invisible axion," *Physics Letters B*, vol. 120, no. 1, pp. 133–136, 1983, ISSN: 0370-2693. DOI: https://doi.org/10.1016/0370-2693(83)90638-X. [Online]. Available: https://www.sciencedirect.com/science/article/pii/037026938390638X.

[64] J. Preskill, M. B. Wise, and F. Wilczek, "Cosmology of the invisible axion," *Physics Letters B*, vol. 120, no. 1, pp. 127–132, 1983, ISSN: 0370-2693. DOI: https://doi.org/10.1016/0370-2693(83)90637-8. [Online]. Available: https://www.sciencedirect.com/science/article/pii/0370269383906378.

[65] H.-J. seo, "Desi 2024 baryon acoustic oscillations and cosmological implications," University Seminar, 2025.

[66] D. Brout, D. Scolnic, B. Popovic, *et al.*, "The pantheon+ analysis: Cosmological constraints," *The Astrophysical Journal*, vol. 938, no. 2, p. 110, Oct. 2022, ISSN: 1538-4357. DOI: 10.3847/1538-4357/ac8e04. [Online]. Available: http://dx.doi.org/10.3847/1538-4357/ac8e04.

[67] D. Collaboration, T. M. C. Abbott, M. Acevedo, *et al.*, *The dark energy survey: Cosmology results with 1500 new high-redshift type ia supernovae using the full 5-year dataset*, 2024. arXiv: 2401.02929 [astro-ph.CO]. [Online]. Available: https://arxiv.org/abs/2401.02929.

[68] D. Rubin, G. Aldering, M. Betoule, *et al.*, *Union through unity: Cosmology with 2,000 sne using a unified bayesian framework*, 2024. arXiv: 2311.12098 [astro-ph.CO]. [Online]. Available: https://arxiv.org/abs/2311.12098.

[69] Planck Collaboration, N. Aghanim, Y. Akrami, *et al.*, "Planck 2018 results. VI. Cosmological parameters,", vol. 641, A6, A6, Sep. 2020. DOI: 10.1051/0004-6361/201833910. arXiv: 1807.06209 [astro-ph.CO].

[70] R. R. Caldwell, "An introduction to quintessence.," *Brazilian Journal of Physics*, vol. 30, no. 2, pp. 215–229, Jun. 2000.

[71] P. J. E. Peebles and B. Ratra, "Cosmology with a Time-Variable Cosmological "Constant",", vol. 325, p. L17, Feb. 1988. DOI: 10.1086/185100.

[72] P. Zyla *et al.*, "Review of Particle Physics," *PTEP*, vol. 2020, no. 8, p. 083C01, 2020, and 2021 update. DOI: 10.1093/ptep/ptaa104.

[73] I. Counts, J. Hur, D. P. L. Aude Craik, *et al.*, "Evidence for nonlinear isotope shift in Yb^+ search for new boson," *Phys. Rev. Lett.*, vol. 125, p. 123 002, 12 Sep. 2020. DOI: 10.1103/PhysRevLett.125.123002. [Online]. Available: https://link.aps.org/doi/10.1103/PhysRevLett.125.123002.

[74] S. O. Allehabi, V. A. Dzuba, V. V. Flambaum, and A. V. Afanasjev, "Nuclear deformation as a source of the nonlinearity of the king plot in the Yb^+ ion," *Phys. Rev. A*, vol. 103, p. L030801, 3 Mar. 2021. DOI: 10.1103/PhysRevA.103.L030801. [Online]. Available: https://link.aps.org/doi/10.1103/PhysRevA.103.L030801.

[75] J. Guéna, M. Abgrall, D. Rovera, *et al.*, "Improved tests of local position invariance using ^{87}Rb and ^{133}Cs fountains," *Phys. Rev. Lett.*, vol. 109, p. 080 801, 8 Aug. 2012. DOI: 10.1103/PhysRevLett.109.080801. [Online]. Available: https://link.aps.org/doi/10.1103/PhysRevLett.109.080801.

[76] A. M. Khokhlov, "Delayed detonation model for type IA supernovae,", vol. 245, no. 1, pp. 114–128, May 1991.

[77] W. Hillebrandt and J. C. Niemeyer, "Type ia supernova explosion models," *Annual Review of Astronomy and Astrophysics*, vol. 38, no. 1, pp. 191–230, Sep. 2000, ISSN: 1545-4282. DOI: 10.1146/annurev.astro.38.1.191. [Online]. Available: http://dx.doi.org/10.1146/annurev.astro.38.1.191.

[78] D. Branch and G. A. Tammann, "Type IA supernovae as standard candles.,", vol. 30, pp. 359–389, Jan. 1992. DOI: 10.1146/annurev.aa.30.090192.002043.

[79] I. of Astrophysics of Andalucia, Aug. 2014. [Online]. Available: https://www.iaa.csic.es/en/noticias/type-ia-supernovae-stem-explosion-white-dwarfs-coupled-twin-stars.

[80] E. Churazov, R. Sunyaev, J. Isern, *et al.*, "Gamma rays from type ia supernova sn 2014j," *The Astrophysical Journal*, vol. 812, no. 1, p. 62, Oct. 2015. DOI: 10.1088/0004-637X/812/1/62. [Online]. Available: https://dx.doi.org/10.1088/0004-637X/812/1/62.

[81] L. A. Kwok, "Exploring the thermonuclear supernova zoo with jwst," University Seminar, 2025.

[82] J. K. Webb, V. V. Flambaum, C. W. Churchill, M. J. Drinkwater, and J. D. Barrow, "Search for time variation of the fine structure constant," *Phys. Rev. Lett.*, vol. 82, pp. 884–887, 5 Feb. 1999. DOI: 10.1103/PhysRevLett.82.884. [Online]. Available: https://link.aps.org/doi/10.1103/PhysRevLett.82.884.

[83] V. V. Flambaum and A. F. Tedesco, "Dependence of nuclear magnetic moments on quark masses and limits on temporal variation of fundamental constants from atomic clock experiments," *Phys. Rev. C*, vol. 73, p. 055 501, 5 May 2006. DOI: 10.1103/PhysRevC.73.055501. [Online]. Available: https://link.aps.org/doi/10.1103/PhysRevC.73.055501.

[84] P. E. Hodgson, E. Gadioli, and E. Gadioli Erba, *Introductory nuclear physics*. Oxford University Press, 1997.

[85] R. K. B. M. A. Preston, *Structure of the Nucleus*. Addison-Wesley Publishing Company, 1982.

[86] B. R. Johnl William Strutt, *The Theory of Sound, Vol. II*. Dover Publications, 1945.

[87] Y. Liu, T. Ye, W. Sun, and H. Guo, "Coupled-channel analysis of deuteron scattering on 56 fe," *EPJ Web of Conferences*, vol. 239, p. 03 018, Jan. 2020. DOI: 10.1051/epjconf/202023903018.

[88] G. M. Temmer and N. P. Heydenburg, "Coulomb excitation of medium-weight nuclei," *Phys. Rev.*, vol. 104, pp. 967–980, 4 Nov. 1956. DOI: 10.1103/PhysRev.104.967. [Online]. Available: https://link.aps.org/doi/10.1103/PhysRev.104.967.

[89] V. V. Flambaum and R. B. Wiringa, "Dependence of nuclear binding on hadronic mass variation," *Phys. Rev. C*, vol. 76, p. 054 002, 5 Nov. 2007. DOI: 10.1103/PhysRevC.76.054002. [Online]. Available: https://link.aps.org/doi/10.1103/PhysRevC.76.054002.

[90] V. F. Dmitriev and V. V. Flambaum, "Limits on cosmological variation of quark masses and strong interaction," *Phys. Rev. D*, vol. 67, p. 063 513, 6 Mar. 2003. DOI: 10.1103/PhysRevD.67.063513. [Online]. Available: https://link.aps.org/doi/10.1103/PhysRevD.67.063513.

[91] A. Banerjee, D. Budker, M. Filzinger, *et al.*, *Oscillating nuclear charge radii as sensors for ultralight dark matter*, 2023. arXiv: 2301.10784 [hep-ph]. [Online]. Available: https://arxiv.org/abs/2301.10784.

[92] Q. Yang and R. Huang, *Search for qcd axions in light of string theory*, 2024. arXiv: 2408.06652 [hep-ph]. [Online]. Available: https://arxiv.org/abs/2408.06652.

[93] L. McLerran, "The electroweak axion, dark energy, inflation and baryonic matter," *Journal of Experimental and Theoretical Physics*, vol. 120, no. 3, pp. 376–379, Mar. 2015, ISSN: 1090-6509. DOI: 10.1134/s1063776115030103. [Online]. Available: http://dx.doi.org/10.1134/S1063776115030103.

[94] A. V. Filippenko, M. W. Richmond, T. Matheson, *et al.*, "The Peculiar Type IA SN 1991T: Detonation of a White Dwarf?", vol. 384, p. L15, Jan. 1992. DOI: 10.1086/186252.

[95] D. O. Jones, S. A. Rodney, A. G. Riess, *et al.*, "The discovery of the most distant known type ia supernova at redshift 1.914," *The Astrophysical Journal*, vol. 768, no. 2, p. 166, Apr. 2013. DOI: 10.1088/0004-637X/768/2/166. [Online]. Available: https://dx.doi.org/10.1088/0004-637X/768/2/166.

[96] V. Schoenfelder, H. Aarts, K. Bennett, *et al.*, "Instrument Description and Performance of the Imaging Gamma-Ray Telescope COMPTEL aboard the Compton Gamma-Ray Observatory,", vol. 86, p. 657, Jun. 1993. DOI: 10.1086/191794.

[97] V. Schönfelder, K. Bennett, J. J. Blom, *et al.*, "The first comptel source catalogue," *Astronomy and Astrophysics Supplement Series*, vol. 143, no. 2, pp. 145–179, Apr. 2000, ISSN: 1286-4846. DOI: 10.1051/aas:2000101. [Online]. Available: http://dx.doi.org/10.1051/aas:2000101.

[98] M. Snelling, K. Bennett, and J. Clear, "A calibration system for space borne medium energy gamma ray telescopes," *Nuclear Instruments and Methods in Physics Research Section A: Accelerators, Spectrometers, Detectors and Associated Equipment*, vol. 248, no. 2, pp. 545–549, 1986, ISSN: 0168-9002. DOI: https://doi.org/10.1016/0168-9002(86)91046-6. [Online]. Available: https://www.sciencedirect.com/science/article/pii/0168900286910466.

[99] G. Knoll, *Radiation Detection and Measurement (4th ed.)* Hoboken, NJ: John Wiley, 2010, ISBN: 978-0-470-13148-0.

[100] A. Rohatgi, *Webplotdigitizer*, version 5.2. [Online]. Available: https://automeris.io.

[101] F. H. Panther, I. R. Seitenzahl, A. J. Ruiter, T. Siegert, S. Sim, and R. M. Crocker, "Prospects of direct detection of ^{48}V gamma-rays from thermonuclear supernovae,", vol. 508, no. 2, pp. 1590–1598, Dec. 2021. DOI: 10.1093/mnras/stab2701. arXiv: 2103.16840 [astro-ph.HE].

[102] M. D. Leising, W. N. Johnson, J. D. Kurfess, *et al.*, "Compton Gamma Ray Observatory OSSE Observations of SN 1991T,", vol. 450, p. 805, Sep. 1995. DOI: 10.1086/176185.

[103] G. G. Lichti, K. Bennett, J. W. den Herder, *et al.*, "COMPTEL upper limits on gamma-ray line emission from Supernova 1991T.,", vol. 292, p. 569, Dec. 1994.

[104] K. Maeda and K. Iwamoto, "Observational characteristics and possible asphericity of overluminous type ia supernovae," *Monthly Notices of the Royal Astronomical Society*, vol. 394, no. 1, pp. 239–249, Mar. 2009, ISSN: 1365-2966. DOI: 10.1111/j.1365-2966.2008.14179.x. [Online]. Available: http://dx.doi.org/10.1111/j.1365-2966.2008.14179.x.

[105] K. Maeda, S. Taubenberger, J. Sollerman, *et al.*, "Nebular Spectra and Explosion Asymmetry of Type Ia Supernovae,", vol. 708, no. 2, pp. 1703–1715, Jan. 2010. DOI: 10.1088/0004-637X/708/2/1703. arXiv: 0911.5484 [astro-ph.SR].

[106] V. V. Flambaum and P. Munro-Laylim, "Spacetime variation of the s and c quark masses," *Phys. Rev. D*, vol. 107, p. 015 004, 1 Jan. 2023. DOI: 10.1103/PhysRevD.107.015004. [Online]. Available: https://link.aps.org/doi/10.1103/PhysRevD.107.015004.

[107] T. H. Dinh, A. Dunning, V. A. Dzuba, and V. V. Flambaum, "Sensitivity of hyperfine structure to nuclear radius and quark mass variation," *Phys. Rev. A*, vol. 79, p. 054 102, 5 May 2009. DOI: 10.1103/PhysRevA.79.054102. [Online]. Available: https://link.aps.org/doi/10.1103/PhysRevA.79.054102.

[108] R. H. Wechsler and J. L. Tinker, "The connection between galaxies and their dark matter halos," *Annual Review of Astronomy and Astrophysics*, vol. 56, no. Volume 56, 2018, pp. 435–487, 2018, ISSN: 1545-4282. DOI: https://doi.org/10.1146/annurev-astro-081817-051756. [Online]. Available: https://www.annualreviews.org/content/journals/10.1146/annurev-astro-081817-051756.

[109] G. F. R. Ellis, "Dark energy and inhomogeneity," *Journal of Physics: Conference Series*, vol. 189, no. 1, p. 012 011, Oct. 2009. DOI: 10.1088/1742-6596/189/1/012011. [Online]. Available: https://dx.doi.org/10.1088/1742-6596/189/1/012011.

[110] N. J. Nunes and D. F. Mota, "Structure formation in inhomogeneous dark energy models," *Monthly Notices of the Royal Astronomical Society*, vol. 368, no. 2, pp. 751–758, May 2006, ISSN: 0035-8711. DOI: 10.1111/j.1365-2966.2006.10166.x. eprint: https://academic.oup.com/mnras/article-pdf/368/2/751/3078509/mnras0368-0751.pdf. [Online]. Available: https://doi.org/10.1111/j.1365-2966.2006.10166.x.

[111] V. V. Flambaum and V. A. Dzuba, "Search for variation of the fundamental constants in atomic, molecular, and nuclear spectra," *Canadian Journal of Physics*, vol. 87, no. 1, pp. 25–33, 2009. DOI: 10.1139/p08-072. eprint: https://doi.org/10.1139/p08-072. [Online]. Available: https://doi.org/10.1139/p08-072.

[112] O. Avsajanishvili, G. Y. Chitov, T. Kahniashvili, S. Mandal, and L. Samushia, "Observational constraints on dynamical dark energy models," *Universe*, vol. 10, no. 3, p. 122, Mar. 2024, ISSN: 2218-1997. DOI: 10.3390/universe10030122. [Online]. Available: http://dx.doi.org/10.3390/universe10030122.

[113] P. S. Corasaniti and E. J. Copeland, "Constraining the quintessence equation of state with snia data and cmb peaks," *Physical Review D*, vol. 65, no. 4, Jan. 2002, ISSN: 1089-4918. DOI: 10.1103/physrevd.65.043004. [Online]. Available: http://dx.doi.org/10.1103/PhysRevD.65.043004.

[114] T. Aoyama, N. Asmussen, M. Benayoun, *et al.*, "The anomalous magnetic moment of the muon in the standard model," *Physics Reports*, vol. 887, pp. 1–166, 2020, The anomalous magnetic moment of the muon in the Standard Model, ISSN: 0370-1573. DOI: https://doi.org/10.1016/j.physrep.2020.07.006. [Online]. Available: https://www.sciencedirect.com/science/article/pii/S0370157320302556.

[115] T. Aoyama, T. Kinoshita, and M. Nio, "Theory of the anomalous magnetic moment of the electron," *Atoms*, vol. 7, no. 1, 2019, ISSN: 2218-2004. DOI: 10.3390/atoms7010028. [Online]. Available: https://www.mdpi.com/2218-2004/7/1/28.

[116] M. C. Gonzalez-Garcia and Y. Nir, "Neutrino masses and mixing: Evidence and implications," *Rev. Mod. Phys.*, vol. 75, pp. 345–402, 2 Mar. 2003. DOI: 10.1103/RevModPhys.75.345. [Online]. Available: https://link.aps.org/doi/10.1103/RevModPhys.75.345.

[117] C. Weinheimer and K. Zuber, "Neutrino masses," *Annalen der Physik*, vol. 525, no. 8-9, pp. 565–575, 2013. DOI: https://doi.org/10.1002/andp.201300063. eprint: https://onlinelibrary.wiley.com/doi/pdf/10.1002/andp.201300063. [Online]. Available: https://onlinelibrary.wiley.com/doi/abs/10.1002/andp.201300063.

[118] A. Y. SMIRNOV, "Neutrino physics: Open theoretical questions," *International Journal of Modern Physics A*, vol. 19, no. 08, pp. 1180–1197, Mar. 2004, ISSN: 1793-656X. DOI: 10.1142/s0217751x0401910x. [Online]. Available: http://dx.doi.org/10.1142/S0217751X0401910X.

[119] M. Aker, D. Batzler, A. Beglarian, *et al.*, *Direct neutrino-mass measurement based on 259 days of katrin data*, 2024. arXiv: 2406.13516 [nucl-ex]. [Online]. Available: https://arxiv.org/abs/2406.13516.

[120] Y. Nomura, T. Watari, and T. Yanagida, "Quintessence axion potential induced by electroweak instanton effects," *Physics Letters B*, vol. 484, no. 12, pp. 103–111, Jun. 2000, ISSN: 0370-2693. DOI: 10.1016/s0370-2693(00)00605-5. [Online]. Available: http://dx.doi.org/10.1016/S0370-2693(00)00605-5.

[121] M. W. Hossain and A. Maqsood, *Cosmological implications of tracker scalar fields as dynamical dark energy*, 2025. arXiv: 2502.19274 [astro-ph.CO]. [Online]. Available: https://arxiv.org/abs/2502.19274.

[122] A. D. Rendall, "Dynamics of k-essence," *Classical and Quantum Gravity*, vol. 23, no. 5, pp. 1557–1569, Feb. 2006, ISSN: 1361-6382. DOI: 10.1088/0264-9381/23/5/008. [Online]. Available: http://dx.doi.org/10.1088/0264-9381/23/5/008.

[123] S. Tian and Z.-H. Zhu, "Early dark energy in k-essence," *Physical Review D*, vol. 103, no. 4, Feb. 2021, ISSN: 2470-0029. DOI: 10.1103/physrevd.103.043518. [Online]. Available: http://dx.doi.org/10.1103/PhysRevD.103.043518.

[124] C. Armendariz-Picon, V. Mukhanov, and P. J. Steinhardt, "Essentials ofk-essence," *Physical Review D*, vol. 63, no. 10, Apr. 2001, ISSN: 1089-4918. DOI: 10.1103/physrevd.63.103510. [Online]. Available: http://dx.doi.org/10.1103/PhysRevD.63.103510.

[125] M. Malquarti, E. J. Copeland, and A. R. Liddle, "k-essence and the coincidence problem," *Physical Review D*, vol. 68, no. 2, Jul. 2003, ISSN: 1089-4918. DOI: 10.1103/physrevd.68.023512. [Online]. Available: http://dx.doi.org/10.1103/PhysRevD.68.023512.

[126] K. J. Ludwick, "The viability of phantom dark energy: A review," *Modern Physics Letters A*, vol. 32, no. 28, p. 1 730 025, 2017. DOI: 10.1142/S0217732317300257. eprint: https://doi.org/10.1142/S0217732317300257. [Online]. Available: https://doi.org/10.1142/S0217732317300257.

[127] G. Leon, A. Paliathanasis, and J. L. Morales-Martínez, "The past and future dynamics of quintom dark energy models," *The European Physical Journal C*, vol. 78, no. 9, Sep. 2018, ISSN: 1434-6052. DOI: 10.1140/epjc/s10052-018-6225-y. [Online]. Available: http://dx.doi.org/10.1140/epjc/s10052-018-6225-y.

A. DERIVATION OF PION MASS DEPENDENCE ON THE QCD VACUUM ANGLE AND ITS VARIATION

The dependence of the pion mass on the QCD vacuum angle θ is derived in [11]. The derivation will be included in this appendix for the sake of completeness. Also included are the steps to find the resulting pion mass deviation for small nonzero values of the QCD vacuum.

A.1 Pion Mass Dependence on θ

The derivation starts with the convenient step of eliminating the CP violating term

$$\mathcal{L}_\theta = -\theta \frac{g_S^2}{32\pi^2} G_{l\mu\nu} \tilde{G}^{l\mu\nu} \tag{A.1}$$

from the QCD Lagrangian by rotating the quark fields

$$u \to \mathrm{e}^{\mathrm{i}\phi_u} u, \tag{A.2}$$

$$d \to \mathrm{e}^{\mathrm{i}\phi_d} d, \tag{A.3}$$

where u is the up-quark field, d is the down quark field, and ϕ_u and ϕ_d are their respective phases that obey

$$\phi_u + \phi_d = \theta. \tag{A.4}$$

Consequently, the quark mass matrix, given by MU_0 where

$$M = \begin{pmatrix} m_u & 0 \\ 0 & m_d \end{pmatrix}, \quad U_0 = \begin{pmatrix} \mathrm{e}^{\mathrm{i}\phi_u} & 0 \\ 0 & \mathrm{e}^{\mathrm{i}\phi_d} \end{pmatrix}, \tag{A.5}$$

now depends on the QCD vacuum angle. Above, m_u and m_d are the masses of the up and down quarks, respectively.

The effective Lagrangian of the sigma model, which is an accurate description of QCD in the low energy limit, is written as

$$\mathcal{L} \supset -\frac{1}{4} f_\pi^2 \mathrm{Tr}\left[\partial_\mu U \partial^\mu U^\dagger\right] + B_0 \mathrm{Tr}\left[(MU_0)U + (MU_0)^\dagger U^\dagger\right], \tag{A.6}$$

where $U = \mathrm{e}^{\boldsymbol{\pi}^a \tau^a / f_\pi}$, $\boldsymbol{\pi}^a$ is the pion field, τ^a are the isospin matrices (which are proportional to the Pauli matrices), f_π is the pion decay constant, and B_0 is a constant determined by the ratio of meson masses. These last two quantities are taken to have values of $f_\pi = 92.4$ MeV and $B_0 = 7.6 \times 10^6$ MeV^3. The sigma model Lagrangian has many more terms containing the nucleon fields; however, these are the only two terms needed for finding the value of the pion mass.

The matrix U can be expanded as

$$\begin{aligned} U &= \mathrm{e}^{\mathrm{i}\boldsymbol{\pi}^a \tau^a / f_\pi} \\ &= \sum_{n=0}^{\infty} \frac{1}{n!} \left(\frac{\mathrm{i}}{f_\pi}\right)^n (\boldsymbol{\pi}^a \tau^a)^n, \\ &= 1 + \mathbf{1}_2 \sum_{n \text{ even}} \frac{1}{n!} \left(\frac{\mathrm{i}}{f_\pi}\right)^n (\boldsymbol{\pi}^a \boldsymbol{\pi}^a)^{n/2} + \sum_{n \text{ odd}} \frac{1}{n!} \left(\frac{\mathrm{i}}{f_\pi}\right)^n (\boldsymbol{\pi}^a \boldsymbol{\pi}^a)^{n/2} \left(\frac{\boldsymbol{\pi}^a \tau^a}{\|\vec{\boldsymbol{\pi}}\|}\right), \\ &= \cos \frac{\|\vec{\boldsymbol{\pi}}\|}{f_\pi} + \mathrm{i} \frac{\boldsymbol{\pi}^a}{\|\vec{\boldsymbol{\pi}}\|} \tau^a \sin \frac{\|\vec{\boldsymbol{\pi}}\|}{f_\pi}, \end{aligned} \tag{A.7}$$

where $\mathbf{1}_2$ is the 2×2 identity matrix and

$$\|\boldsymbol{\pi}^a\| = \sqrt{\boldsymbol{\pi}_1^2 + \boldsymbol{\pi}_2^2 + \boldsymbol{\pi}_3^2}. \tag{A.8}$$

Furthermore, the matrix MU_0 can be expanded in the most general form of any 2×2 matrix as

$$MU_0 = A\mathbf{1}_2 + \mathrm{i}B\mathbf{1}_2 + C\tau^3 + \mathrm{i}D\tau^3. \tag{A.9}$$

Using both of the above expansions, the potential in the Lagrangian for the pion can be expressed as

$$V = -B_0 \mathrm{Tr}\left[(MU_0)U + (MU_0)^\dagger U^\dagger\right]. \tag{A.10}$$

Once the matrices are multiplied, added, and the trace is taken, the final expression is

$$V = -B_0 \left[4A \cos \frac{\|\vec{\boldsymbol{\pi}}\|}{f_\pi} - 4D \frac{\boldsymbol{\pi}^3}{\|\vec{\boldsymbol{\pi}}\|} \sin \frac{\|\vec{\boldsymbol{\pi}}\|}{f_\pi} \right]. \tag{A.11}$$

This can be derived mechanically by expanding each term out as a matrix and using the usual rules for multiplying and finding the Hermitian conjugate of matrices. To prevent the contribution of an imaginary term to the quark mass, D must be zero. The expansion of MU_0 implies that the coefficient D is the same as

$$D = \frac{1}{2}\mathrm{Tr}\left[\tau^3 \begin{pmatrix} m_u \sin\phi_u & 0 \\ 0 & m_d \sin\phi_d \end{pmatrix} \right] = \frac{1}{2}(m_u \sin\phi_u - m_d \sin\phi_d) = 0. \tag{A.12}$$

The above equation and Equation (A.1) can be used to find the sine and cosine of each phase. The derivation of the $\sin\phi_u$ will be shown in detail. The other equations can be found by similar steps.

$$\begin{aligned} 0 = m_u \sin\phi_u - m_d \sin\phi_d &= m_u \sin\phi_u - m_d \sin(\theta - \phi_u) \\ &= m_u sin\phi_u - m_d \sin\theta \cos\phi_u + m_d \cos\theta \sin\phi_u \\ &= m_u sin\phi_u - m_d \sin\theta \sqrt{1 - \sin^2\phi_u} + m_d \cos\theta \sin\phi_u \end{aligned}$$

Bringing the second term to the left-hand side, squaring both sides, and then isolating $\sin\phi_u$ yields

$$\begin{aligned} \sin^2\phi_u &= \frac{(m_d \sin\theta)^2}{(m_u + m_d\cos\theta)^2} \frac{1}{\left(1 + \frac{(m_d\sin\theta)^2}{(m_u + m_d\cos\theta)^2}\right)} \\ &= \frac{(m_d\sin\theta)^2}{m_u^2 + m_d^2 + 2m_u m_d \cos\theta}. \end{aligned}$$

Finally, taking the square root yields

$$\sin\phi_u = \frac{m_d \sin\theta}{(m_u^2 + m_d^2 + 2m_u m_d \cos\theta)^{1/2}}. \tag{A.13}$$

The rest of the equations, found in a similar way, are

$$\sin\phi_d = \frac{m_u \sin\theta}{(m_u^2 + m_d^2 + 2m_u m_d \cos\theta)^{1/2}}, \tag{A.14}$$

$$\cos\phi_u = \frac{m_u + m_d \cos\theta}{(m_u^2 + m_d^2 + 2m_u m_d \cos\theta)^{1/2}}, \tag{A.15}$$

$$\cos\phi_u = \frac{m_d + m_u \cos\theta}{(m_u^2 + m_d^2 + 2m_u m_d \cos\theta)^{1/2}}. \tag{A.16}$$

The coefficient A is

$$A = \frac{1}{2}\mathrm{Tr}\begin{pmatrix} m_u\cos\phi_u & 0 \\ 0 & m_d\cos\phi_d \end{pmatrix} = \frac{1}{2}(m_u\cos\phi_u + m_d\cos\phi_d). \tag{A.17}$$

The second order term of Equation (A.1) when expanded corresponds with the pion mass. The second order term is

$$\begin{aligned} m_\pi^2 &= \frac{4AB_0}{f_\pi^2} = \frac{2B_0}{f_\pi^2}(m_u\cos\phi_u + m_d\cos\phi_d) \\ &= \frac{2B_0}{f_\pi^2}\left(\frac{m_u^2 + m_d^2 + 2m_u m_d\cos\theta}{(m_u^2 + m_d^2 + 2m_u m_d\cos\theta)^{1/2}}\right), \end{aligned}$$

which yields the pion mass-squared as

$$m_\pi^2 = \frac{2B_0}{f_\pi^2}(m_u^2 + m_d^2 + 2m_u m_d\cos\theta)^{1/2}. \tag{A.18}$$

A.2 Variation of the Pion Mass

How the mass of the pion will vary when θ is a small angle not equal to zero follows readily from the last equation of the preceding section. Expanding the cosine to second order and then simplifying the resulting expression is carried out below

$$\begin{aligned} m_\pi &\approx \sqrt{\frac{2B_0}{f_\pi^2}}(m_u^2 + m_d^2 + 2m_u m_d(1 - \theta^2/2))^{1/4} \\ &= \sqrt{\frac{2B_0}{f_\pi^2}}(m_u^2 + m_d^2 + 2m_u m_d - m_u m_d \theta^2)^{1/4} \\ &= \sqrt{\frac{2B_0}{f_\pi^2}}[(m_u + m_d)^2 - m_u m_d \theta^2]^{1/4} \\ &\approx \sqrt{\frac{2B_0}{f_\pi^2}}(m_u + m_d)^{1/2} - \sqrt{\frac{2B_0}{f_\pi^2}}\frac{m_u m_d}{4(m_u + m_d)^{3/2}}\theta^2, \end{aligned}$$

making the final result

$$m_\pi \equiv \bar{m}_\pi + \delta\bar{m}_\pi. \tag{A.19}$$

Above, $\bar{m}_\pi$ is the expected mass of the pion with $\theta = 0$. Taking the ratio of $\delta\bar{m}_\pi$ and $\bar{m}_\pi$ and plugging in the values of the quark masses yields

$$\frac{\delta m_\pi}{m_\pi} = -\frac{m_u m_d}{4(m_u + m_d)^2}\theta^2 \approx -0.05\theta^2, \tag{A.20}$$

where the bar over m_π was dropped for convenience. The above result agrees with the expression given in [12].

B. COMPTEL BACKGROUND AND SN 1991T DATA

This appendix contains the data points for the COMPTEL background and the background-subtracted gamma ray data from SN1991T. These data points were extracted using `WebPlotDigitizer` [100] from the respective plots in [5].

B.1 COMPTEL Background Data Points

Table B.1. One example of data points for a background model of COMPTEL. The count error was taken to be the square root of the number of counts.

Counts	Energy (keV)	Count Error
2,620.85	726.397	51.1943
13,799.4	772.54	1117.471
21,460	823.366	146.492
25,849	874.543	160.776
28,386.5	928.072	168.483
29,380	975.311	171.406
29,818.4	1,026.91	172.68
29,700.6	1,072.12	172.339
29,336.1	1,119.51	171.278
28,664	1,175.53	169.304
27,805.9	1,225.12	166.751
27,132.7	1,272.54	164.72
27,077.4	1,324.2	164.552
27,700.5	1,371.47	166.435
28,628.8	1,390.74	169.2
29,743.9	1,422.9	172.464
30,429.3	1,474.48	174.44
27,904.8	1,526.4	167.047
24,824.3	1,574.08	157.557
22,546.5	1,623.82	150.155
20,885.7	1,671.35	144.519
19,780.9	1,723.12	140.645
18,737.7	1,772.73	136.886
17,942.7	1,833.07	133.95
17,330.7	1,876.18	131.646
16,842.5	1,921.42	129.779
16,046.1	1,971.01	126.673
15,497.2	2,024.87	124.488
15,564.8	2,072.21	124.759
16,928.9	2,121.56	130.111

17,919.7	2,147.28	133.865
18,972	2,170.84	137.739
20,212.9	2,222.35	142.172
18,429	2,272.04	135.753
15,534.1	2,324	124.636
13,194.6	2,373.75	114.868
11,842.7	2,423.4	108.824
11,170.1	2,475.12	105.689
10,744.1	2,524.66	103.654
10,317.8	2,572.05	101.577
10,139	2,623.72	100.693
10,268.3	2,671.05	101.333
10,151.3	2,722.72	100.753
10,218.8	2,770.06	101.088
10,163.2	2,819.56	100.813
9,860.69	2,869.09	99.301
9,496.7	2,920.78	97.451
9,688	2,970.26	98.4276

B.2 1991T Background-Subtracted Data Points

Table B.2. Spectroscopic data of SN1991T after the background model is subtracted off. The count error was extracted from the error bars provided in [5].

Counts	Energy (keV)	Count Error
-12.803	726.273	19.5923
211.366	776.828	52.2461
321.246	827.124	62.0422
186.223	876.862	63.6749
-87.5873	925.375	75.1215
-137.693	977.126	78.3602
52.1807	1,026.69	80.0107
117.979	1,076.89	78.378
304.604	1,128.27	78.3691
138.551	1,177.03	81.6345
321.903	1,227.49	84.8999
247.289	1,277.36	78.378
61.6441	1,326.08	78.378
-3.17327	1,375.98	80.0107
29.9708	1,426.1	81.6345
33.7264	1,476.15	83.2672
-29.4582	1,526.05	78.3691
-32.2423	1,575.18	76.7364
-20.3232	1,625.25	75.0948
132.007	1,675.65	68.573
32.8945	1,724.56	71.8383
-136.415	1,774.22	66.9403

C. REPRESENTATIVE VALUES OF $\dot{Q}$

Representative values of $\dot{Q}$ and their uncertainties at one standard deviation for evenly spaced values of α from 0.005 to 0.1 and values of the power of the tracking potential p from 1 to 10. These values are calculated from the average energy deviations as indicated by the gamma rays emitted by ^{56}Fe in SN 1991T. Furthermore, as explained in the previous chapters, these values result after assuming that the decay constant is $f_Q = \alpha M_{pl}/\sqrt{8\pi}$ so that the mass of the field will not cause an accelerated expansion rate of the universe larger than the value suggested by observation. Also, it is assumed that most of the dark energy density is contained in the potential so that Q will behave approximately as a cosmological constant. The first pair of tables is for the nucleus modeled as a rigid rotor and the second pair of tables is for the nucleus modeled as a vibrating liquid drop. For this latter model the values of $\dot{Q}$ will be larger by approximately 12%.

Table C.1. Resulting upper limits on $\dot{Q}$ (upper table, in units of GeV/yr) with one standard deviation (lower table, also in units of GeV/yr) for the nucleus modeled as a deformed rigid rotor for different values of p and α. The values of α are chose to be evenly spaced between the lowest value considered of 0.05 and 0.1.

α	p=1	2	3	4	5	6	7	8	9	10
0.005	2.66E+05	1.86E+05	1.65E+05	1.55E+05	1.50E+05	1.46E+05	1.43E+05	1.42E+05	1.40E+05	1.39E+05
0.0145	2.24E+06	1.57E+06	1.40E+06	1.30E+06	1.26E+06	1.23E+06	1.20E+06	1.19E+06	1.18E+06	1.17E+06
0.024	6.14E+06	4.28E+06	3.81E+06	3.58E+06	3.45E+06	3.37E+06	3.30E+06	3.26E+06	3.23E+06	3.21E+06
0.0335	1.19E+07	8.34E+06	7.40E+06	6.96E+06	6.72E+06	6.56E+06	6.45E+06	6.37E+06	6.30E+06	6.25E+06
0.043	1.97E+07	1.37E+07	1.22E+07	1.15E+07	1.11E+07	1.08E+07	1.06E+07	1.05E+07	1.04E+07	1.03E+07
0.0525	2.93E+07	2.05E+07	1.82E+07	1.71E+07	1.65E+07	1.61E+07	1.59E+07	1.57E+07	1.54E+07	1.53E+07
0.062	4.10E+07	2.86E+07	2.53E+07	2.39E+07	2.30E+07	2.24E+07	2.21E+07	2.18E+07	2.16E+07	2.15E+07
0.0715	5.45E+07	3.80E+07	3.37E+07	3.18E+07	3.07E+07	2.99E+07	2.93E+07	2.90E+07	2.87E+07	2.85E+07
0.081	6.99E+07	4.87E+07	4.33E+07	4.07E+07	3.93E+07	3.83E+07	3.77E+07	3.72E+07	3.70E+07	3.66E+07
0.0905	8.73E+07	6.09E+07	5.40E+07	5.08E+07	4.91E+07	4.79E+07	4.71E+07	4.64E+07	4.60E+07	4.57E+07
0.1	1.07E+08	7.44E+07	6.60E+07	6.21E+07	5.99E+07	5.85E+07	5.75E+07	5.67E+07	5.62E+07	5.57E+07

α	p=1	2	3	4	5	6	7	8	9	10
0.005	8.65E+04	6.03E+04	5.35E+04	5.04E+04	4.86E+04	4.75E+04	4.67E+04	4.61E+04	4.56E+04	4.52E+04
0.0145	7.27E+05	5.07E+05	4.49E+05	4.23E+05	4.08E+05	3.99E+05	3.92E+05	3.87E+05	3.83E+05	3.80E+05
0.024	1.99E+06	1.39E+06	1.23E+06	1.16E+06	1.12E+06	1.09E+06	1.07E+06	1.06E+06	1.05E+06	1.04E+06
0.0335	3.88E+06	2.70E+06	2.40E+06	2.26E+06	2.18E+06	2.13E+06	2.09E+06	2.07E+06	2.04E+06	2.03E+06
0.043	6.39E+06	4.46E+06	3.95E+06	3.73E+06	3.59E+06	3.51E+06	3.45E+06	3.41E+06	3.37E+06	3.34E+06
0.0525	9.55E+06	6.65E+06	5.90E+06	5.56E+06	5.36E+06	5.24E+06	5.15E+06	5.09E+06	5.03E+06	4.99E+06
0.062	1.33E+07	9.27E+06	8.22E+06	7.75E+06	7.47E+06	7.30E+06	7.18E+06	7.08E+06	7.01E+06	6.95E+06
0.0715	1.77E+07	1.23E+07	1.09E+07	1.03E+07	9.93E+06	9.71E+06	9.54E+06	9.42E+06	9.32E+06	9.24E+06
0.081	2.27E+07	1.58E+07	1.40E+07	1.32E+07	1.27E+07	1.24E+07	1.22E+07	1.21E+07	1.20E+07	1.18E+07
0.0905	2.83E+07	1.97E+07	1.75E+07	1.65E+07	1.59E+07	1.55E+07	1.53E+07	1.51E+07	1.49E+07	1.48E+07
0.1	3.46E+07	2.41E+07	2.14E+07	2.02E+07	1.94E+07	1.90E+07	1.87E+07	1.84E+07	1.82E+07	1.81E+07

Table C.2. Resulting upper limits on $\dot{Q}$ (upper table, in units of GeV/yr) with one standard deviation (lower table, also in units of GeV/yr) for the nucleus modeled as a charged liquid drop undergoing surface vibrations for different values of p and α. It should be noted that the upper limit for $\dot{Q}$ for a given value of α and p is higher than the upper limit for the deformed rigid rotor by 12%.

α	p=1	2	3	4	5	6	7	8	9	10
0.005	3.03E+05	2.11E+05	1.87E+05	1.76E+05	1.71E+05	1.66E+05	1.63E+05	1.61E+05	1.60E+05	1.59E+05
0.0145	2.55E+06	1.77E+06	1.58E+06	1.49E+06	1.43E+06	1.40E+06	1.38E+06	1.36E+06	1.35E+06	1.34E+06
0.024	6.99E+06	4.87E+06	4.33E+06	4.07E+06	3.93E+06	3.83E+06	3.77E+06	3.72E+06	3.68E+06	3.66E+06
0.0335	1.36E+07	9.50E+06	8.42E+06	7.93E+06	7.65E+06	7.47E+06	7.34E+06	7.25E+06	7.17E+06	7.12E+06
0.043	2.24E+07	1.57E+07	1.39E+07	1.30E+07	1.26E+07	1.23E+07	1.20E+07	1.19E+07	1.18E+07	1.17E+07
0.0525	3.34E+07	2.33E+07	2.07E+07	1.95E+07	1.88E+07	1.83E+07	1.81E+07	1.78E+07	1.76E+07	1.75E+07
0.062	4.66E+07	3.25E+07	2.88E+07	2.72E+07	2.62E+07	2.56E+07	2.52E+07	2.49E+07	2.45E+07	2.44E+07
0.0715	6.20E+07	4.33E+07	3.83E+07	3.61E+07	3.48E+07	3.41E+07	3.34E+07	3.30E+07	3.26E+07	3.24E+07
0.081	7.96E+07	5.55E+07	4.93E+07	4.63E+07	4.47E+07	4.37E+07	4.29E+07	4.24E+07	4.19E+07	4.16E+07
0.0905	9.93E+07	6.93E+07	6.13E+07	5.78E+07	5.58E+07	5.45E+07	5.35E+07	5.29E+07	5.23E+07	5.19E+07
0.1	1.22E+08	8.46E+07	7.50E+07	7.06E+07	6.81E+07	6.66E+07	6.54E+07	6.46E+07	6.40E+07	6.34E+07

α	p=1	2	3	4	5	6	7	8	9	10
0.005	9.69E+04	6.75E+04	5.99E+04	5.64E+04	5.44E+04	5.32E+04	5.23E+04	5.16E+04	5.11E+04	5.06E+04
0.0145	8.14E+05	5.67E+05	5.03E+05	4.74E+05	4.57E+05	4.47E+05	4.39E+05	4.34E+05	4.29E+05	4.25E+05
0.024	2.23E+06	1.55E+06	1.38E+06	1.30E+06	1.25E+06	1.22E+06	1.20E+06	1.19E+06	1.17E+06	1.16E+06
0.0335	4.34E+06	3.03E+06	2.69E+06	2.53E+06	2.44E+06	2.39E+06	2.34E+06	2.31E+06	2.29E+06	2.27E+06
0.043	7.16E+06	4.99E+06	4.43E+06	4.17E+06	4.02E+06	3.93E+06	3.87E+06	3.82E+06	3.77E+06	3.74E+06
0.0525	1.07E+07	7.45E+06	6.61E+06	6.23E+06	6.01E+06	5.87E+06	5.77E+06	5.70E+06	5.64E+06	5.59E+06
0.062	1.49E+07	1.04E+07	9.21E+06	8.68E+06	8.37E+06	8.18E+06	8.04E+06	7.94E+06	7.85E+06	7.78E+06
0.0715	1.98E+07	1.38E+07	1.22E+07	1.15E+07	1.11E+07	1.09E+07	1.07E+07	1.06E+07	1.04E+07	1.03E+07
0.081	2.54E+07	1.77E+07	1.57E+07	1.48E+07	1.43E+07	1.39E+07	1.37E+07	1.35E+07	1.34E+07	1.33E+07
0.0905	3.17E+07	2.21E+07	1.96E+07	1.85E+07	1.78E+07	1.74E+07	1.71E+07	1.69E+07	1.67E+07	1.66E+07
0.1	3.87E+07	2.70E+07	2.40E+07	2.26E+07	2.18E+07	2.13E+07	2.09E+07	2.07E+07	2.04E+07	2.02E+07

D. MATLAB CODE FOR CALCULATING $\dot{Q}$ AND PLOTTING PARAMETER SPACES

This appendix contains the code for calculating the values of $\dot{Q}$ and plotting the allowed parameter spaces for both the nucleus as a rigid rotor and vibrating liquid drop. All values used for astrophysical constants and parameters are taken from [72].

D.1 Rigid Rotor Model

```
% Clear all variables in MATLAB
clear;

length_conversion = 1.9733*10^(-16);                    % m*GeV
time_conversion = 6.5823*10^(-25);                      % s*GeV
planck_mass = 1.22093*10^(19);                          % GeV

%Fractional energy density of dark energy.
omega_Lambda = 0.685;

% Scaling factor for Hubble expansion rate.
h = 0.673;

rho_crit = h^2*1.05375*10^(-5);                         % GeV/cm^3
f_Q = planck_mass/sqrt(8*pi);                           % GeV

% Averaged gamma ray energy deviation.
dEoverE = .023;

% Time light takes to rach earth from 91T.
delta_t = 44*10^6;

% Max allowed value of the DE EoS parameter.
w_DE_max = -0.972;

% Max fractional kinetic energy density allowed for w_DE_max.
Omega_KE_max = -(w_DE_max+1)/(w_DE_max-1)*omega_Lambda;

% Declare variables that will later act as arrays.
Omega_KE_space = 0;
alpha=0;
power_list=0;
Omega_KE=0;
i=0;
alphamax=0;
Q_dot_list=0;

% Loop through values of decay constant coefficients
% from 0.005 to 0.2 in 0.001 increments.
for al=0.005:0.001:0.2
```

```
i=i+1;
j=0;

% Loop through values of the tracking potential power
% from 1 to 10 in 0.01 increments.
for p=1:0.01:10
    j=j+1;
    alpha(i,j)=al;
    power_list(i,j)=p;

    % Calculate the cosmological constant term of the
    % quintessence field for a value of p.
    Q_Lambda = planck_mass/sqrt(8*pi)*1/(3*omega_Lambda)^(1/p);

    % Calculate the maximum value of the decay constant
    % coefficent such that the kinetic energy density
    % doe not exceed 10 percent the energy density of DE.
    alphamax(j) = sqrt(.24*Q_Lambda*delta_t*3.154*10^7/time_conversion/dEoverE)*...
        (omega_Lambda*rho_crit*length_conversion^3/10^(-6)/5)^(1/4)/f_Q;

    % Exclude fractional kinetic energy densities that exceed
    % 10 percent of dark energy density.
    if al>alphamax(j)
        Omega_KE(i,j)=NaN;
    else

        % Compute Q_dot for rigid rotor model.
        Q_dot = (al*f_Q)^2/(0.24*Q_Lambda*delta_t)*dEoverE;          % GeV/yr
        Q_dot_list(i,j)=Q_dot;

        % Convert Q_dot to natural units.
        Q_dot_natural = Q_dot*time_conversion/(3.154*10^7);          % GeV^2

        % Compute kinetic energy density.
        rho_KE = Q_dot_natural^2/2;                                  % GeV^4

        % Covert kinetic energy density to intuite units.
        rho_KE_intuitive = rho_KE/length_conversion^3*10^(-6);       % GeV/cm^3

        % Compute fractional kinetic energy density.
        Omega_KE(i,j) = rho_KE_intuitive/rho_crit;

    end

    % Exclude fractional kinetic energy densities
    % where the equation of state parameter will
    % exceed that of w_DE_max.
    if Omega_KE(i,j)>Omega_KE_max
            Omega_KE_space(i,j) = NaN;
    else
            Omega_KE_space(i,j) = Omega_KE(i,j);
    end
```

```
   end
end

% Plot parameter spaces with color bar that indicates
% the value of the fractional kinetic energy density.
figure;
h1=pcolor(power_list,alpha,Omega_KE);
set(h1, 'EdgeColor', 'none');
colormap('jet');
set(gca,'ColorScale','linear');
c1 = colorbar;
c1.Label.String = '\Omega_{KE,rig}';

figure;
h2=pcolor(power_list,alpha,Omega_KE_space);
set(h2, 'EdgeColor', 'none');
colormap('jet');
set(gca,'ColorScale','linear');
c2 = colorbar;
c2.Label.String = '\Omega_{KE,rig}';
```

D.2 Phonon Model

```
% Clear all variables in MATLAB
clear;

length_conversion = 1.9733*10^(-16);                                % m*GeV
time_conversion = 6.5823*10^(-25);                                  % s*GeV
planck_mass = 1.22093*10^(19);                                      % GeV

%Fractional energy density of dark energy.
omega_Lambda = 0.685;

% Scaling factor for Hubble expansion rate.
h = 0.673;

rho_crit = h^2*1.05375*10^(-5);                                     % GeV/cm^3
f_Q = planck_mass/sqrt(8*pi);                                       % GeV

% Averaged gamma ray energy deviation.
dEoverE = .023;

% Time light takes to rach earth from 91T.
delta_t = 44*10^6;

% Max allowed value of the DE EoS parameter.
w_DE_max = -0.972;

% Max fractional kinetic energy density allowed for w_DE_max.
Omega_KE_max = -(w_DE_max+1)/(w_DE_max-1)*omega_Lambda;

% Atomic number of iron-56.
Z = 26;

% Mass number of iron-56.
A = 56;

% Value of the coefficient of the A^(2/3) term
% in the semi-empirical mass formula.
S = 18.56*10^(-3);                                          % GeV

% Experimentally determined parameter used
% to predict the radius of a nucleus.
r_0 = 1.2*10^(-15)/length_conversion;                       % GeV^-1

% Fundamental unit charge in
% natural units.
charge = 0.30282;

% Dimensionless constant needed for the
% determination of Q_dot.
xi = 3*Z^2*charge^2/(10*A*S*r_0);

% Declare variables that will later act as arrays.
```

```
alpha=0;
power_list=0;
Omega_KE=0;
Omega_KE_space = 0;
i=0;
alphamax=0;
Q_dot_list=0;

% Loop through values of decay constant coefficients
% from 0.005 to 0.2 in 0.001 increments.
for al=0.005:0.001:0.2
    i=i+1;
    j=0;

    % Loop through values of the tracking potential power
    % from 1 to 10 in 0.01 increments.
    for p=1:0.01:10
        j=j+1;
        alpha(i,j)=al;
        power_list(i,j)=p;

        % Calculate the cosmological constant term of the
        % quintessence field for a value of p.
        Q_Lambda = planck_mass/sqrt(8*pi)*1/(3*omega_Lambda)^(1/p);

        % Calculate the maximum value of the decay constant
        % coefficent such that the kinetic energy density
        % doe not exceed 10 percent the energy density of DE.
        alphamax(j) = sqrt(.12*Q_Lambda*delta_t*3.154*10^7/time_conversion*(1-3*xi/2)/((1-
xi)*dEoverE))...
            *(omega_Lambda*rho_crit*length_conversion^3/10^(-6)/5)^(1/4)/f_Q;

        % Exclude fractional kinetic energy densities that exceed
        % 10 percent of dark energy density.
        if al>alphamax(j)
            Omega_KE(i,j)=NaN;
        else

            % Compute Q_dot for phonon model.
            Q_dot = (al*f_Q)^2*(1-xi)*dEoverE/(.12*Q_Lambda*(1-3/2*xi)*delta_t);  % GeV/yr
            Q_dot_list(i,j)=Q_dot;

            % Convert Q_dot to natural units.
            Q_dot_natural = Q_dot*time_conversion/(3.154*10^7);          % GeV^2

            % Compute kinetic energy density.
            rho_KE = Q_dot_natural^2/2;                                  % GeV^4

            % Covert kinetic energy density to intuite units.
            rho_KE_intuitive = rho_KE/length_conversion^3*10^(-6);       % GeV/cm^3

            % Compute fractional kinetic energy density.
            Omega_KE(i,j) = rho_KE_intuitive/rho_crit;
```

```
        end

        % Exclude fractional kinetic energy densities
        % where the equation of state parameter will
        % exceed that of w_DE_max.
        if Omega_KE(i,j)>Omega_KE_max
                Omega_KE_space(i,j) = NaN;
        else
                Omega_KE_space(i,j) = Omega_KE(i,j);
        end
   end
end

% Plot parameter spaces with color bar that indicates
% the value of the fractional kinetic energy density.
figure;
h1=pcolor(power_list,alpha,Omega_KE);
set(h1, 'EdgeColor', 'none');
colormap('jet');
set(gca,'ColorScale','linear');
c1 = colorbar;
c1.Label.String = '\Omega_{KE,phon}';

figure;
h2=pcolor(power_list,alpha,Omega_KE_space);
set(h2, 'EdgeColor', 'none');
colormap('jet');
set(gca,'ColorScale','linear');
c2 = colorbar;
c2.Label.String = '\Omega_{KE,phon}';
```